THESE

présentée à

L'UNIVERSITE DE LILLE 1

Pour obtenir le titre de **Docteur**

de l'Ecole Doctorale

Sciences de la Matière, du Rayonnement et de l'Environnement

par

Claudio Bettinelli

Etude de la photolyse à 266 nm ou 355 nm de composés carbonylés d'intérêt atmosphérique

Soutenue le 9 Décembre 2011

N°d'ordre : 40722

Directrice de thèse	Christa FITTSCHEN	Directrice de Recherches, Université Lille 1
Rapporteurs :	Elena JIMENEZ MARTINEZ	Professeur, Université Castilla La Mancha (Espagne)
	Holger SOMNITZ	Université de Essen - Duisburg (Allemagne)
Membres du jury :	Bela VISKOLCZ	Professeur, Université de Szeged (Hongrie)
	Jean-François PAUWELS	Professeur, Université Lille 1
	Pascal DREAN	Maître de Conférences, Université Lille 1
Membre invité :	Bernard LEMOINE	Chargé de Recherches, Université Lille 1

Remerciements

Ce travail, réalisé à l'Université de Lille 1, est issu d'une collaboration entre les laboratoires de Physico-chimie des Processus de Combustion et l'Atmosphère (PC2A) et Physique des Lasers, Atomes et Molécules (PhLAM). Il a été effectué au sein du Centre d'Etudes et de Recherches Lasers et Applications (CERLA), avec le soutien financier: Marie-Curie Early Stage Training Site "TOTECAT".

Je tiens d'abord à remercier messieurs Pascal Dréan, Maître de Conférences, et Bernard Lemoine, Chargé de Recherche CNRS, pour avoir encadré cette thèse, pour m'avoir laissé libre de pouvoir appliquer mes idées et choix et d'autre part d'avoir été disponibles à l'écoute. J'exprime toute ma gratitude à Mme Christa Fittschen, Directrice de Recherche, pour l'énergie et la passion transmise au cours des ces années, mais surtout pour m'avoir donné la possibilité de participer à des congrès nationaux et internationaux.

Je ne saurais oublier de remercier Maria Antiñolo Navas et Elena Jiménez membres du groupe 'Química y Contaminación Atmosférica (QYCA)' de l'Université de Castilla la Mancha (Espagne) pour la collaboration effectué avec le PC2A.

Je remercie l'ensemble des membres du jury et en particulier Holger Somnitz, Professeur à Institute of Physical and Theoretical Chemistry de l'Université de Duisburg-Essen (Allemagne) et Elena Jiménez Professeur de l'Université de Castilla la Mancha (Espagne) pour avoir accepté de juger ce mémoire.

Je tiens à remercier aussi l'ensemble des membres des laboratoires PC2A et CERLA, chercheurs, enseignants-chercheurs, étudiants pour m'avoir accueilli et aidé à comprendre et aimer la France.

Je termine en remerciant mes parents, pour la sagesse avec laquelle ils ont su encourager et accepter leur fils parti "chez les français", et tous mes amis, que seulement pour en faire la liste il faudrait un autre mémoire, pour m'avoir fait comprendre ce qu'est la vie dans le "Nord".

Enfin, la plus importante, Pauline, que je souhaite remercier pour l'écoute, la compréhension mais surtout pour la patience montrée pendant cette dernière année.

Index

I. Introduction

I.1 Definition of Volatile Organic Compounds.

Volatile Organic Compounds, referred as VOCs in the following, are organic molecules that can be defined according to different points of view. On one side, the European directive of the European Community 1999/13/EC (Esig) defines a VOC on the base of its vapour pressure, regardless to its reactivity:

"Volatile Organic Compounds are functionally defined as organic compounds having at 293.15 K (*i.e.*, 20°C) a vapour pressure of 0.01 kPa or more, or having a corresponding volatility under particular conditions of use. An organic compound is defined as any compound containing at least the element carbon and one or more of hydrogen, halogens (e.g., chlorine, fluorine or bromine), oxygen, sulphur, phosphorus, silicon, or nitrogen, with the exception of carbon oxides and inorganic carbonates and bicarbonates".

On the other hand, the United States Environmental Protection Agency (EPA) gives more importance to the reactivity of these molecules (EPA 2004):

"Volatile organic compounds means any compound of carbon, excluding carbon monoxide, carbon dioxide, carbonic acid, metallic carbides or carbonates, and ammonium carbonate, which participates in atmospheric photochemical reactions "

Methane (CH_4) is the most abundant organic species in the atmosphere. Methane is a VOC according to the first definition but not any more according to the second one because of its low reactivity, making its lifetime to be very long compared with other VOCs. It mainly participates to the global warming of the atmosphere. Methane is then sometimes considered apart from other VOCs, leading to the common expression of Non-Methane Volatile Organic Compounds NMVOC.

I.2 VOCs sources and emissions

VOCs released in the atmosphere can be classified as biogenic if they are biologically produced or anthropogenic if they are produced by the action of man. Molecules in the atmosphere are subjected to photolysis and / or oxidation to give rise to other VOCs, which are often oxygenated (OVOCs).

I.2.1 Anthropogenic emission of VOCs

Pollution from anthropogenic sources in industrial or urban areas are various and concern principally petroleum use or combustion. Several studies have been performed to quantify the annual amount of these emissions and define their chemical composition (Watson, Probert et al. 1991). Fuelwood and gasoline combustion are the most important sources of paraffins (around 9000 ktons/year) and major aromatics like benzene, toluene and xylene (Watson, Probert et al. 1991). Chemical manufactures and use of solvents are minor sources of aldehydes and aromatics which represent only 7% of the total VOCs emissions (Table I-1).

source	Fuelwood	Gasoline	chemicals	solvent use	petroleum
paraffins	9316	10979	4760	7218	350
olefines	7654	2479	1674	38	85
aromatics*	7503	2800	540	168	52
formaldehyde	0	1314	39	34	494
other aldehydes	0	53	80	0	0.036
other aromatics	0.2	2881	834	86	3
total	24474	19326	8118	7968	4137

Table I-1 Global VOCs Emissions by Source Category (ktons/year); * = benzene, toluene and xylene (Watson, Probert et al. 1991).

I.2.2 Natural sources

The Biogenic Volatile Organic Compounds (BVOC) are emitted from both terrestrial and marine sources. It is estimated that on a worldwide scale the total amount of the biogenic emissions are 10 times higher than the anthropogenic ones (Atkinson and Arey 1998). The most abundant emissions are due to forests (terpenes emitted by trees), followed by humic acid from the decomposition of the organic matter (soils), biomass fires and eruptions of volcanoes (Guenther, Hewitt et al. 1995; Niinemets, Loreto et al. 2004).

Studies have estimated the North America biogenic emissions to be 86 Tg (1 Tg = 10^{12} g) per year. Tropical forests are believed to produce about half of all global natural emissions of NMVOCs (Table I-2). More than one thousand different compounds are known to be emitted by natural sources. These emissions are composed of methanol (30%), hexene derivatives (8%), 2-methyl-3-buten-2-ol (5%), monoterpenes, sesquiterpenes (20%) and isoprene (30%) (Atkinson and Arey 1998; Guenther, Geron et al. 2000). This work deals with the photolysis of isoprene derivatives.

compounds	vegetation	soils	Biomass burning	total
Isoprene	29.3	0	0	29.3
2-methyl-3-buten-2-ol	3.2	0	0	3.2
Monoterpenes	17.9	0	0	17.9
Other reactive NMVOC	15.9	0.2	0.2	16.3
Other NMVOC	15.9	0.9	0.4	17.2
total NMVOC	82.2	1.1	0.6	83.9

Table I-2 Annual emission rates fluxes of NMVOC and COV from natural sources in North America expressed in equivalent tera gram-carbon (Tg-C). Other reactive NMVOC are primarily ethene, propene, hexenol, hexenyl-acetate, hexenal, acetaldehyde and formaldehyde (Guenther, Geron et al. 2000)

I.2.3 Indirect sources of VOCs

Degradation products of primary VOCs are called indirect sources of VOCs. The most important indirect sources are products from the reaction with the OH radical, followed by subsequent oxidation, and photolysis. Isoprene is the most abundant hydrocarbon released in the atmosphere. Its oxidation, initiated by the OH radical followed by subsequent addition of O_2 and reaction with NO, gives rise to a huge number of VOCs (Atkinson and Arey 2003) with methacrolein and methylvinylketone being formed in important yields (Table I-3).

	Products of the oxidation of isoprene				
Oxydant	methylvinylketone	methacrolein	formaldehyde	OH	methyl furane
OH	32	23	-	-	4
NO_3	3.5	3.5	11	-	-
O_3	16	39	90	27	-

Table I-3 Yields (%) of some secondary VOCs from the reaction of isoprene with OH, NO_3 or O_3 (Atkinson and Arey 1998).

I.3 Impact of the VOCs

I.3.1 Effects on human health

VOCs, once emitted in the atmosphere, may have a strong impact on human health. They are generally not acutely toxic but may have chronic effects. The United States Environmental Agency (EPA) evaluates the level of risk for continuous inhalation exposure on the human population considered without non cancerous effects. Some non cancerous effects on human are: eyes, nose, and throat irritation, headaches, loss of coordination, nausea, damage to liver, kidney, and central nervous system (EPAdefinition). Some VOCs, like formaldehyde, acetaldehyde and benzene, are known to cause cancer on animals and consequently are likely to cause cancer also on humans. Due to the low concentrations of VOCs and because the symptoms are difficult to be detected, analysis of VOCs and their effects on human health is still nowadays a developing area.

I.3.2 Environmental effects

Most of the VOCs, due to their physical-chemical properties, are ubiquitous (Ciccioli, Cecinato et al. 1996). For example, propane, butane, and many other VOCs have been found in Antarctica and Greenland, remote regions that are considered to be abroad from anthropogenic sources (Swanson 2003; Beyersdorf, Blake et al. 2010). The discovery of anthropogenic VOCs in such remote area indicates that VOCs can be transported on a global scale (Aghedo, Schultz et al. 2007; Beyersdorf, Blake et al. 2010).

When molecules absorb and emit in the thermal IR range, they are called greenhouse gases. CO_2, H_2O, CH_4 and O_3 are amongst the main greenhouse gases. The situation worsens when the degradation products of VOCs contribute to the greenhouse effect. It is therefore important to determine the pathways of degradation of VOCs, in order to know whether they give rise to greenhouse compounds or not.

Since the late ’50 it has been shown that VOC oxidation is responsible for the photochemical smog called Los Angeles type because of its first apparition in the homonymous city in the early 40’s (Delmas R. 2005). This particular smog irritates the eyes and the respiratory systems and it is nowadays occurring in many cities all over the world. In this type of smog, the ozone is produced at low altitude from the oxidation of VOCs under high NOx levels. In addition to the tropospheric

ozone production, there is also a formation of aldehydes (principal cause of the irritation of the respiratory systems) and peroxyacetyl nitrate PAN (reaction I-17 page 20).

I.4 Chemistry of the troposphere

I.4.1 Atmospheric layer and troposphere

The Earth's atmosphere is conventionally divided in a series of layers, according to their characteristics and properties. The lowest and most dense part of the atmosphere in contact with the Earth's surface is called the troposphere, the structure of which is shown in Figure I-1 on the next page. The temperature decreases rapidly with height from 293 K at the surface of the Earth to 223 K at an altitude of 10 km. The tropopause is a boundary layer separating the troposphere and the stratosphere. The altitude of the tropopause varies with the seasons and the latitude (about 9-12 km at the poles and 15-18 km at the equator).

The troposphere contains almost 80% of the mass of the atmosphere and a dry volume of air contains roughly N_2 (78%), O_2 (20%), Ar (0.93%) and CO_2 (0.036%). The remaining part is constituted by water vapour, depending on altitude and temperature and trace gases (VOCs, O_3, NO_X, etc...).

The troposphere is itself divided in two parts with distinct characteristics:

- The boundary layer extends from the Earth's surface up to a few hundred meters to about 1 km.
- The free troposphere, between the boundary layer and the tropopause, is a turbulent region mixed by high-speed winds.

The stratosphere is situated above the tropopause. It extends to an altitude of around 50 km. In the stratosphere, the temperature increases with altitude, due to the absorption of solar UV radiations by O_2 and thereby formation of the ozone layer.

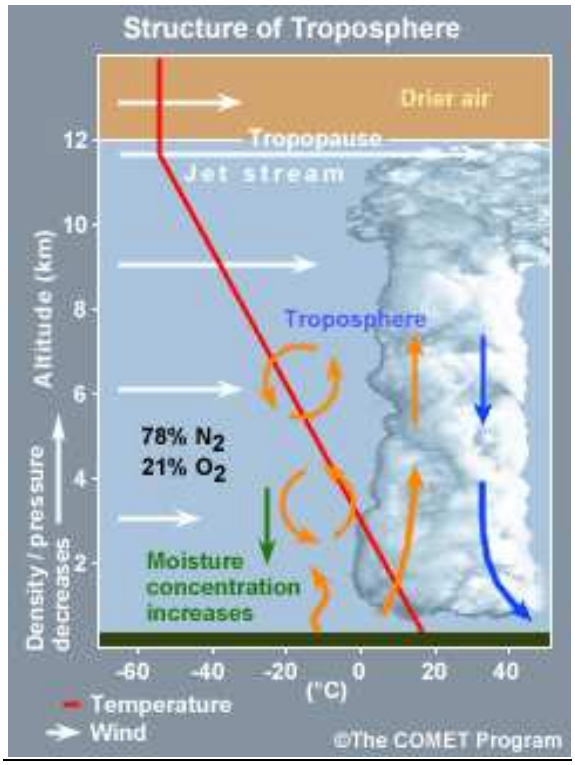

Figure I-1 Temperature profile in the troposphere and mixing effect of the winds (COMET program of the University corporation for atmospheric research UCAR).

I.4.2 Solar spectrum

The solar emission can be assimilated as the emission of a blackbody at a temperature of 5800 K (Figure I-2) (Ravishankara and Moortgat 1994). In the visible and infrared (IR) ranges, the spectral radiation density can be approximately described by a continuous Boltzmann distribution expressed by the Planck's law (Delmas R. 2005):

$$\Psi(\lambda) = \frac{\frac{2hc^2}{\lambda^5}}{\exp\left(\frac{hc}{\lambda kT}\right) - 1} \qquad \text{I-1}$$

where $\psi(\lambda)$ is expressed in J m^{-3} s^{-1} or in W m^{-3}; h is the Planck constant; k is the Boltzmann constant and c is the speed of light.

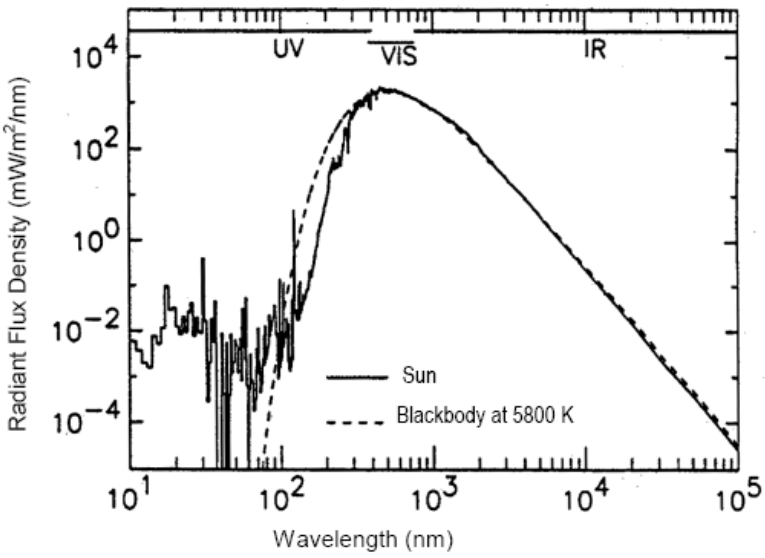

Figure I-2 Solar radiation flux in the outer atmosphere (Ravishankara and Moortgat 1994).

The radiation flux in the atmosphere will be altered in intensity due to absorption by molecules and subjected to the Lambert Beer law:

$$I(\lambda) = I_0(\lambda)e^{-t(\lambda)m} \qquad \text{I-2}$$

where t(λ) is the attenuation coefficient and m is the mass of air to be crossed.

The shortest wavelengths of the UV radiation are absorbed almost completely in the upper atmospheric layers (Figure I-3). In addition, the incident solar radiation at a wavelength shorter than 200 nm is strongly attenuated by absorption of molecular oxygen (Delmas R. 2005). Water vapour and CO_2 instead contribute for wavelengths below 80 and 165 nm respectively (Figure I-3 right). At wavelengths above 180 nm, the absorption cross-section of O_2 declines sharply, but oxygen still absorbs efficiently due to its high concentration.

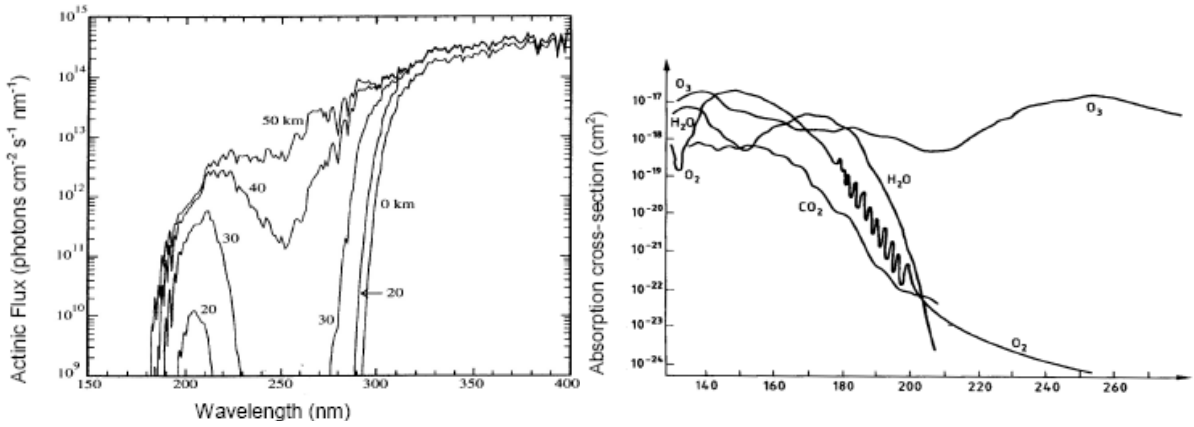

Figure I-3 Left : Actinic flux as function of the altitude and wavelength for a solar zenith angle 33°. Right : absorption cross sections for atmospheric species absorbing in the range 100-260 nm (Finlayson-Pitts and Pitts 2000).

The actinic flux F(λ), plotted in Figure I-3 left, represents the amount of light available at a given altitude. Usually expressed in photons cm^{-2} s^{-1} nm^{-1}, it includes direct, reflected and scattered radiation. The actinic flux, which is the relevant quantity for light intensity in photochemical processes, depends on many factors like solar zenith angle (and thus daytime, season and latitude), altitude, albedo, etc... (Finlayson-Pitts and Pitts 2000). From Figure I-3, we notice that below 50 km there is no radiation available at wavelengths below 180 nm, and radiations between 200 and 290 nm are almost completely absorbed by ozone in the 50-20 km height interval. This wavelength limit is called the actinic cut-off. The available radiations in the troposphere are then limited to wavelengths longer than 290 nm (Delmas R. 2005).

I.4.3 Photochemical processes

Photochemical processes play a central role in the chemistry of the atmosphere because they represent the major source of radicals. The interaction of light with a molecule depends strongly on the wavelength of the radiation. Photons in the UV range possess enough energy (several hundreds of kJ mol^{-1}, see Table I-4) to induce chemical changes for the majority of atmospheric species: bond ruptures (Table I-5) and electronic excitation. Only a small fraction (a few percent) of the incoming photons fulfils this condition, but it is enough to transform the atmosphere into a vast photochemical reactor.

Electromagnetic region	visible	near UV	middle-UV	far UV
λ (nm)	780 - 400	400 - 300	300 - 200	200 - 120
E (kJ mol^{-1})	154 - 299	299 - 399	450 - 599	599 - 997

Table I-4 Visible and UV radiations with the relative photon energies (Delmas R. 2005).

Bond	H-CH_3	CH_2CH-CHO	CH_3CO-CH_3	O-NO	Br-CH_3
Energy (kJ mol^{-1})	435	354	350	300	293

Table I-5 Energies required for some bond breaking (Delmas R. 2005).

When a photon is absorbed by a molecule, it induces the transition from the electronic fundamental state to an excited state. For instance, we consider the one photon process that brings the molecule AB to an excited state AB* (I-3).

$$AB + h\nu \rightarrow AB^* \qquad \text{I-3}$$

From the excited state AB* the molecule can evolve following different pathways: physical, chemicals or others. The primary photochemical processes encountered in the atmosphere are:

Emission	$AB^* \rightarrow ABj + h\nu'$	I-4
Energy transfer	$AB^* + M \rightarrow AB + M$	I-5
Dissociation	$AB^* \rightarrow A + B$	I-6
Isomerization	$AB^* \rightarrow AB'$	I-7
Non radiative transition	$AB^* \rightarrow AB_j$	I-8

The dissociation is often responsible for the radical generation producing reactive species that drive most of the cycles in the atmosphere.

The photodissociation of the molecule AB absorbing a radiation hν is expressed from reaction (I-9). The formation of the products A or B is predictable with equation (I-10) that describes the dependence of the photodissociation from the intensity of the incident radiation and the absorption efficiency of the molecule AB (Delmas R. 2005).

$$AB + h\nu \rightarrow A + B \qquad \text{I-9}$$

$$\frac{d[A]}{dt} = J_\lambda [AB] = F_\lambda \sigma_\lambda \Phi_\lambda [AB] \qquad \text{I-10}$$

where J_λ is the photolysis rate constant (s^{-1}) and F_λ is the intensity of the photons flux expressed in photons $cm^{-2}\ s^{-1}$. The parameter Φ_λ called the quantum yield is the probability for a reaction to occur after absorption of a photon at the wavelength λ. The aim of our work was to determine the quantum yield of photolysis of some aldehydes and ketones.

I.5 Reactive species and tropospheric mechanisms

I.5.1 Nitrogen oxides (NO_x)

I.5.1.1 Sources and emissions

The presence of nitrogen oxides NO and NO_2 in the atmosphere is mainly due to human activities (Delmas R. 2005). The most important source of NO_X is fossil fuel combustion that represents almost 50% of the global emissions (Table I-6). NO_X emissions within the troposphere are more punctual but still not negligible. The process of ammonia oxidation, for example, produces the highest amount of NO_X in the atmosphere corresponding to 34% of the total emissions.

Sources of NO_x	Surface sources			Tropospheric sources			
	Fossil fuel combustion	Biomass burning	Biogenic soil emission	Lightning	Aircrafts	Ammonnia oxidation	total
Tg n/Y	22	6.7	5.5	2	0.55	13	38.2
Origin (%)	100	95	40	0	100	60	83

Table I-6 Main sources of NO_X and quantification of their emissions (Tons/Y), and proportion of their anthropogenic origin (Delmas R. 2005).

I.5.1.2 Reactivity of NO_x

It is estimated that NO represents the majority of the total NO_X emissions. Only a small fraction of the NO_x (10-30%) is emitted as NO_2 (Yao, Lau et al. 2005), the remaining coming from the oxidation of NO (Atkinson 2000). When the oxidation takes place close to the emission sources, where the NO concentrations are elevated, it occurs rapidly and is driven directly from O_2.

$$2NO + O_2 \rightarrow 2\ NO_2 \qquad \text{I-11}$$

In absence of competitive reactions, the ratio NO/NO_2 is regulated by a photostationary cycle related to the concentration of O_3 (Atkinson and Arey 1998). During daytime, NO_2 will be photolyzed leading to NO :

$$NO_2 + h\nu \rightarrow NO + O(^3P) \quad (\lambda<420nm) \qquad \text{I-12}$$

Oxygen in the ^3P state subsequently reacts with molecular oxygen to generate ozone :

$$O(^3P) + O_2 + M \rightarrow O_3 + M \qquad \text{I-13}$$

Under tropospheric conditions, the oxidation of NO occurs mainly with ozone:

$$NO + O_3 \rightarrow NO_2 + O_2 \qquad \text{I-14}$$

At typical boundary layer concentration of O_3 of 30 ppbv, the oxidation reaction I-14, closing the photostationary cycle, occurs on a timescale of circa 1 min (Jenkin and Clemitshaw 2000).

The presence of HO_X and RO_2 radicals in the atmosphere perturbs the photostationary cycle, because it leads through reaction (I-15) and (I-16) to an oxidation of NO to NO_2 without simultaneous destruction of O_3, and hence to a build-up of tropospheric ozone:

$$NO + HO_2 \rightarrow NO_2 + OH \qquad \text{I-15}$$

$$NO + RO_2 \rightarrow NO_2 + RO \qquad \text{I-16}$$

I.5.1.3 Losses

Other than the build-up of tropospheric ozone, the reaction between HOx radicals (see paragraph I.5.2 page 20) and NOx species leads to the generation of the oxyacids, nitric acid (HNO_3), peroxynitric acid (HO_2NO_2) and nitrous acid (HONO) that remove nitrogen oxides from the atmosphere (Jenkin and Clemitshaw 2000) (Figure I-4). In the same way the reactions of the organic peroxy radicals (RO_2) with NO can generate organic nitrates ($RONO_2$) which are thermal reservoir of this species.

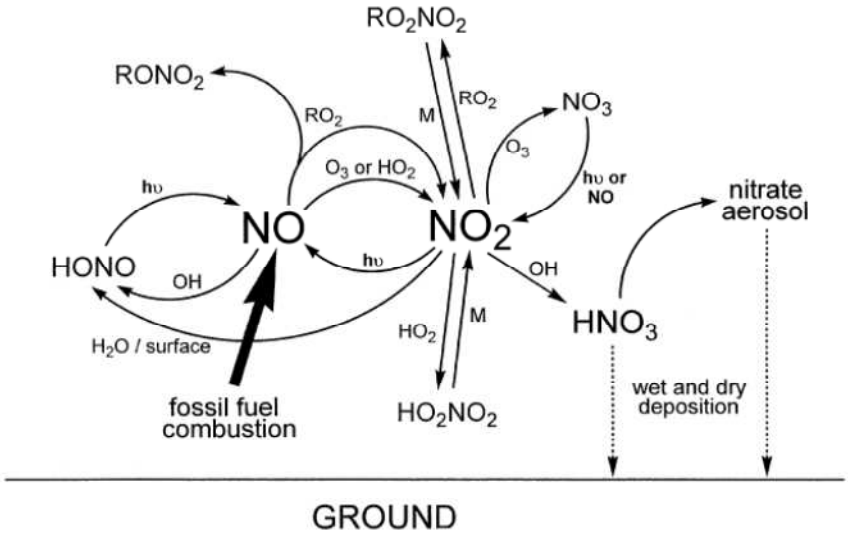

Figure I-4 Daytime cycles of oxidized nitrogen compounds in the troposphere (Jenkin and Clemitshaw 2000).

Organic peroxy radicals (RO_2) can react with NO_2 generating the peroxyacyl nitrates (PAN) (I-17) (Atkinson 2000).

$$NO_2 + RO_2 (+M) \leftrightarrows ROONO_2 (+M) \qquad \text{I-17}$$

As is shown in Table I-7, if the radical R contains a ketonic group (C=O), the bond OO-NO_2 formed in reaction (I-17) is more stable compared to an alkyl peroxy derivatives. This increases the lifetime of the products (Atkinson and Arey 1998) from a few seconds for methyl radicals to 50 minutes for acetyl radicals.

R	H	CH_3	C_2H_5	CH_3CO	CH_2=CH(CH_3)CO
k_{-17} (s^{-1})	0.076	1.6	4	0.00033	0.00035
lifetime	13 s [a)]	0.61 s [b)]	0.25 s [b)]	50 min [b)]	48 min [c)]

Table I-7 Thermal decomposition rates (k_{-17}) and lifetimes for a series of peroxy nitrates at 298 K and 760 Torr. a)(Atkinson, Baulch et al. 1997b); b) (Atkinson, Baulch et al. 1997a); c) (Roberts and Bertman 1992).

I.5.2 Hydroxy radicals (HO_X)

The radicals OH and HO_2 are the two hydroxy radicals important in atmospheric chemistry. Even if their concentrations in the atmosphere are quite low (10^5 to 10^8 cm^{-3}), they have a fundamental relevance in the chemistry of the atmosphere because they are the main oxidizing agents of VOCs (Atkinson 2000) (see paragraph I.6.4 page 27).

I.5.2.1 Sources of HO_x.

The OH radical is principally generated by the photolysis of O_3 at wavelengths lower than 330 nm. The oxygen atom in the singlet state D generated by this photodissociation (I-18) subsequently reacts with H_2O (I-19) to form the hydroxyl radical (Jenkin and Clemitshaw 2000).

$$O_3 + h\nu \rightarrow O_2 + O(^1D) \quad (\lambda<330nm) \qquad \text{I-18}$$

$$O(^1D) + H_2O \rightarrow 2\ OH \qquad \text{I-19}$$

It should also be noted that only a small quantity of $O(^1D)$ reacts with H_2O because of the antagonist quenching reaction (I-20):

$$O(^1D)\ (+M) \rightarrow O\ (+M) \qquad \text{I-20}$$

Seen the dependence on the H_2O concentration, the OH yield is influenced by altitude, latitude and season. During night OH is principally formed by O_3 reaction on unsaturated VOCs (Jenkin and Clemitshaw 2000). Early in the morning, the photolysis of HONO can also be a major OH source:

$$HONO + h\nu \rightarrow OH + NO \ (\lambda<400nm) \qquad \text{I-21}$$

A major source of HO_2 radicals in the troposphere is the reaction of O_2 with alkoxy radicals. Another source of HO_2 radicals during daytime is the photolysis of aldehydes. In particular conditions, like in heavy industrial areas or urban atmospheres with high VOC concentrations, these reactions can overcome the ozone photodissociation as radical source (I-18 and I-19). As an example, the photolysis of formaldehyde (Atkinson and Arey 1998) produces two molecules of HO_2 for each molecule of formaldehyde (reactions from I-22 to I-24).

$$H_2CO + h\nu \rightarrow H + HCO \qquad \text{I-22}$$

$$HCO + O_2 \rightarrow HO_2 + CO \qquad \text{I-23}$$

$$H + O_2 \ (+M) \rightarrow HO_2 \ (+M) \qquad \text{I-24}$$

I.5.2.2 Losses

HOx radicals can be removed from the atmosphere through a variety of reactions. The products of these reactions can act as reservoirs because of their ability to regenerate HO_x radicals. The most significant tropospheric sinks for the HO_x are reactions with peroxy radicals:

$$HO_2 + HO_2 \rightarrow O_2 + H_2O_2 \qquad \text{I-25}$$

$$RO_2 + HO_2 \rightarrow ROOH + O_2 \qquad \text{I-26}$$

$$OH + HO_2 \rightarrow H_2O + O_2 \qquad \text{I-27}$$

or the removal by reaction with NO_x species (Jenkin and Clemitshaw 2000)

$$OH + NO_2 \ (+M) \rightarrow HONO_2 \ (+M) \qquad \text{I-28}$$

$$OH + NO \ (+M) \rightarrow HONO \ (+M) \qquad \text{I-29}$$

The average OH concentration over 24 hours is estimated to be $[OH] \approx 10^6$ molec cm^{-3}, but varies, depending on the atmospheric conditions: solar irradiation, ozone and water vapour concentration and trace gas load. On the other hand the concentrations of HO_2 radicals is estimated to be 100 times more important than the concentration of OH radicals ($[HO_2] \approx 10^8$ molec cm^{-3}) (Atkinson 2000).

I.5.3 Nitrates radicals

The nitrates radicals, principally NO_3 and N_2O_5, destroy O_3 in processes occurring during night-time. They basically represent the chemistry of VOC oxidation at night (Jenkin and Clemitshaw 2000).

I.5.3.1 Sources

The radical NO_3 is formed by reaction of NO_2 with O_3 (I-30) (Atkinson 2000) and its concentration become noticeably during night, because it is readily photolyzed during day (I-31) making its lifetime extremely short (t < 5s)(Jenkin and Clemitshaw 2000): .

$$NO_2 + O_3 \rightarrow NO_3 + O_2 \qquad \text{I-30}$$

$$NO_3 + h\nu \rightarrow NO_2 + O(^3P) \qquad \text{I-31}$$

The average nighttime concentration of NO_3 (Atkinson and Arey 1998) is believed to be $[NO_3] \approx 10^6$ molec cm^{-3}. Another important reaction of NO_3 during night is its equilibrium reaction with NO_2 (I-32) (Atkinson 2000).

$$NO_3 + NO_2 (+M) \leftrightarrows N_2O_5 (+M) \qquad \text{I-32}$$

The equilibrium is fast. At an average night concentration of NO_2 of 10 ppbv, N_2O_5 is formed in almost 2 s and it is destroyed in 15 s at 298K (Atkinson 2000). As a consequence, their behaviour is strongly coupled and any process removing one of the species is also a sink for the other.

I.5.3.2 Losses

During daytime the NO_3 radical is removed efficiently by photolysis (I-31,I-33) leading to NO_2 and ozone formation. In case of strong solar irradiation this reaction occurs on the second time scale (Atkinson 2000). At night NO_3 react rapidly with NO by the reaction I-34.

$$NO_3 + h\nu \rightarrow NO + O_2 \ (\lambda<520nm) \qquad \text{I-33}$$

$$NO_3 + NO \rightarrow 2\ NO_2 \qquad \text{I-34}$$

N_2O_5, formed during night, is removed from the atmosphere by wet or dry deposition, or by heterogeneous reaction with H_2O (I-35) (Jenkin and Clemitshaw 2000).

$$N_2O_5 + M \rightarrow NO_2 + NO_3 + M \qquad \text{I-35}$$

I.5.4 Ozone

I.5.4.1 Stratospheric

Almost 90% of ozone is contained in the stratosphere (Delmas R. 2005). The remaining 10% is contained and formed in the troposphere. The understanding of the basics of ozone photochemistry began with Chapman (1930), who supposed that UV radiation was responsible for ozone production in the stratosphere. The atomic oxygen is formed by the dissociation of O_2 at wavelength shorter than 242 nm.

$$O_2 + h\nu \rightarrow O + O \ (\lambda<242nm) \qquad \text{I-36}$$

The ozone then will be formed by reaction of the atomic oxygen with one molecule of O_2.

$$O_2 + O \ (+M) \rightarrow O_3 \ (+M) \qquad \text{I-37}$$

Ozone formed by reaction (I-37) is removed by photolysis at wavelengths shorter than 310 nm, producing oxygen in the singlet state (I-18) readily quenched by atmospheric O_2 or N_2 (I-38).

$$O(^1D) + M \rightarrow O(^3P) + M \qquad \text{I-38}$$

The ozone absorbing the radiation at wavelengths lower than 310 nm works actively as a filter, protecting the surface of the Earth from the UVA and B radiations (Newman and Morris) (Figure I-5).

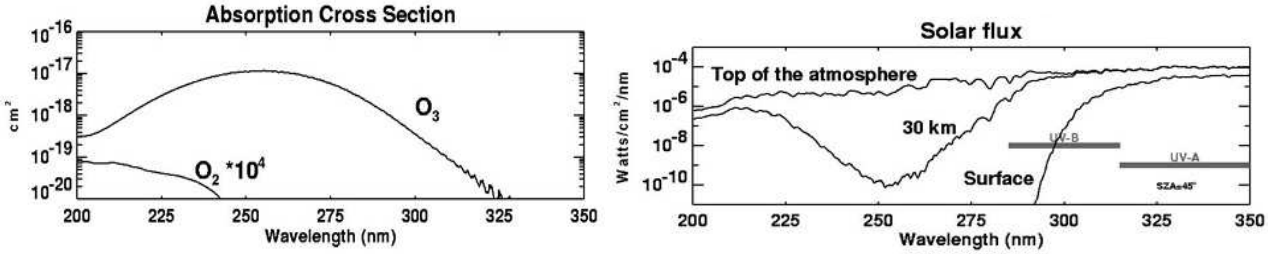

Figure I-5 Absorption cross sections of O_2 and O_3 in the wavelength range 200-350nm and relative actinic flux at: the stratosphere the ozone layer and the hearth surface (Newman and Morris).

I.5.4.2 Tropospheric

The tropospheric ozone represents 10% of the atmospheric ozone and is formed from the direct reaction of molecular oxygen with atomic oxygen (I-37). The atomic oxygen is formed from the

NO_2 photolysis at wavelength lower than 420 nm (I-12)(Atkinson and Arey 1998; Jenkin and Clemitshaw 2000). The tropospheric ozone concentration in unperturbed atmospheres depends principally on the ratio between NO_2 and NO, because it is formed by reactions I-12 and I-14 but it is removed from the atmosphere by reaction with NO (I-14) (Atkinson and Baulch 2004).

This photostationary equilibrium of the three species O_3-NO-NO_2, resumed in Figure I-6, can be altered by parallel reactions oxidizing NO to NO_2 during the photodegradation of VOCs. These compounds, after photolysis or OH reaction and in presence of O_2, generate peroxy radicals (RO_2) that subsequently oxidized NO to NO_2 (Atkinson and Arey 1998)

$$RO_2 + NO \rightarrow NO_2 + RO \qquad \text{I-39}$$

The alkoxy radical formed can be further oxidized by molecular oxygen to produce HO_2 radicals

$$RO + O_2 \rightarrow R_{-H}O + HO_2 \qquad \text{I-40}$$

HO_2 will oxidize another NO to NO_2 with subsequent production of O_3

$$HO_2 + NO \rightarrow NO_2 + OH \qquad \text{I-41}$$

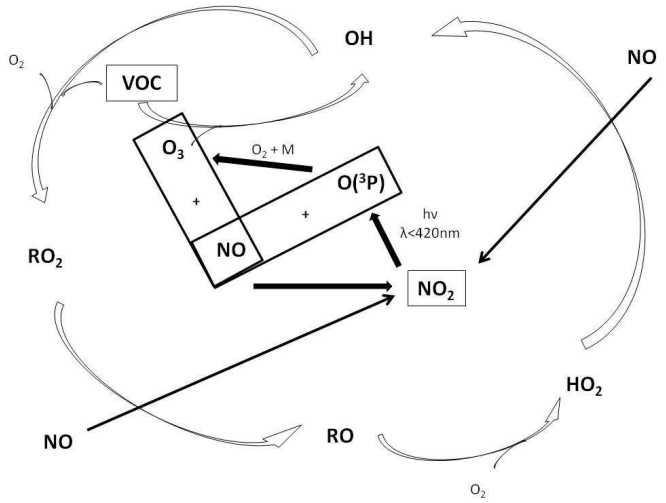

Figure I-6 Tropospheric ozone formation and relevance of the VOC in the NO/NO_2 equilibrium. Adapted from (Jenkin and Clemitshaw 2000).

Once again the concentrations of HO_2 and RO_2 radicals are dependent upon the solar intensity, which means that in the most enlightened hours of the day, ozone will reach its maximum concentrations. Contrarily during night-time unsaturated VOCs consume ozone generating OH (Atkinson and Baulch 2004).

I.6 VOC degradation mechanisms

In the atmosphere, VOCs can be removed by:

- dry or wet deposition (Matsunaga, Guenther et al. 2007). A deposition phenomenon is a condensation/absorption process on dust particles or water droplets (generally aerosols) that brings those hydrocarbons back to the ground. For most of the VOCs wet or dry deposition starts to be relevant only after transformation in oxidized species such as alcohols, acids or peroxy-alcoxy radicals (Atkinson and Baulch 2004).
- reaction with OH, O_3, NO_3 or photolysis (Atkinson 2000). The photolysis process is relatively important particularly for aldehydes and ketones because of their ability to absorb radiation at wavelength longer than 290 nm.

In the following paragraphs we present briefly the dynamics of those removal reactions trying to understand their importance in the atmosphere.

I.6.1 Reaction with ozone

The degradation by ozone occurs only for unsaturated VOCs. The ozone is added to the double bond (RC=CR) generating an ozonide, a five atoms ring that dissociates depending on its internal energy. The dissociation leads to a carbonyl oxide (Criegee intermediate) and to aldehydes and / or ketones (Jenkin and Clemitshaw 2000; Zhang, Lei et al. 2002).

$$O_3 + RHC=C(R)_2 \rightarrow RCHO + [(R)_2COO]^{++} \quad \text{I-42}$$

$$O_3 + RHC=C(R)_2 \rightarrow (R)_2CO + [RCHOO]^{++} \quad \text{I-43}$$

The Criegee intermediate is stabilized by collision or decomposes. The main products of this decomposition are carboxylic acids RC(O)OH and OH radical (Zhang, Lei et al. 2002).

$$[RCHOO]^{++} + H_2O \rightarrow RC(O)OH + H_2O \quad \text{I-44}$$

$$[RCHOO]^{++} \rightarrow R_HCHO + OH \quad \text{I-45}$$

It should be noted that the ozone reaction with VOCs is consider to be one of the most important sources of OH at nighttime (Atkinson 2000).

I.6.2 Reaction with NO_3

During nighttime the NO_3 reaction plays an important role because of the increase of its concentration (paragraph I.5.3 page 22). The reaction proceeds via H atom abstraction for saturated molecules (I-46) (very minor compared to reaction with OH) or aldehydes (I-47) (Atkinson 2000), leading in presence of oxygen to RO_2 and $RCOO_2$ radicals.

$$RH + NO_3 \rightarrow R + HNO_3 \qquad \text{I-46}$$

$$RC(O)H + NO_3 \rightarrow RCO + HNO_3 \qquad \text{I-47}$$

Peroxy radicals react with HO_2 and RO_2 to give rise to smaller aldehydes, carboxylic acids, hydro peroxides or with NO_2 to produce RO_2NO_2 (Atkinson 2000).

The addition of NO_3 to unsaturated VOCs, in presence of O_2, generates nitratoalkyl peroxy radicals. These radicals react with HO_2, RO_2 or NO_2 to originate peroxy nitrate in a thermal equilibrium. Peroxy nitrates act as reservoirs of NO_X released thermally during day (Jenkin and Clemitshaw 2000).

I.6.3 Reaction with OH radical

The OH radical reacts with VOCs by hydrogen abstraction or addition to an unsaturated bond, followed by reaction with O_2 to give peroxy radicals (Atkinson 2000).
For alkanes, ethers, alcohols, aldehydes, carbonyls and esters, the main reaction is the hydrogen abstraction from the various C-H bonds (I-48) (Atkinson 2000).

$$RCHO + OH \rightarrow RCO + H_2O \qquad \text{I-48}$$

For unsaturated molecules the reaction proceeds via addition to the double bond:

$$RCH{=}CHR + OH \rightarrow RCH\text{-}CROH \qquad \text{I-49}$$

The radicals generated in the reactions I-48 and I-49 will react rapidly under atmospheric conditions with oxygen to originate an important class of compounds in the atmospheric chemistry: the organic peroxy radicals (Atkinson and Baulch 2004).

$$CH_3CO + O_2 \rightarrow CH_3C(O)O_2 \qquad \text{I-50}$$

The further fate of peroxy radicals depends on the environment: under polluted conditions, *i.e.* high NOx level, they will rapidly be converted to alkoxy radicals, thereby oxidizing NO to NO_2 and leading to the formation of O_3, while in remote environments, *i.e.* low NOx levels, their lifetime can exceed several minutes and the primary fate is cross reaction with other peroxy radicals.

I.6.4 VOCs oxidation

The oxidation of VOC is initiated either by absorption of sunlight in the UV range or by reaction with OH or NO_3 radicals or ozone. The OH radical, together with HO_2, in presence of nitrogen oxides, catalyses the VOCs degradation to ideally CO_2 and water vapour.

$$RR' + h\nu \rightarrow R + R' \quad \text{I-51}$$

$$RH + OH \rightarrow R + H_2O \quad \text{I-52}$$

The alkyl radicals produced from the initiation reaction are subsequently oxidized to alkoxy radicals from a first reaction with O_2 and a further reaction with NO (Atkinson 2000).

$$R + O_2 \rightarrow RO_2 \quad \text{I-53}$$

$$RO_2 + NO \rightarrow RO + NO_2 \quad \text{I-54}$$

The formed alkyl radical is secondarily oxidized by O_2 and generates HO_2 radical that acts as the chain propagator (Jenkin and Clemitshaw 2000).

$$RO + O_2 \rightarrow R_{-H}O + HO_2 \quad \text{I-55}$$

$$RO \rightarrow R_{-H}OH \quad \text{I-56}$$

$$RO \rightarrow 'R + \text{carbonyl} \quad \text{I-57}$$

Once again the chain of reaction is catalyzed by NO driving to the OH regeneration. The new OH formed in this way will be available for a new initiation of the oxidation process (Atkinson 2000). The NOx-catalyzed VOC oxidation is schematically shown in Figure I-7:

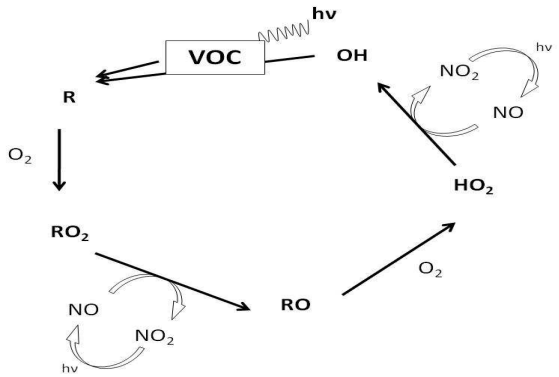

Figure I-7 Schematic of the VOCs oxidation cycle catalyzed by NOx radicals (Jenkin and Clemitshaw 2000).

The OH-initiated oxidation mechanism of isoprene, one of the most abundant biogenic hydrocarbons present in the atmosphere (Guenther, Geron et al. 2000), is presented in Figure I-8. In presence of NO it gives origin to a large number of VOCs among which are found methacrolein and methylvinylketone (Paulot, Crounse et al. 2009)(Figure I-8). Hydroxyacetone is also formed directly in the atmosphere from the oxidation of isoprene but clearly with lower yield because of the numerous steps. The investigation of the photolysis of these three molecules has been the subject of this phD work.

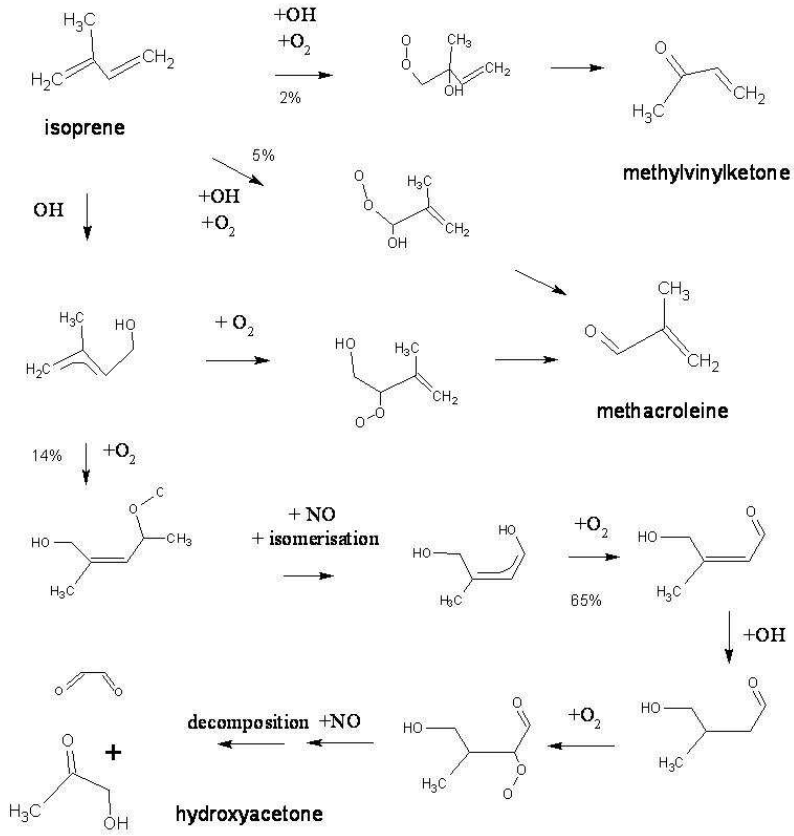

Figure I-8 Schematic of the isoprene oxidation ways leading to to the formation of methylvinylketone, methacrolein and hydroxyacetone (adapted from Paulot, Crounse et al. 2009).

I.6.5 Photolysis of ketones and aldehydes

The photolysis process and the photodissociation process have been already introduced in paragraph I.4.3 page 16. This paragraph will be devoted to the photodissociation of oxygenated VOCs, giving particular attention to aldehydes and ketones. The majority of molecules belonging to one of these two groups have non-zero absorption cross sections in the actinic range (Atkinson 2000) which can influence and reduce their lifetime in the atmosphere (paragraph I.7 page 30).

The photolysis of ketones and aldehydes proceeds via dissociation of the C-R bond in the α position of the carbonyl group (Blitz, Heard et al. 2006; Rajakumar, Gierczak et al. 2008). According to the energy of the incident photons, one or two bonds may be broken.

$$R_1COR_2 + h\nu \rightarrow R_1 + CO + R_2 \qquad \text{I-58}$$

$$R_1COR_2 + h\nu \rightarrow R_1CO + R_2 \qquad \text{I-59}$$

For ketones analyzed in the current work the radical R_1 appearing in reactions I-58 and I-59 is the methyl radical. For aldehydes instead R_1 is represented by H.

$$R_1C(O)H + h\nu \rightarrow R_1 + CHO \qquad \text{I-60}$$

$$R_1C(O)H + h\nu \rightarrow R_1 + CO + H \qquad \text{I-61}$$

The formation of the photofragment (for example CO) is predictable with equation I-62 describing the dependence of the photodissociation from the intensity of the incident radiation and the absorption efficiency of the molecule R_1COR_2 (Delmas R. 2005).

$$[CO] = J_\lambda [R_1COR_2] = F_\lambda \sigma_\lambda \Phi_\lambda [R_1COR_2] \qquad \text{I-62}$$

where J_λ is the photolysis rate constant (s^{-1}), σ_λ is the absorption cross section and F_λ is the intensity of the photon flux expressed in photons $cm^{-2}\ s^{-1}$. The parameter Φ_λ called the quantum yield is the probability for a reaction to occur after absorption of a photon at a determined wavelength λ.

In the current phD work we studied the photolysis of aldehydes and ketones at two different wavelengths 266 nm and 355 nm. At these wavelengths the molecules studied reaach their maximum of UV absorption, as can be seen in Figure I-9.

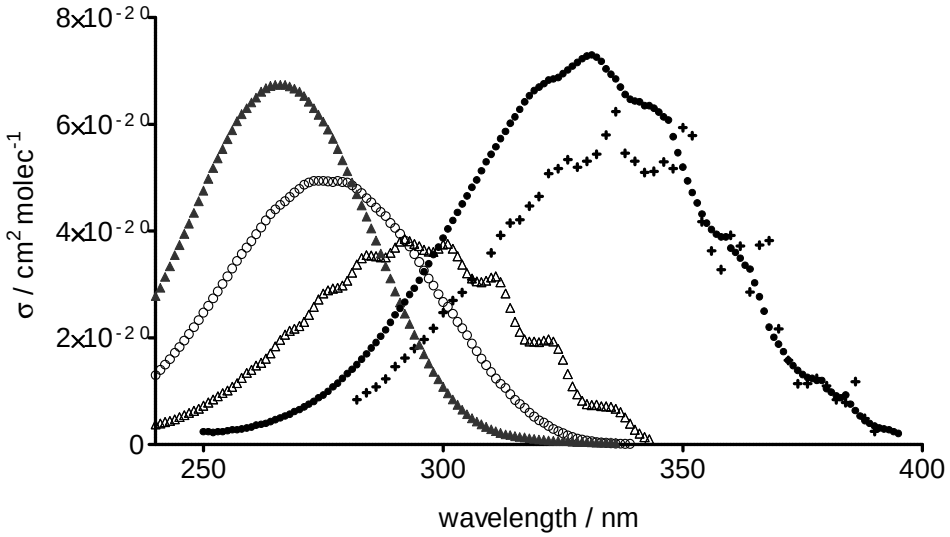

Figure I-9 UV absorption spectrum at 298 K of: -acetone (O ,(Gierczak, Burkholder et al. 1998)), hydroxyacetone (▲, (Orlando, Tyndall et al. 1999)), 3,3,3-trifluoropropionaldehyde (Δ,(Sellevåg, Kelly et al. 2004)), acrolein (+, (Magneron, Thévenet et al. 2002)), methyl vinyl ketone (•, (Gierczak, Burkholder et al. 1997)).

As presented in reaction I-62 the absorption cross section, together with the intensity of the incident radiation are the key elements of a photolytic process. For volatile organic compounds like aldehydes and ketones that have high absorption cross sections in the UV region the photolysis can result in an important removal process (Atkinson 2000).

I.7 VOC lifetime

For each VOC, depending on the removal processes previously presented, it is possible to determine its time of residence in the atmosphere (Delmas R. 2005).

If we consider that a molecule AB undergoes photolysis, the lifetime will be defined as:

$$AB + h\nu \rightarrow A + B \qquad \text{I-63}$$

$$t_{AB} = \frac{1}{J_\lambda} = \frac{[AB]}{\frac{-d[AB]}{dt}} \qquad \text{I-64}$$

The same will be for a bimolecular reaction (with OH, O_3 or NO_3).

$$AB + C \rightarrow \text{Products} \qquad \text{I-65}$$

$$t_{AB} = \frac{1}{k[C]} = \frac{[AB]}{\frac{-d[AB]}{dt}} \qquad \text{I-66}$$

If we consider the example of OH reaction, the lifetime of the VOC will depend on the rate constant and on the OH concentration. In the atmosphere, all reactions occur simultaneously so that the calculation of the effective lifetime of a molecule needs to include the contribution from all reaction pathways.

$$t_{AB} = \frac{1}{\sum k_i [C_i]} \qquad \text{I-67}$$

The lifetime of a VOC is a parameter that has already been largely studied for reactions with OH, NO_3 and O_3 (Atkinson and Arey 1998). Some of the data present in literature are reported in this work to give an overview on the relative importance of these three major reactions for different species. The individual lifetimes presented in both tables (Table I-8 and Table I-9) are determined on the average of 12h daytime for a OH concentration of 2×10^6 molec cm^{-3}; an average of 12 night-time $[NO_3] = 5\times10^8$ molec cm^{-3} and the ozone concentration over 24h $[O_3] = 7\times10^{11}$ molec cm^{-3} (Atkinson and Arey 1998).

From these lifetime values we can observe that biogenic VOC react fast with both, OH and NO_3, determining an average lifetime of a few hours. Anthropogenic VOCs are generally less reactive and have longer residence times. It is also possible to notice how photolysis in the case of ketones and aldehydes becomes relevant to the total removal process. This particular effect is due to the non-negligible absorption cross sections that these two classes of compounds still have in the actinic region ($\lambda > 290$ nm).

biogenic VOC	OH	NO_3	O_3
isoprene	1.4 h	1.6 h	1.3 days
camphene	2.6 h	1.7 h	18 days
3-carene	1.6 h	7 min	11 h
limonene	50 min	5 min	2.0 h
myrcene	40 min	6 min	50 min
α -phellandrene	50 min	8 min	8 h
α -pinene	1.8 h	25 min	1.1 day
sabinene	1.2 h	7 min	4.6 h
α-caryophyllene	40 min	4 min	2 min
longifolene	3.0 h	1.6 h	>33 days
methanol	12 days	1 yr	>4.5 yr
2-methyl-3-buten-2-ol	2.1 h	8 days	1.7 day
cis-3-hexen-1-ol	1.3 h	4.1 h	6 h
linalool	50 min	6 min	55 min

Table I-8 Calculated Tropospheric Lifetimes for Selected Biogenic VOCs for the reaction with OH Radicals, NO_3 Radicals, and O_3 (Atkinson and Arey 1998).

VOC	OH	NO_3	O_3	Photolysis
Propane	10 day	7 yr	>4500 yr	
n-Butane	4.7 day	2.8 yr	>4500 yr	
Ethene	1.4 day	225 day	10 day	
Propene	5.3 h	4.9 day	1.6 day	
Benzene	9.4 day	>4 yr	>4.5 yr	
Toluene	1.9 day	1.9 yr	>4.5 yr	
Styrene	2.4 h	3.7 h	1.0 day	
Phenol	5.3 h	9 min		
Formaldehyde	1.2 day	80 day	>4.5 yr	4 h
Acetaldehyde	8.8 h	17 day	>4.5 yr	6 day
Benzaldehyde	11 h	18 day		
Acetone	53 day	>11 yr	~60 day	4 day
Glyoxal	1.1 day			5 h
Methylglyoxal	9.3 h		>4.5 yr	2 h
Pinonaldehyde	2.9 h	2.3 day	>2.2 yr	
Methanol	~ 12 day	1 yr		
Ethanol	3.5 day	26 day		
Methacrolein	4.1 h	11 day	15 day	~1 day
Methylvinyl ketone	6.8 h	>385 day	3.6 day	~2 day
Ethyl acetate	6.9 day	10 yr		

Table I-9 VOCs calculated relative lifetimes for photolysis, reaction with the OH radical, NO_3 radical, and with O_3 (Atkinson 2000).

II. EXPERIMENTAL

II.1 Introduction

The exceptional characteristics of the tunable infrared laser diode and the low time constant of the infrared detection with photonic effect (<1µs) spread their utilization in the field of kinetics in the gas phase. Since 1982, research groups have coupled the IR detection together with a photolysis laser used to initiate elementary reactions (Thrush and Tyndall 1982). The combination of these techniques allows recording time resolved signals of absorbing photoproducts created by the photolysis of environmental interesting species. A similar system was developed in Lille by coupling a pulsed UV laser for flash photolysis with an IR spectrometer working in the middle IR (Hanoune, Dusanter et al. 2001).

In this chapter we present in a first part the experimental set-up and in a second part we will focus on the method of data analysis.

II.2 Description of the experimental set-up

The experimental set-up used in the current work is sketched in Figure II-1 and it can be divided into three main parts: the UV beam, the IR beam and the photolysis cell. Each one will be described individually in the chapter.

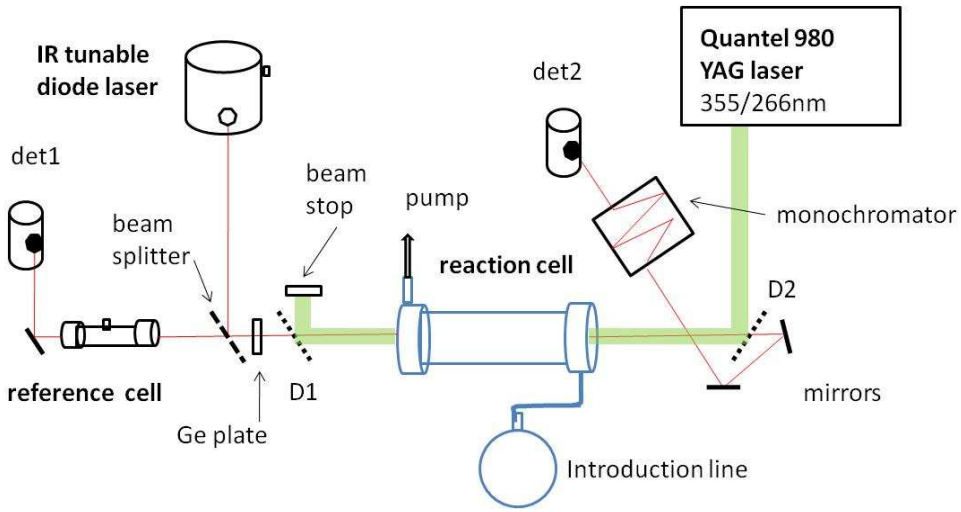

Figure II-1Schematic of the experimental set-up used in the current work and composed of: reaction cell and sample introduction (blue); UV photolysis beam (green) and IR TDLAS detection system (red). Det = detector and D = dichroic mirrors.

II.3 Photolysis beam

The UV beam for the photolysis is generated by a YAG Laser (Quantel model 980). The two principal parts of the laser are: the optical head (Figure II-2) and the power supply. The power supply provides the powering of the optical head and the cooling of the system to evacuate the heat generated by the flash lamps. The optical head is basically composed of the oscillator, the amplifier and the harmonic generator(s).

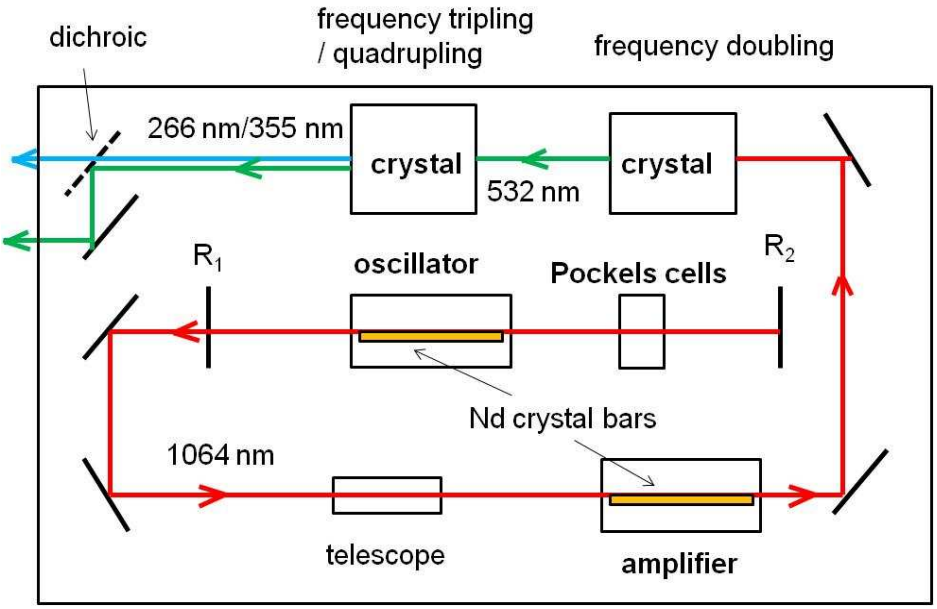

Figure II-2 Schematic of the optical head of the Nd YAG laser model Quantel 980 (R1,R2 = cavity mirrors).

Wavelength	nm	1064	532	355	266
Energy	mJ/pulse	1200	600	280	130

Table II-1 Characteristics of the Quantel YG981C Q-switched Nd:YAG laser for a 10 Hz repetition rate.

- The YAG oscillator

The oscillator consists in a neodymium doped yttrium aluminium garnet crystal rod (115 mm long and 60 mm diameter) and is at the origin of the laser pulse generation. Nd electrons in the ground state are excited to an upper level by optical pumping on the side faces of the crystal bar. The pumping is performed by two flash lamps that flash the crystal rod with a repetition rate of 10 Hz. The relaxation of the excited electros is followed by the emission of a 1064 nm radiation. This radiation is trapped into a cavity, built with one mirror (R_1) coated for the emitting wavelength and an output mirror (R_2) having variable radial reflectivity (which provides a constant density energy profile: top hat beam profile). The laser time diagram is shown on Figure II-3. A Q-switch composed by pockels cells works as a shutter inside the cavity. It is open in synchronization with the maximum of the neodymium fluorescence and sends a pulse of 6 ns duration. The pockels cells can be activated at several frequencies concerted with the 10 Hz flash lamp repetition rate (1, 2, 5, 10 Hz). The flash lamps discharge their pulse with a delay of 175 µs with respect to the electric command occurring in 50 µs. The flash pulse excites the neodymium electrons producing the fluorescence phenomena. The neodymium fluorescence is a photochemical process slower than the pulse of the flash lamps. The Q-switch trigger is sent with a delay of 285 µs, corresponding to the optimal intensity of the neodymium fluorescence process that produces a laser pulse duration of 6 ns.

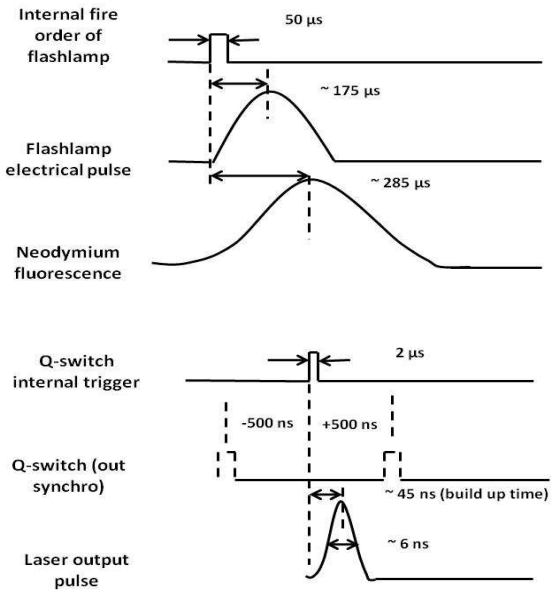

Figure II-3 Laser timing diagram.

- The amplifier

  The near infrared beam at 1064 nm produced in the cavity by the oscillator is firstly enlarged by a telescope and then amplified by a Nd YAG unit. This second amplification element is constituted by a Nd crystal bar pumped by flash lamps with the same repetition rates of the YAG oscillator (10 Hz).

- Harmonic generators

  After the amplification, the infrared beam emission wavelength is doubled by the "Second Harmonic Generator crystal" (SHG). Harmonic generators are made of nonlinear KDP crystals cut at the proper angle depending on the required wavelength. The 532 nm radiation can be tripled or quadrupled by a second KDP crystal unit. To obtain the maximum harmonic conversion these crystals should be carefully phase matched. The phase matching is adjusted by angle tilting for the doubling crystal and adjusted thermally for the tripling/quadrupling crystals.

The UV photolysis beam presents a spot surface of 0.95 ± 0.1 cm^2. The regularity of the shape of the UV beam has been checked daily by impact on a photosensitive paper. Power intensity of the UV beam was measured each two samples to ensure the laser stability. Laser stability has been taken as fundamental criteria for the analysis. The power of the laser pulse was measured at the exit of the laser unit and at the entrance of the cell, in order to evaluate the loss of energy in the optical pathway through the cell.

II.4 Reaction cell

The reaction system presented in Figure II-4 is a simple path cell made of stainless steel with an internal diameter of 3.6 cm and a length of 120 cm. Two CaF_2 windows close the extremities, allowing both UV and IR transmissions. They have been tilted to minimize the optical interferences and the back reflection of the two laser beams. A small nitrogen flow (averagely 20 ml min^{-1}) on the internal side of the windows prevents any deposition of reactants. In addition, two Teflon diaphragms have been placed at each extremity of the cell to minimize the mixing of the sample flow with the protecting one. The two diaphragms have an internal diameter of 1.1 ± 0.1 cm and were placed at 1 cm from the CaF_2 windows (Figure II-4). All around the cell were rolled heating elements (Thermocoax) for the cell thermostatation. Three thermo captors (K type) were installed,

in the center and at each extremity of the cell, with a feedback action on the heating system. In the current work the cell was thermostated at 25 ± 1 °C for the analysis of all molecules, except for hydroxyacetone which has been photolyzed at 60 ± 1 °C. The pressure in the cell was controlled and kept constant by a mechanical pressure regulator (Leybold MR16) placed between the exit of the cell and the pumping system. The pressure was measured with a capacity gauge (Baratron MKS 0-100 ± 1 Torr) that was periodically calibrated (Annex B.1 page 143).

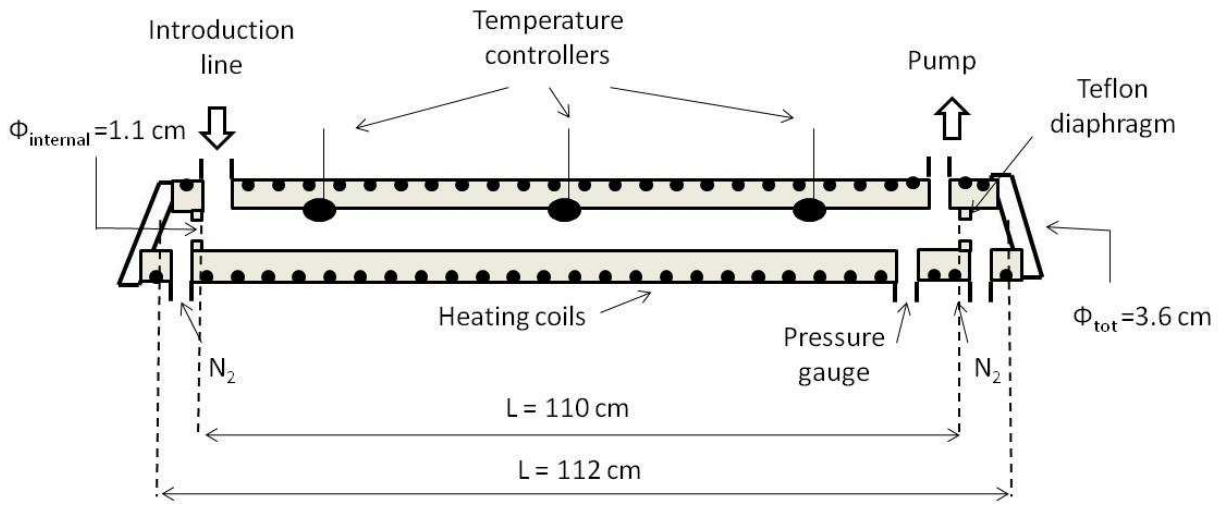

Figure II-4 Schematic of the structure of the reaction cell.

The input flows of the gases were regulated by mass flow controllers that were periodically calibrated and checked with a DRYCAL automatic system (BIOSINT). Its working principle is based on the time required for a frictionless piston to cross a known volume. Two automatic valves are placed at the beginning and at the end of the tube of known volume. When the measurement begins, the outlet valve closes and the gas flow raises the piston through the tube. When the piston terminates its trajectory the reading is complete and an internal processor calculates the flow. The result is immediately displayed on a LCD screen. All mass flow controllers used in this work have been calibrated with the help of the DRYCAL system for both, He and N_2. This instrument assures high precision in the flow estimation with an associated error on the slope of the calibration lower than 0.2%. Calibration stability and calibration curves for each mass flow controller used are reported in Annex B.1 page 143. The input gas flow passed by Low Density Poly Ethylene (LDPE) 6 mm tubes and was pumped at the exit of the cell through a trap cooled with liquid nitrogen to condensate the toxic compounds and to prevent the contamination of the oil of the pump. The buffer gas (N_2 or He) and the chemicals were pre-mixed before their introduction in the cell.

The concentration of stable species in the cell was calculated in the approximation of an ideal gas using the following equation II-1:

$$[M] = \frac{P}{RT} = 9.66 \cdot 10^{18} \frac{P}{T} \qquad \text{II-1}$$

[M] is the total concentration, "P" and "T" are respectively the Pressure (Torr) and the Temperature (K), while "R" is the gas constant (1.034×10^{-19} cm^3 Torr K^{-1}). The concentration [C] of the stable species is calculated from the fraction of the flow of the species "F_i" over the total one "F_t" at a given "P" and "T".

$$[C] = \frac{F_i}{F_{tot}} \cdot 9.66 \cdot 10^{18} \frac{P}{T} \qquad \text{II-2}$$

After each photolysis pulse the gas mixture in the photolyzed volume should be renewed. The renewal rate of the gases through pumping can be calculated as follows: in the approximation of a laminar flow expressed in cm^3 min^{-1} in the standard conditions T_0 = 293 K and P_0 = 1 atm, the refreshing time is given by II-3 :

$$t_e = 60 \cdot \frac{L}{F_{tot}} \frac{P}{P_0} \frac{T_0}{T} S \qquad \text{II-3}$$

were "F_{tot}" is the total flow, "S" is the section of the cell, "L" is the cell length, "T" is the temperature and "P" is the pressure inside the cell.

As an example, the following experimental conditions: F_t = 500 cm^3 min^{-1}; L = 110 cm, p = 30 Torr; T = 298 K and S = 10 cm^2 gave a refreshing time t_e = 5 s. The refreshing of the gas mixture was also due to the radial diffusion of the molecules from the central photolysis beam cylinder to the surrounding wall of the cell. The resulting dilution between each UV flash was in the ratio of the section of the cell over the section of the UV beam (about 10) and occurred in less than 10 ms. A repetition rate of 5 or 2 Hz was chosen in our experiments.

II.5 Samples introduction

The introduction system for the carbonyl compounds was chosen according to their vapour pressure. If it was high enough (several 10 mbar) they could be introduced in the cell after pre-mixing with the carrier gas in balloons (10 L), prepared at a concentration of several percent (3-10%) of VOC (Figure II-5). If the vapour pressure of the compounds at room temperature was too low the VOC was put into a heated flask and brought to the cell by bubbling the carrier gas (He or N_2) through the liquid (paragraph II.5.2 page 41) (Figure II-6).

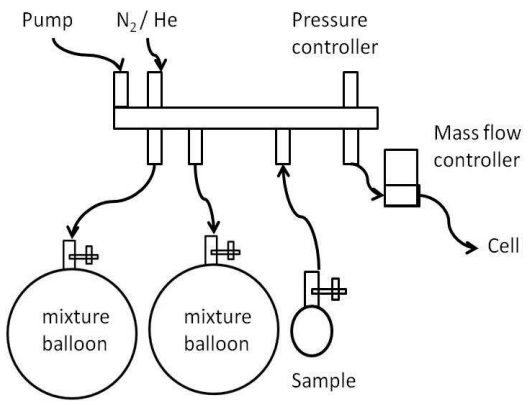

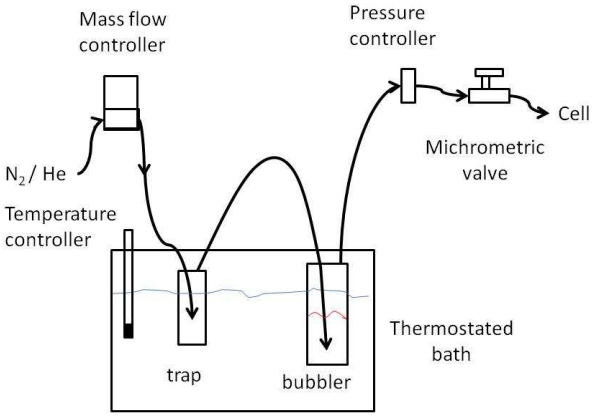

Figure II-5 schematic of the line employed for the sample preparation. The glass balloons directly connected to the line were black covered for a best conservation of the samples.

Figure II-6 simplified scheme of the introduction of sample with the method of the bubbler. The transport gas and the sample are pre-heated in a thermostated bath before their introduction in the photolysis cell.

II.5.1 Introduction system for VOC with high vapour pressure

The preparation of gas mixtures with known concentrations of VOC in balloons can be applied to all volatile compounds and is largely used in gas kinetic studies for its characteristics:

- Universal for all volatile compounds
- Easy preparation of the samples at different, reproducible concentrations
- Use of a flow meter to adjust the flow

After careful removal of dissolved air from the liquid carbonyl sample by pump and freeze cycles, the balloon was filled with vapour of the carbonyl compounds up to a given pressure, limited by the

vapour pressure of each molecule (Figure II-5). In order to reproduce the same photolysis condition for all molecules, balloons were prepared introducing 30 Torr of carbonyl compound and completing it with He or N_2 up to 1000 Torr. Finally, the concentration of the VOC in the balloon results as the fraction of the pressure introduced on the total pressure reached (II-4).

$$C = \frac{P_{voc}}{P_{tot}} \qquad \text{II-4}$$

where "P_{voc}" is pressure of VOC (Torr), "P_{tot}" is the final pressure (Torr).

The introduction of the mixture in the cell was regulated by a flow meter. The calibration of the flow meter, made for N_2, was not anymore valid because, in the presence of high VOC concentrations, the heat capacity of the gas increased and thus changed the thermal resistance of the filament of the flow meter. Therefore, flow meters were calibrated for the gas mixtures by measuring the time required to increase the pressure in a calibrated volume. The time Δt needed to increase the pressure p in a given volume was first measured with pure N_2 at a given flow F_0, admitted through a calibrated flow meter. The rate $\Delta p/\Delta t$ is related to the flow F_0. The time needed to increase the pressure in the same volume was then measured using the gas mixture delivered through the flow meter to be calibrated. The measured flow is then given by (II-5):

$$F = F_0 \frac{(\Delta P / \Delta t)_1}{(\Delta P / \Delta t)_0} \qquad \text{II-5}$$

This way it is possible to calibrate flow meter with a gas containing a given concentration of a VOC.

II.5.2 Introduction system for low vapour pressure compounds

The introduction system for compounds with low vapour pressure, sketched in Figure II-6, consists in a bubbler heated in a thermostated bath. The transport gas, regulated by a mass flow controller (2000 SCCM), brought the VOC vapours through the heated line where it was diluted by the main bath gas flow. A trap situated in the thermostated bath had a double purpose: to pre-warm the carrier gas before entering the bubbler and prevent any back-flow of liquid to the flow meter in case of a mistake in manipulation of the gas handling system. The pressure (P_b) inside the bubbler was chosen in the range 300 - 600 Torr and was controlled by throttling a needle valve placed at the exit of the bubbler. The pressure was measured by a pressure gauge Tylan General (0-1000 ± 0.1 Torr). The flow of carbonyl compound $D_{mixture}$, at the exit of the bubbler, was calculated using equation II-6, assuming that the carrier gas was saturated with the vapour pressure of the VOC and that the mixture could be described as an ideal gas:

$$F_{mixture} = \frac{P_b}{P_b - V_p} \cdot D_{N2} \qquad \text{II-6}$$

where "$F_{mixture}$" is the VOC flow + the transport gas; "D_{N2}" is the input N_2 flow; "P_b" is the pressure inside the bubbler, "V_p" is the vapour pressure.

The temperature of the organic compound inside the bubbler was taken as the temperature of the thermostated bath, which is not exactly the case. The value of the vapour pressure taken into account was consequently slightly higher and the flow of the VOC thus overestimated. We expected the VOC flow to be known within an error of ± 10%. A previous study made by Christensen, using such an introduction system for methanol found an agreement of 10% between the calculated flow and the measured one (Christensen, Okumura et al. 2006).

II.6 Detection system

Detection was performed by IR with the technique of Tuneable Diode Laser Absorption Spectroscopy (TDLAS). The IR beam was generated by a diode laser. Diodes are semiconductors (type p-n junctions) that generate laser emission when they are stimulated with current. The applied current pumps electrons from one band to the other, inducing a difference of population. The return at the normal distribution is followed by the emission of a radiation hν proportional to the gap difference (Figure II-7).

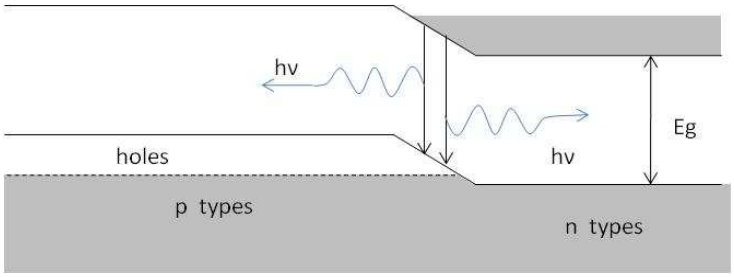

Figure II-7 General representation of a p-n semiconductor generating laser radiation for the return of excited electron at the ground state with emission of a radiation equivalent to the Electronic Gap (Eg).

Diode lasers are widely spread on the market of telecommunications and electronics (laser printers and CD players) because of their small size, ease of use and high reliability. They are divided in four major families, depending on their nature: gallium arsenide, indium phosphite, antimonides and lead salts. Semiconductor emission cover the spectral range from visible to infrared (Figure II-8).

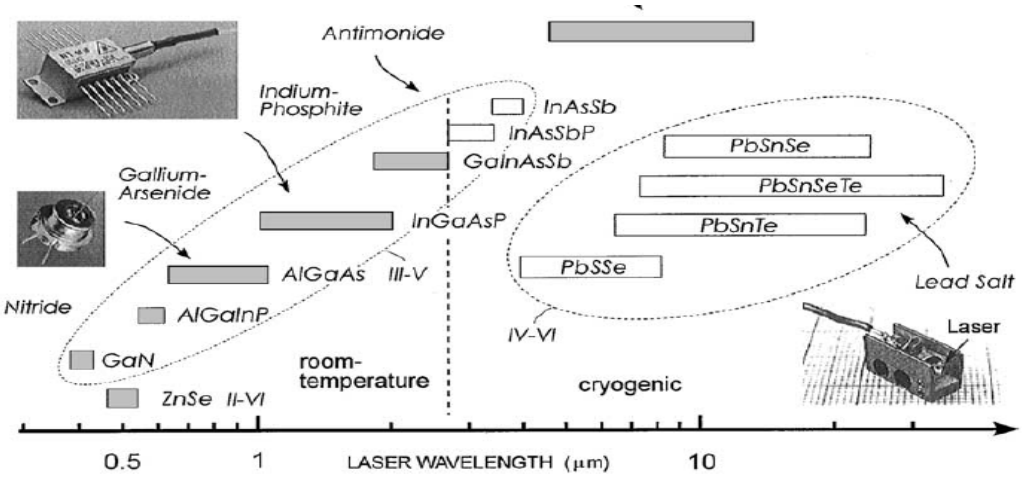

Figure II-8 Overview of the different semiconductors diodes and their spectral emissions (Werle, Mucke et al. 1995).

Lead-salt diodes allow working in the mid-IR in the spectral range from 30 to 3000 cm^{-1} where atmospheric molecules have fundamental absorption bands presenting strong absorption cross sections. In addition the tune ability of the lead-salt diode makes TDLAS a powerful tool for kinetic studies. With this technique it is possible to tune the wavelength on small intervals (some cm^{-1}) by varying the applied current (Werle, Mucke et al. 1995). In addition, diode lasers have a linewidth emission of about 10^{-3} cm^{-1}, an order of magnitude lower than typical linewidths at pressures used in this work (30-90 Torr), allowing even to observe absorption lines in the Doppler limit profile.

II.6.1 Tuneable Diode Laser Absorption Spectroscopy (TDLAS) set-up

The IR beam generated by the diode was split in two parts, one part was directed to a reference cell, used to stabilize the emission wavelength, the other to the photolysis cell (Figure II-9). Both absorption paths are composed of the same elements, except for the monochromator placed in the detection path, used for filtering the wavelength. The elements composing the reference and the detection lines are shown in Figure II-9.

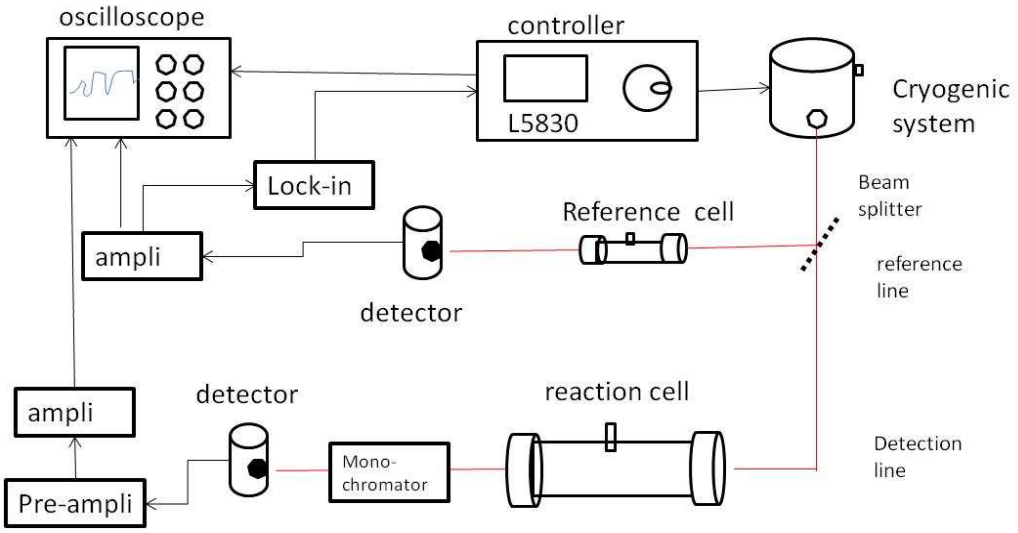

Figure II-9 Schematic of the experimental set-up of the detection line for the TDLAS technique coupled with a reference line for the wavelength stabilization.

The diode laser support (model L5376) is cryogenically cooled with liquid N_2, which is typical for lead-salt diode lasers working in a temperature range over 80 K. The diodes are mounted under vacuum on a heated coil finger which can be regulated from 80 to 120 K, depending on the diode laser operating specification. The vacuum chamber had to be periodically evacuated to ensure high thermal isolation. The frequency of this operation was indicated by the laser controller that

displayed the thermal stability inside the chamber. The TDL controller (model L5376) is the device that is connected to the diode laser and controls the current injection to the diode. The applied current depends on the diode type, and was in our case comprised between 500-1000 mA.

The laser crystal is very small and the output beam is highly divergent, therefore it has to be collimated by a parabolic mirror. The beam is directed through the photolysis cell by two plane, silver coated mirrors. The alignment of the IR beam was carefully checked at the beginning of every experiment with the help of two diaphragms centred on the two windows of the cell. A wavelength determination was made possible by a grating monochromator (photonics L5100-6 µm). Due to the fact that our diode lasers (for CO and H_2CO) are mono-mode, the monochromator mainly filters parasite radiations, incoming to the photosensitive surface of the detector such as UV and VIS (visible) light, coming from unwanted reflections, thermal IR radiation and possible fluorescence induced by excitation of impurities on the windows through the photolysis laser.

The IR beam was focused on the photovoltaic InSb LN2-cooled detector (Fermion Corps model PV-6-500). The electric signal was amplified by a pre-amplifier (EG&G INSTRUMENTS 5184) followed by an amplifier (Fermion Corps model PVA-500-5). The signal is acquired by an oscilloscope interfaced with a PC. The oscilloscope (Tektronix TDS 520B) has a passing band of 500 MHz and a sampling power of 1 Gigasignal/s on two channels. The oscilloscope was triggered by a photodiode placed at the end of the UV line and signals were finally transferred to the computer through a GPIB interface and processed with a Labview program.
A small part of the IR beam (10%) was directed to the reference cell (Figure II-9), a glass tube 20 cm long, filled with CO or H_2CO (≈ 10 Torr). The IR beam passing through the reference cell is sent to an amplifier connected to the oscilloscope. This signal was used for the stabilization of the laser emission frequency at the center of an absorption line. This was achieved by modulating of the incoming IR signal by a 18 kHz sine wave. The reference cell signal was then demodulated by a lock-in amplifier which yielded a correction sent to the input of the laser power supply. Any shift in the frequency emission was detected as a variation on the derivative signal and corrected with a feedback signal sent to the diode power supply.

II.7 CO and H_2CO Detection with TDLAS

In the following part we present the time resolved absorption spectroscopy (TDLAS) and the procedure chosen to monitor CO and H_2CO.

II.7.1 IR absorption spectroscopy

Absorption spectroscopy can be used for the quantitative detection of species using the Lambert Beer law (II-7):

$$T(\nu) = \frac{I_t}{I_0} = \exp(-\sigma_\nu \cdot l \cdot [C]) \qquad \text{II-7}$$

where "T(ν)" represents the transmission, "[C]" is the concentration of the absorbing molecule, "l" the length of the optical path, "I_t" and "I_0" are respectively the IR intensity with and without absorbing species. "σ_ν" is the absorption cross section at the frequency ν (cm^2). The absorption cross section σ_ν at a given wavelength can be expressed with the integrated intensity "S" of the absorption line (II-8):

$$\sigma_\nu = S \cdot f(\nu - \nu_0) \qquad \text{II-8}$$

where the function "$f(\nu-\nu_0)$" describes the integrated profile with an imposed condition of normalization (II-9):

$$\int_{-\infty}^{+\infty} f(\nu - \nu_0) d\nu = 1 \qquad \text{II-9}$$

The function "f(ν)" can be rewritten as equation II-10 if we introduce a coefficient of normalization "a", while "φ(ν)" is a mathematical function of the profile with $\varphi(\nu_0) = 1$.

$$f(\nu) = \frac{1}{a} \cdot \varphi(\nu - \nu_0) \qquad \text{II-10}$$

If the wavelength emission is centred on the absorption line then the function "f(ν)" simply depends on the normalization factor (II-11).

$$f(\nu) = \frac{1}{a} \qquad \text{II-11}$$

II.7.2 Cross section calculation

From equations II-8 and II-11 it can be seen that the cross section "σ" is defined as the ratio of the integrated intensity "S" over the normalization factor "a":

$$\sigma = \frac{S}{a} \qquad \text{II-12}$$

Equation (II-12) shows that the absorption cross section "σ" depends linearly on the integrated intensities of the peak (expressed in cm molec^{-1}), tabulated for atmospheric pressure. For CO lines this information was taken from the "wave number calibration tables for heterodyne Frequency measurements" NIST Special Publication 821 (Maki and Wells 1998). The line intensity "S" is independent of the pressure but changes with temperature following the Boltzmann distribution of the population level of energy (II-13):

$$S(T) = S(T_0)\left(\frac{T}{T_0}\right)^z \exp\left(\frac{E^1}{k}\left(\frac{1}{T_0}-\frac{1}{T}\right)\right) \qquad \text{II-13}$$

where "T_0" is the reference temperature (298K), "E^1"is the energy of the lower level, "k" is the Boltzmann constant, "z" is a parameter depending on the structure of the molecule (for CO and for all linear molecules z=1).

The normalization factor "a" of equation II-12 is a function of the Voigt profile (II-14).

$$a = 2 \cdot \Delta\nu_{voigt} \cdot (1.065 + 0.447r + 0.058r^2) \qquad \text{II-14}$$

The Voigt profile is a combination of the effects of two profiles (Doppler and collisional) on the absorption line profile (Olivero and Longbothum 1977) (II-15).

$$\Delta\nu_{voigt} = \frac{1}{2}(1.0692 \cdot \Delta\nu_{coll} + \sqrt{0.86639\Delta\nu^2{}_{coll} + 4\Delta\nu^2{}_{dopp}}) \qquad \text{II-15}$$

The parameter "r" in equation II-14 is defined as the ratio of the collisional over the Voigt profile.
The collisional profile is a good estimation of the line profile at high pressure while the Doppler profile is better adapted at low pressure (Figure II-10). In the intermediate range such as in our experiments both broadening processes coexist and are described by the Voigt profile which is a combination of the collisional and Doppler (Olivero and Longbothum 1977).

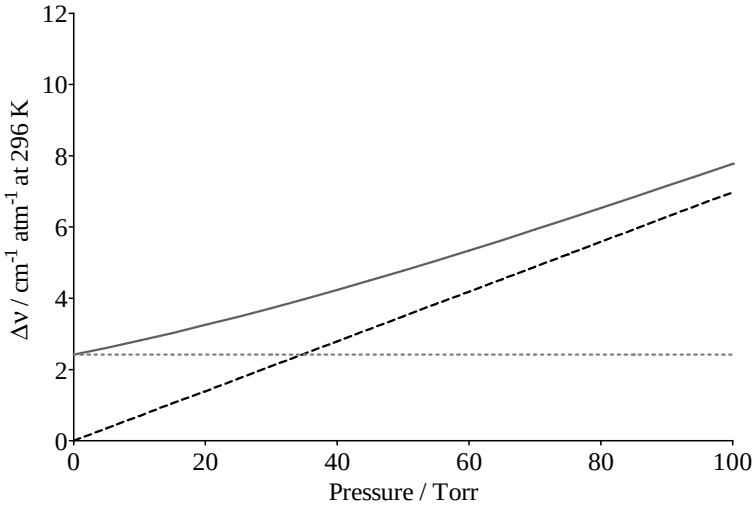

Figure II-10 Resulting broadening of CO at 2082cm^{-1} in N_2 in a pressure range 0-100 Torr. Voigt profile (plain line), collisional profile (dashed line), Doppler profile (point line).

Doppler and collisional profiles, needed for the calculation of the normalization factor "a" appearing in equation II-15, will now be approached separately.

1. Doppler broadening

In a gas sample at thermal equilibrium at a temperature "T", the velocity of a molecule follows the Boltzmann distribution law and as a consequence the line is enlarged symmetrically around the value "ν_0", following a Gaussian distribution of the velocity (II-16).

$$f_D(\nu-\nu_0)=\frac{1}{a}\cdot\exp\left(-\left(\frac{\nu-\nu_0}{\Delta\nu}\right)^2\right) \qquad \text{II-16}$$

The Doppler profile is characterized by its full width at half maximum:

$$\Delta\nu_{dop}=\frac{\nu_0}{c}\sqrt{\frac{2KT\ln 2}{M}}=3.58\cdot10^{-4}\sqrt{\frac{T}{M}}\cdot\nu_0 \qquad \text{II-17}$$

where "M" is the molecular mass of the molecule and T is the temperature (K).

1. Pure collisional broadening

Collisions between molecules generate a perturbation in the interaction radiation-matter. Those collisions are described by the Poisson law and result in a widening linear with the pressure and with a Lorentzian profile:

$$f_L(\nu-\nu_0)=\frac{1}{\pi\cdot\Delta\nu_{coll}}\cdot\frac{1}{\frac{(\nu-\nu_0)^2}{\Delta\nu_{coll}}+1} \qquad \text{II-18}$$

$\Delta\nu_{coll}$ is proportional to the pressure and depends on the broadening coefficient γ which is specific to each collision partner (II-19):

$$\Delta\nu_{coll}=\gamma\cdot P \qquad \text{II-19}$$

For a gas mixture, this results in the combination of the component of each gas.

$$\Delta\nu_{coll-mix}=\gamma_0\cdot p_0+\sum\gamma_i\cdot p_i \qquad \text{II-20}$$

where "γ_0" and "p_0" represent the self broadening of the main gas and "γ_i" and "p_i" is the broadening given by the other gases. In our case, considering the high dilution of the absorbing molecules, we can assimilate the photolysis mixture to a hypothetic pure flow (N_2 or He) and as a consequence we applied equation II-19 instead of II-20.

The concentrations can be calculated from the variation of the intensity "I" and "I_0" using equation II-21.

$$[C]=\frac{\ln\left(\frac{I_0}{I_0-I}\right)}{\sigma_\lambda\cdot l} \qquad \text{II-21}$$

The intensity of the diode emission "I_0" is obtained by placing a chopper in the detection line. The motion of the chopper cuts off regularly the IR beam generating a square signal (Figure II-11). The difference between the maximum and minimum intensity represents "I_0".

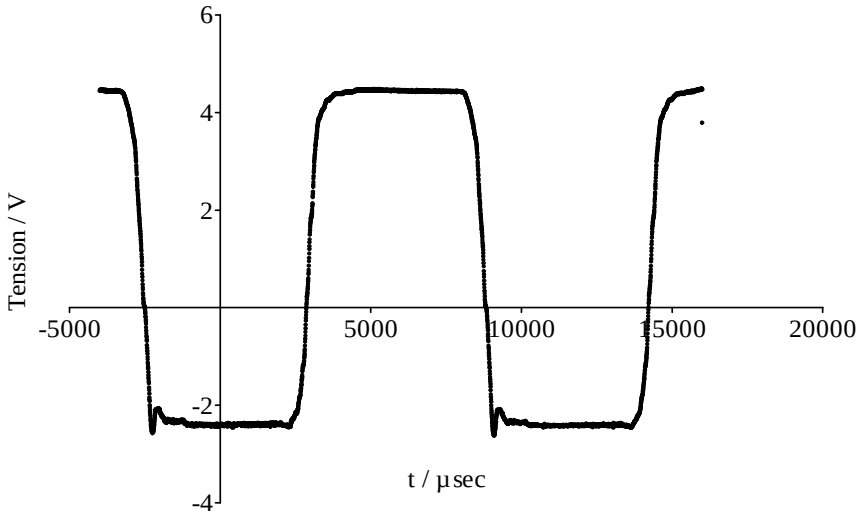

Figure II-11 Example of the IR signal recorded for the determination of I_0.

II.7.3 IR detection procedure

It was observed in the course of the measurement that the sensitivity depend on the position of the IR beam with respect to the position of the UV beam, in particular concerning the shape of the temporal IR signal recorded for the kinetics. The alignment, complicated by the strong astigmatism of the IR diode laser beam, has been checked by placing two diaphragms front of the windows on each extremities of the cell. Control of the reciprocal alignment was verified weekly to ensure the reproducibility of the measurements.

The time resolved CO and H_2CO measurements were performed according to the following procedure.

- ✓ Record of the baseline off the absorption line.
- ✓ Search of the wavelength of the absorption line centre using the reference cell.
- ✓ Stabilization of the diode laser emission on top of the absorption line.
- ✓ Record of the kinetic as the average of several photolysis pulses.
- ✓ Analysis and fit of the collected signals

The baseline has been recorded by setting the emission of the IR diode away from the absorption line of the detected molecule. An example of the baseline is reported in Figure II-13 (gray line). The baseline is used to remove systematic interferences affecting the signal.

The search of the wavelength of the absorption line has been performed introducing 10 Torr of pure CO or H_2CO in the reference cell. The current applied to the IR diode laser was then set to achieve the centre of the absorption line and the emission was stabilized on that wavelength by a first derivative frequency lock-in procedure (paragraph II.6.1 page 43). The assignment of a line was checked using the monochromator (± 1 cm^{-1}) and by comparison with the GEISA database (Jacquinet-Husson, Scott et al. 2008).

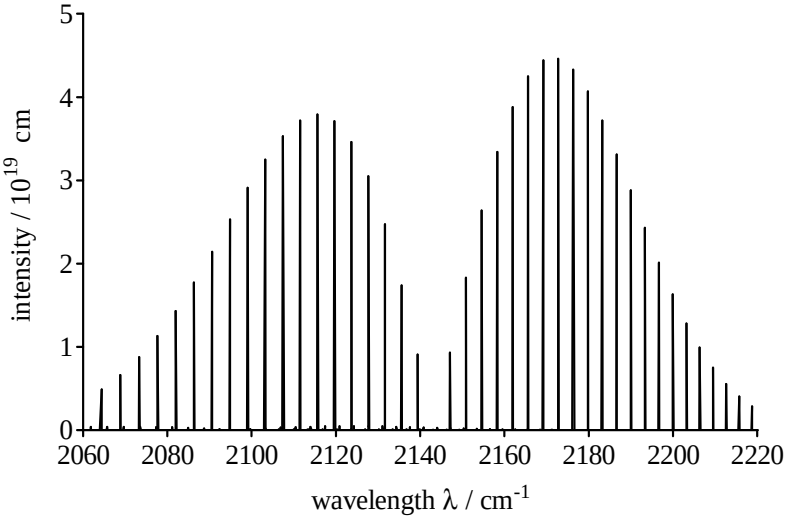

Figure II-12 Intensity of the CO absorption lines at 296 K, from GEISA database (Jacquinet-Husson, Scott et al. 2008) .

In the current work we performed analysis at different wavelengths, choosing always the most intense absorption line accessible in the diode laser emission range. The absorption lines used for CO were 2136, 2099, 2082, 2111 and 2115 cm^{-1} (Figure II-12). For H_2CO, all measurements were performed at 2820 cm^{-1}.

λ	S	γ	Rotational assignment
cm^{-1}	*$cm^{-1}/molec.cm^{-2}$*	*cm^{-1} atm^{-1}*	
2136	1.74×10^{19}	0.0728	P(2)
2099	2.91×10^{19}	0.0579	P(11)
2082	1.43×10^{19}	0.0553	P(15)
2111	3.72×10^{19}	0.0599	P(8)
2115	3.79×10^{19}	0.0611	P(7)

Table II-2 Intensity, broadening coefficient and rotational assignment for the CO absorption lines used in the current work. Data refers to air at atmospheric pressure and 296 K, according to the GEISA database (Jacquinet-Husson, Scott et al. 2008)

To increase the signal-to noise ratio and to remove parasites and interferences from the absorption signal, two different methods have been used. Random noise was attenuated by averaging signals with the numerical oscilloscope. Depending on the signal-to-noise ratio and on the laser repetition rate, up to 500 signals were averaged. Two systematic parasites have been observed: an intense peak in the first few µs was generated electronically by the photolysis laser (probably discharge of flash lamps). It can be seen in Figure II-13 that it occurs in both, the baseline and in the absorption signal. It can be eliminated by subtracting the baseline from the absorption signal.

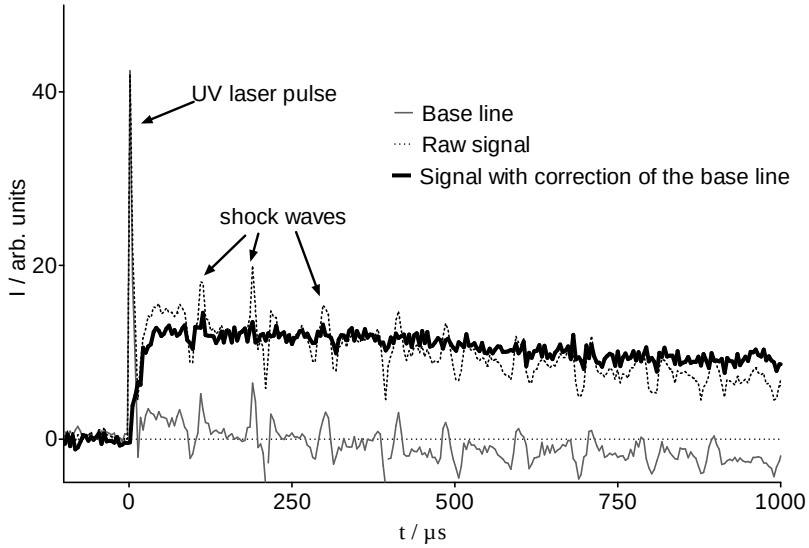

Figure II-13 Typical signal (voltage expressed in mV): on the center of the absorption line (dash line) and away from the line (gray line) and the relative subtraction (dark line).

Another parasite in form of regular oscillations (Figure II-13) was visible all along the signal. These interferences are probably due to shock waves, caused by a radial expansion of the gas induced by heating after absorption of the UV laser pulse. These waves, originating in the centre of the cell, bounce back on the walls and come back. The density of the gas and thus the refractive index changes and this phenomenon created small deviations of the IR beam. The nature of this parasite can be evaluated calculating the time laps between two shock waves. For example, in Figure II-14 the interval is 100 µs, corresponding to the time required to cover twice the radius of the cell (see Figure II-14). The velocity v of this shock wave can be calculated as (II-22):

$$v = \frac{(r_{cell} \cdot 2)}{\Delta t_{shockwave}} = \frac{(1.8[cm] \cdot 2)}{1 \cdot 10^{-4}} / 100 = 360 m\,s^{-1} \qquad \text{II-22}$$

This value, compatible to the speed of sound, confirmed that the wave was due to a gas expansion. In Figure II-13 we see that the parasite appears on both the baseline and the absorption line but it is efficiently removed by subtraction.

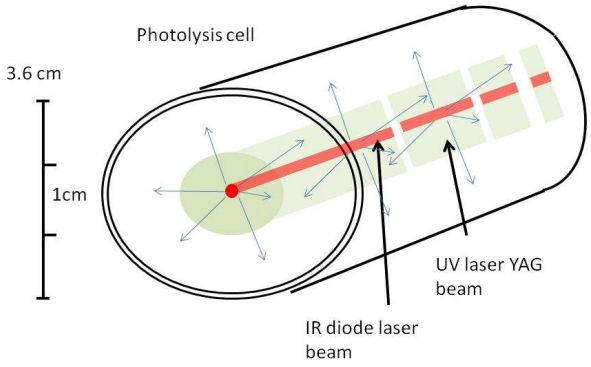

Figure II-14 Radial propagation of the shock waves respect to the photolysis and IR beam.

The records of the transient profiles of CO in the vibrational excited states were performed without stabilization since at room temperature the concentration of vibrationally excited CO is very low and the absorption lines were too low to be used as a reference. However, the position of lines of CO v = 1 were easily found because their intensity was just above our detection limit when pure CO was introduced in the long cell. For CO in upper states (v = 2 and v = 3), the line positions are tabulated in the GEISA database (Jacquinet-Husson, Scott et al. 2008), but it was not possible to detect them even with large amount of pure CO in the long cell. To tune the emission of the diode laser to a line of CO in the states v = 2 or v = 3, the following procedure was used. The emission wavelength was first tuned on a detectable line of CO (which could be a line of CO or a line of an isotopic species in v = 0) close to the target line. A Fabry Perot interferometer, made of a germanium bar, was then introduced in the IR beam. At a given wavelength, the difference between two fringes is known. For example, at 2099 cm^{-1}, it is 0.0471 cm^{-1}. Sweeping the wavelength of emission, the fringes scrolled on the oscilloscope screen. By counting the number of fringes, the laser emission was moved from the position of the known line to the expected position of a v = 2 or v = 3 line. The final tuning was obtained by monitoring the line when a VOC was photolyzed in order to get the better S/N ratio.

The calculation of the CO concentration in the excited states has been performed slightly differently because the absorption cross section should be estimated. Seen that the intensity of a line is:

$$I = \sigma \cdot D^2 \cdot (N'' - N') \qquad \text{II-23}$$

where D is the dipolar moment and (N"-N') is the difference in population between two sequent energetic levels. Considering that N">>N' , the expression can be reduced to:

$$I = \sigma \cdot D^2 \cdot (N'') \qquad \text{II-24}$$

Knowing that the dipolar moment is a function of the vibration effect we can resume for the different vibration states the following conditions (Table II-3).

state	*v=0*	*v=1*	*v=2*	*v=3*
D	0.1765	0.1521	0.1861	0.2146
D_i^2/D_o^2	≈1	≈2	≈3	≈4

Table II-3 Dipolar moment of the CO vibrational state and ratios respect to state the v=0.

The Table II-3 resumes the dipolar moment for an example created for one line of intensity R5. If we search the absorption cross section for a vibrational state v=2 with intensity R5 we will have:

$$\sigma(R5, v=2) = \sigma(R5, v=0) \cdot \frac{D_i^{\,2}}{D_0^{\,2}} \cdot (N'') \qquad \text{II-25}$$

But as the population distribution is given by the Boltzmann distribution and we are at the same condition for both absorption cross sections, the resulting absorption coefficient will be simply dependent from the ratio of the two dipolar moments at the two states.

II.7.4 Data evaluation procedure

In the current work two different types of time resolved signals have been observed. In this paragraph the two typologies are approached separately with respect to the two different fitting equations used.

The signal presented in Figure II-15 represents an example of the type of signal that has been recorded during the detection of H_2CO in the photolysis of hydroxyacetone (paragraph IV.8 page 94). Similar profiles have been encountered also in the detection of CO during the photolysis of acetyl bromide (paragraph II.8.2 page 61) .

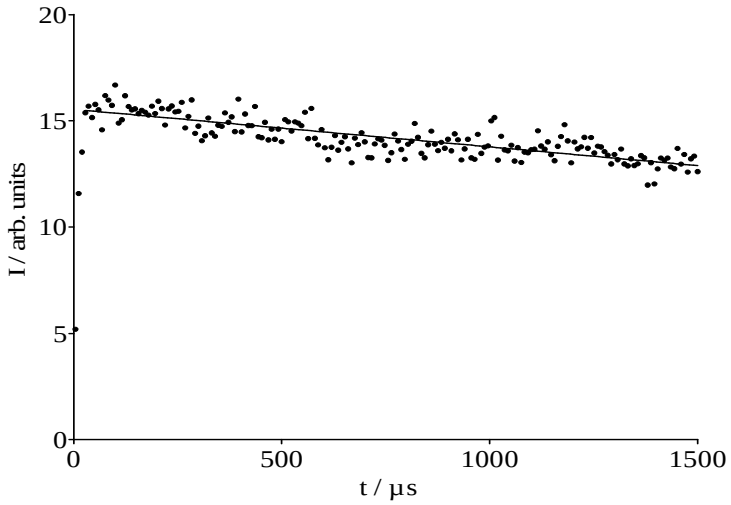

Figure II-15 H_2CO signal from the photolysis of hydroxyacetone in N_2 with $[CH_3COCH_2OH] = 7.23\times10^{15}$ molec cm^{-3}

Here, a rapid rise of the signal is observed in the first 20 µs. This fast rise was at least partially due to the time constant of the experimental set-up and was considered immediate on our time scale. The decay, due to diffusion, could be approximated as linear and hence the intercept a of a linear regression was considered for the calculation of the concentration of molecules formed immediately after the photolysis pulse.

The second typology of signal that has been recorded in the detection of CO after photolysis of acetone, methylvinylketone, hydroxyacetone, 3,3,3-trifluoro propionaldehyde and acrolein (chapters III, IV, V, VI, VII); a typical example is shown in Figure II-16.

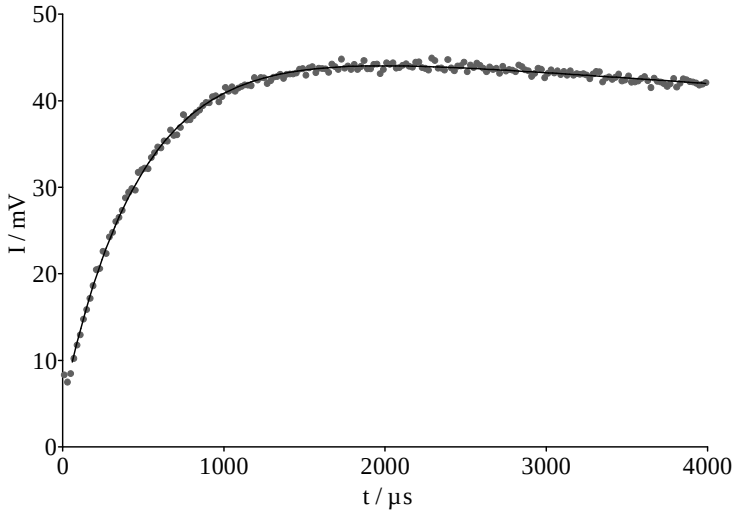

Figure II-16 CO signal from the photolysis of 3,3,3-trifluoro propionaldehyde in N_2 at 30 Torr with $[CF_3CH_2CHO] = 5.1\times10^{15}$ molec cm^{-3}.

This type of signal consists in a fast and almost instantaneous increase of the concentration of CO, followed by a slower formation. In order to evaluate the two different components: CO formed directly in the first 20 µs (called CO_{direct} in II-26) and CO formed in the following kinetic process (called $CO_{secondary}$ in II-26), we fitted the curves with an exponential equation including an offset.

$$[CO] = \left([CO]_{direct} + [CO]_{secondary} \times \left(1 - e^{-k \cdot t}\right)\right) \times \left(e^{-kdiff \cdot t}\right) \qquad \text{II-26}$$

where the kinetics occurs at a rate k and k_{diff} is the diffusion rate, introduced to take into account the diffusion of photolysis products out of the photolyzed volume. The empirical values for k_{diff} were found to be $k_{diff,N2} = 80\ s^{-1}$ in N_2 and $k_{diff,He} = 300\ s^{-1}$ in He, at a pressure close to 30 Torr.

II.7.5 Evaluation of the uncertainties

In the following, we discuss the contributions of the parameters appearing in equation II-21 and the uncertainty on the [CO] measurement.

- "l", the length of the cell:

Its uncertainty is due to the difficulty in the exact determination of the path length (110±1cm), *i.e.* the portion of the photolysis cell containing the VOC. This uncertainty is introduced by the use of protection flows in front of the CaF_2 windows, necessary to prevent the deposition of photolysis products. This uncertainty it is hardly estimable because highly dependent on the flows. It is nevertheless considered to be less than 3%.

- "σ_{IR}" the absorption cross section:

The calculation of the absorption cross section of CO has been performed (paragraph II.7.2 page 46) on the base of the line intensity tabulated on the GEISA database (Table II-2) (Jacquinet-Husson, Scott et al. 2008). The IR integrated intensity (S) of CO lines and broadening parameters are well tabulated in GEISA database, but the accuracy is not always well determined. Another component affecting the uncertainty associated to the cross section is directly linked on the broadening (γ) of the line. In this work we used the broadening parameters with N_2 and He as buffer gas (Sinclair, Duggan et al. 1997; Sinclair, Duggan et al. 1998). In addition, collisional broadening with the precursor gas was not take into account (even if it is not negligible) because no data are available in literature. Taking into account this two contributions, the uncertainty (u_σ) on the absorption cross section can be estimated to u_σ = 10%. Certainly this parameter is one of the most influent in the whole calculation of the extended uncertainty on the CO measurements.

- "I" the IR diode intensity:

The contribution of the laser diode intensity plays a minor role in the uncertainties for the CO determination and it is estimated to be almost negligible: even though the observed absorptions are rather small (a few % maximal), a change in the diode laser intensity has only a minor impact on the results, because the baseline is always measured and subtracted to the signal just before the photolysis pulse.

Also the application of the modulation during the signal detection can introduce a minor source of uncertainty. In fact, the amplitude of the sinus wave modulation of the wavelength of the IR laser is low enough compared with the CO linewidth to be considered negligible for the absorption measurement.

In order to verify the detection procedure and the measurement of CO concentration during kinetic experiments, we decided to perform two different tests based on the measurement of known, stationary CO concentrations (Air Liquid, 99% purity) in the cell. A balloon of CO in N_2 at a suitable concentration (0.01%) was prepared and variable flows of the mixture were introduced in the cell through a flow meter. In the first method the CO concentration was measured from the integrated intensity of the CO absorption line, while in the second one is was measured from the transmittance of the IR signal.

1. *Measurement of the integrated intensity of the absorption line*

The intensity of the transition was obtained by scanning the IR wavelength over the absorption profile by applying a smooth modulation. The line profile was recorded and the amplitude of the CO line was obtained after subtraction (Figure II-17).

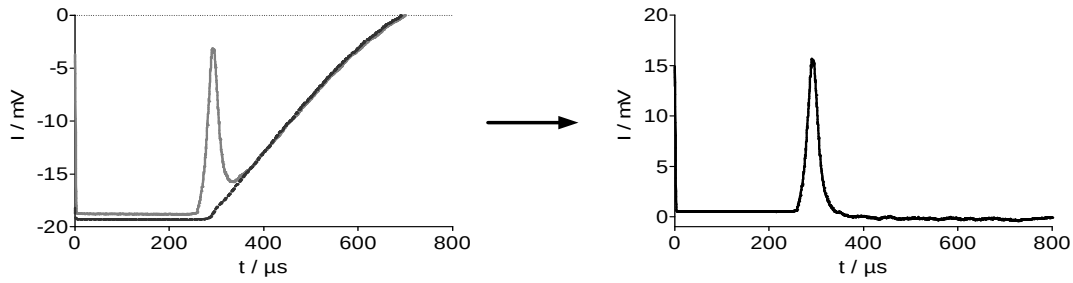

Figure II-17 Signals recorded recorded applying the modulation (gray line) and the resulting signal (dark line) after subtraction of the baseline (dashed line).

2. *Measurement of the variation of the diode laser intensity*

In this method, we measured the CO concentration as the variation of the diode laser intensity (with the diode stabilized on the centre of the absorption line). The absorbing molecules present in the cell reduce the IR signal proportionally to their concentration (II-21).

The CO concentration was measured on the CO absorption line at 2115 cm^{-1} at a pressure of 30 Torr. The CO absorption cross section for the calculation of the CO concentrations used in the two different methods was $\sigma_{2115} = 2.27\times10^{-17}$ cm^2 $molec^{-1}$. In Figure II-18, the CO concentrations obtained with both methods are plotted versus the introduced concentrations, determined from the flows and pressure. The good agreement of the concentrations obtained with both methods (slopes of 1.001 and 1.137 are obtained) gives confidence for the reliability of the CO measurements during time resolved experiments. From the difference of the two curves we can evaluate the overall uncertainty on our CO measurements to be better than 14%.

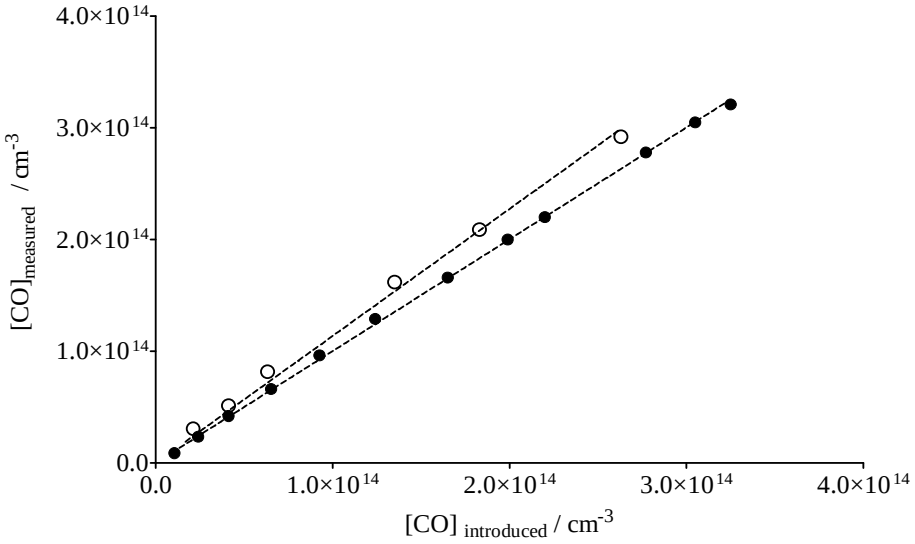

Figure II-18 Check of reliability of the CO measurement though measurement of a known CO concentration with two different methods: variation of the diode laser intensity (I_0) (full symbols, m=1.001) and measurement of full line through modulation (open symbols, m=1.137).

II.8 Fluence

II.8.1 Estimation of the fluence of the UV beam

The fluence is a crucial parameter for the determination of the quantum yield and represents the energy density in a delimited area. In the current work, the fluence was determined from the energy and the area of the UV photolysis beam ($0.95 \pm 0.1 cm^2$) using the equation II-27:

$$F = \frac{E \cdot \lambda}{S \cdot h \cdot c} \qquad \text{II-27}$$

where "E" is the laser energy (J $pulse^{-1}$), "λ" is the wavelength, "S" is the surface of the laser spot (cm^2), "h" is the Planck constant and "c" is the speed of light. The two fundamental parameters in the fluence determination with equation II-27 are the surface "S" and the laser energy "E". Both will be discussed in the following paragraphs.

II.8.1.1 Control of the laser beam spot "S"

The surface was regularly checked by printing a single laser pulse on a photosensitive paper in front of the window of the cell (*i.e.* just before the beam enters the cell). The impression of the beam was accurately verified to ensure that the shape of the beam was round. The diameter was 1.1 cm, measured with an accuracy of ± 1 cm, *i.e.* the section area was $S = 0.95 \pm 0.14$ cm^2.

The top hat of the laser beam was also checked with a camera recording the fluorescence produced by a white sheet of paper illuminated by the laser beam at 266 nm or 355 nm (Figure II-19 and Figure II-20, right).

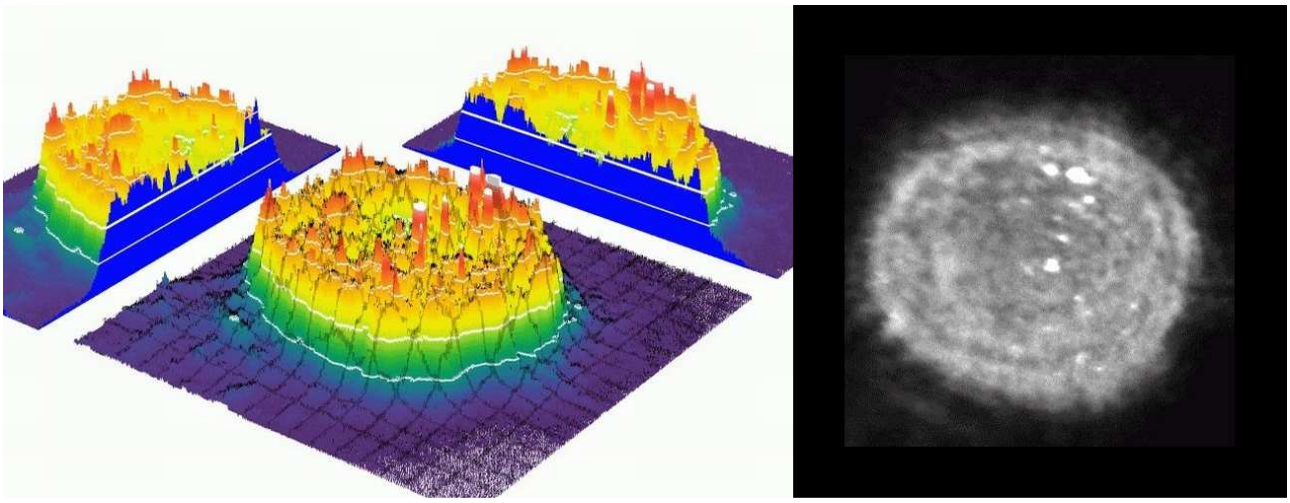

Figure II-19 Profile of the 266 nm beam laser spot modeled with the software IRIS to create a 3D picture (left) from the fluorescence recorded with a camera (right).

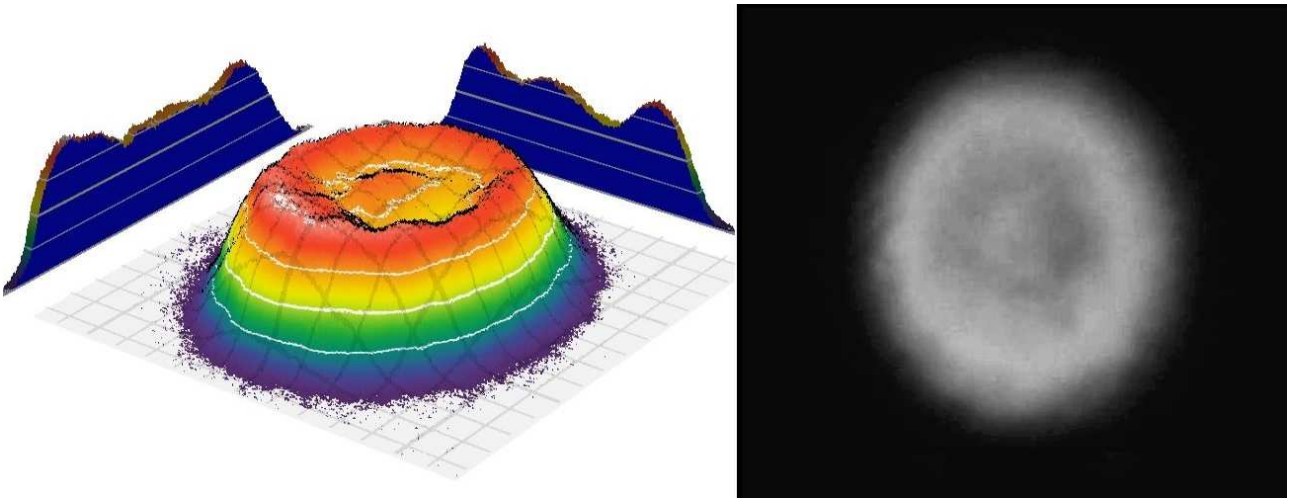

Figure II-20 Profile of the 355 nm beam laser spot modeled with the software IRIS to create a 3D picture (left) from the fluorescence recorded with a camera (right).

The top of the beam profile was processed with the software IRIS to create a 3D picture of the profile (Figure II-19 and Figure II-20, left). At 355 nm, the energy is distributed quite equally over the surface. Provided that the IR beam probed the volume irradiated by the portion of the UV beam displayed in red / orange on Figure II-20, the fluence could be averaged using equation (II-26) At 266 nm Figure II-19, the irregularities of the spot should have prevented the fluence to be determined as an average. We showed nevertheless that the average was close to the effective fluence measured using acetyl bromide as an actinometer (see paragraph II.8.2 page 61).

The energy of the pulse was measured regularly with a power meter (Ophir An/2 power range 0.1-300±0.1 W). The power meter is composed by a thermopile detector having a central metallic disc surrounded by thermocouples. When the laser beam hits the central area of the sensor disc, the

absorbed photons are converted to thermal energy and heat is transferred to the cooled periphery passing through the thermocouples. The current generated by the thermocouples is converted into optical power. The sampling head of the power meter was placed routinely for practical reasons at the exit of the laser. The laser energy was measured after each experiment to ensure its stability during the whole series of experiment. In our case, the fluence measured at the exit of the laser varied between 5×10^{16} and 1.4×10^{17} photons cm^{-2}.

The calibration of the power meter was verified by comparison with another power meter, available at the laboratory that had been previously calibrated. We carried out several measurements with both power meters at different energies. At a repetition rate of 10 Hz, the laser power was varied in a range 0.1-0.8 W modifying the parameter of the YAG laser called “time delay” of the Q-switch. The results obtain with the power meter used in this work have been plotted versus the results of the calibrated one. As can be seen in Figure II-21 the results obtained with our power meter are in very good agreement with the results obtained with the calibrated one. Small variations were found in the results at lower energy because of the difficulty in the stabilization of the energy with variation of the Q switch delay. A slope of 0.99 was derived, which showed that we could rely on the measurements of the power meter currently used in this work.

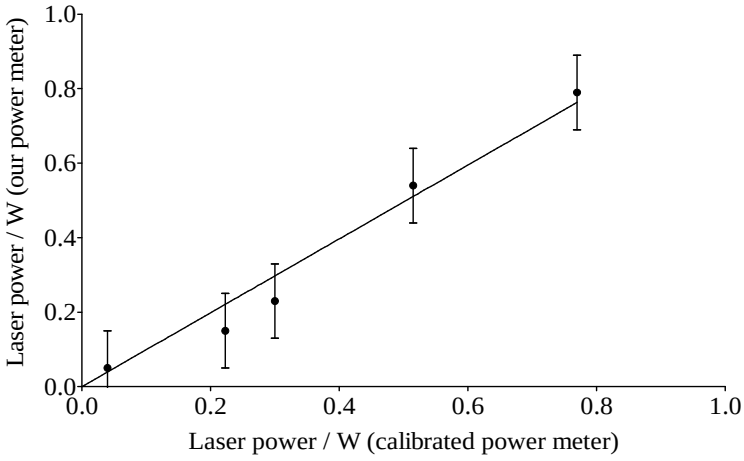

Figure II-21 Plot of the power measured with the power meter currently used in our work against the power measured with a calibrated power meter. The result of the linear regression is Y = 0.9914 X.

II.8.2 Measurement of the fluence with the CH_3COBr photolysis

The fluence at 266 nm was also measured by using a well-characterized photolysis process. In this work the photolysis of CH_3COBr has been chosen as actinometer. The choice of this molecule has been motivated by the following reasons:

- The CO quantum yield is known to be close to the unity $\Phi_{266\ nm} = 0.92 \pm 0.1$ and is not pressure dependent (Khamaganov, Karunanandan et al. 2007).
- CH_3COBr presents a strong absorption at 254 nm and 266 nm: $\sigma_{254} = 2.42\times10^{-19}$ cm^2 $\sigma_{266} = 1.96\times10^{-19}$ cm^2 (Khamaganov, Karunanandan et al. 2007), which allowed to measure the concentrations of CH_3COBr *in situ* using UV spectroscopy at 254 nm, and to get a high S/N ratio during the record of CO profiles.
- CO is expected to be produced almost instantaneously by decomposition of CH_3CO (II-28) with no secondary chemistry leading to CO.

$$CH_3COBr + h\nu \rightarrow CH_3 + CO + Br \qquad \text{II-28}$$

The fluence has been measured from the photolysis of acetyl bromide. The concentrations of CH_3COBr were measured in situ via UV absorption at 254 nm using a line equipped by a Hg lamp, a monochromator, a photomultiplier (Figure II-22) connected to an analog voltmeter with an input resistance of 100 MΩ. The flow of CH_3COBr was regulated through a needle valve. We waited for the concentration of CH_3COBr to be stable before starting the photolysis. Due to the high S/N ratio of the signal, only 10 traces needed to be averaged. The concentration was measured again after each record, to be sure that it had not changed during the records of CO time-profiles (Figure II-23).

Dissociation of the acetyl bromide inside the cell due to the Hg-lamp was neglected. The concentrations obtained from the UV signals were calculated using Lambert Beer law (Table II-4).

Trasmission %	92.5	86.5	78	75
$[CH_3COBr]/\ 10^{15}$ molec cm^{-3}	2.94	5.47	9.36	10.80

Table II-4 Determination of [CH_3COBr] from the absorption at 254 nm.

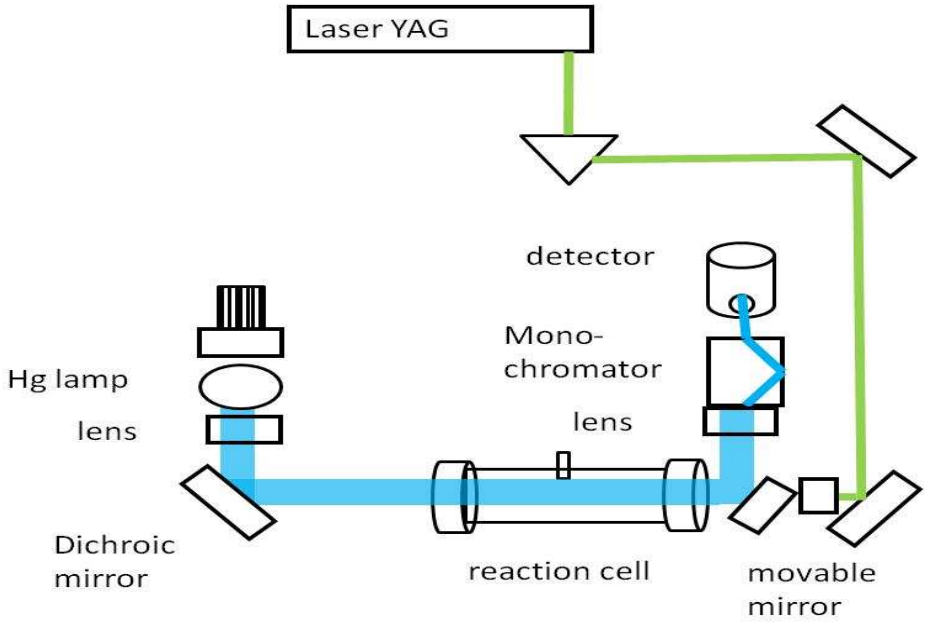

Figure II-22 UV line mounted for the 254 nm detection. The beam stopper was placed between the dichroic mirror and a plane silver mirror which reflected the 254 nm beam to a photomultiplier.

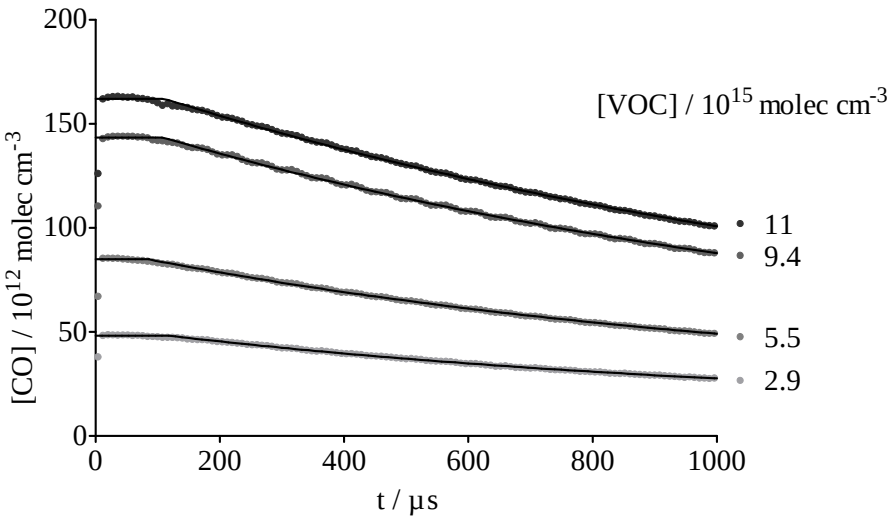

Figure II-23 [CO] signals from CH_3COBr photolysis at 266 nm for four different acetyl bromide concentrations between $[CH_3COBr] = 2.9$ and 10.8×10^{15} molec cm^{-3} at 28 Torr He, photolysis repetition rate has been 5 Hz.

CO concentrations obtained from these experiments were plotted versus the acetyl bromide concentrations multiplied by the absorption cross section at 266 nm and the nominal quantum yield (Φ= 0.92 ± 0.1 (Khamaganov, Karunanandan et al. 2007)).

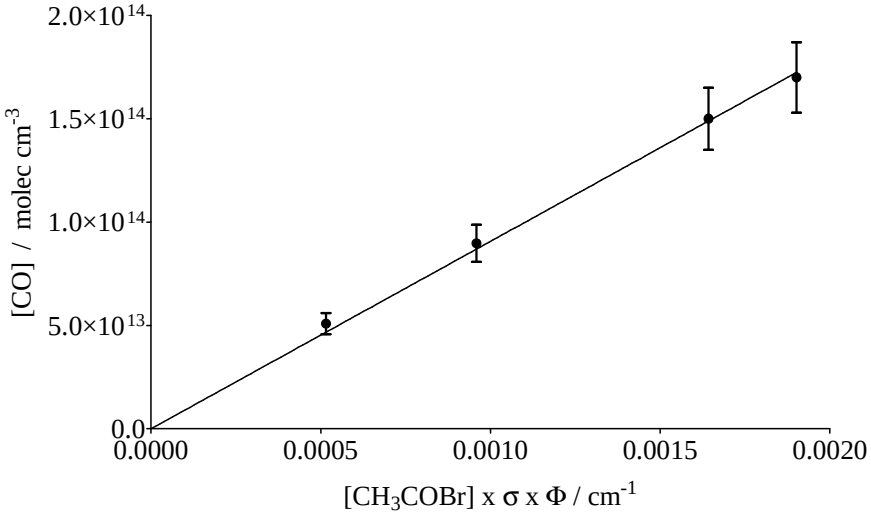

Figure II-24 Variation of [CO] obtained after the photolysis as function of photolyzed [CH_3COBr]. The [CH_3COBr] has been measured with a Hg lamp at 254nm. The result of the linear regression is $Y = 9.07\times10^{16} X$.

Linear correlation is found (Figure II-24), the slope being the fluence F = 9.07×10^{16} photons cm^{-2}. The fluence determined from measurements with the power meter resulted in F = 9.30×10^{16} photons cm^{-2}. There is a good agreement between both values, and we decided to rely on the power meter to derive the fluence to be used for the evaluation of our experiments.

III. Photolysis of acetone (CH_3COCH_3) at 266 nm

Acetone is the simplest ketone and has been the subject of numerous studies detailed in the following. In this chapter we present our results on the photolysis of acetone at 266 nm at room temperature at a pressure of 30 Torr. These results were also used as reference for the photolysis of hydroxyacetone.

III.1 Previous studies

Acetone is an abundant and ubiquitous VOC in the troposphere. Airborne field campaigns have shown its presence over the tropical pacific oceans while the principal sources are mostly located in the Northern hemisphere (Singh, Chen et al. 2001).

Seen that the different sinks of acetone depend on altitude they can have different implications on the tropospheric chemistry. In particular, its reaction with OH radicals is dominant at lower altitudes while photolysis becomes more important at higher altitude because of increasing intensity of radiation in the wavelength range 290-320 nm with increasing heights together with a decrease of the rate constant of the OH reaction with decreasing temperature.

Previous studies explain how, at higher altitudes, the photolysis of one molecule of acetone could be an efficient source of HO_2 radical production than OH initiated reactions (Arnold 2004). This occurs mainly because the HO_2 produced by the photolysis can react with NO to give OH that will be then available for a reaction with a second molecule of acetone. In addition, photolysis of acetone in the Upper Troposphere (UT) is known to be an important source of peroxyacetylnitrate (PAN) which can be transported on a large scale distance (Atkinson and Arey 2003). The kinetics of the reaction of acetone with OH was studied by several authors (see table 2 in ref (Wollenhaupt, Carl et al. 2000)), but the most interesting study at temperatures relevant to the atmosphere was given by Wollenhaupt et al. in 2000 (Wollenhaupt, Carl et al. 2000). They investigated the reaction in the temperature range 202 - 395 K at a pressure of 20 Torr, using pulsed laser photolysis of suitable precursors to generate OH radicals and resonance fluorescence or pulsed laser-induced fluorescence to monitor the OH time profiles. They found that the rate constant of the reaction of OH with acetone could not be described by a simple Arrhenius expression, but rather by a two-exponential function $k_{OH} = 8.8 \times 10^{-12} e^{-\frac{1320}{T}} + 1.7 \times 10^{-14} e^{\frac{423}{T}}$. The rate constant decreases slightly between 202 and 295 K, the values being respectively 1.50×10^{-13} and 1.35×10^{-13} cm^3 s^{-1}, and increases from 240 to 395 K. This behaviour was attributed to a change of mechanism, which could be an electrophilic addition of OH to the carbonyl C-atom followed by formation of acetic

acid and methyl radicals at low temperatures, while hydrogen abstraction is expected to occur at higher temperatures. Arnold and Chipperfield (Arnold 2004) completed the model studying the OH reaction on acetone at different latitudes, distinguishing two areas of interest: tropical areas and mid-latitude areas. They determined the OH rate constants and attributed to acetone a lifetime of 9 days at the tropics and 74 days at the mid latitudes.

The photoexcitation of acetone from the ground electronic state (S_0) to its first electronically excited state (S_1) has been intensively studied. This electronic transition in acetone results in a low and wide absorption band from 220 to 330 nm (Figure III-1) with its maximum around 280 nm, corresponding to a perpendicular transition from the n orbital of the oxygen atom to the π^* orbital of the carbonyl group (Blitz, Heard et al. 2006). The UV spectrum of acetone was measured by several authors but the IUPAC recommendation is based on the data of Gierczak et al. (Gierczak, Burkholder et al. 1998). Around the maximum of absorption at ≈ 280 nm, Gierczak's values are slightly lower than those given by other groups (Wollenhaupt, Carl et al. 2000). At 266 nm, the values of all studies are in agreement and the cross section, at 298 K, is estimated to be $\sigma_{266} = 2.98\times10^{-20}$ cm^2.

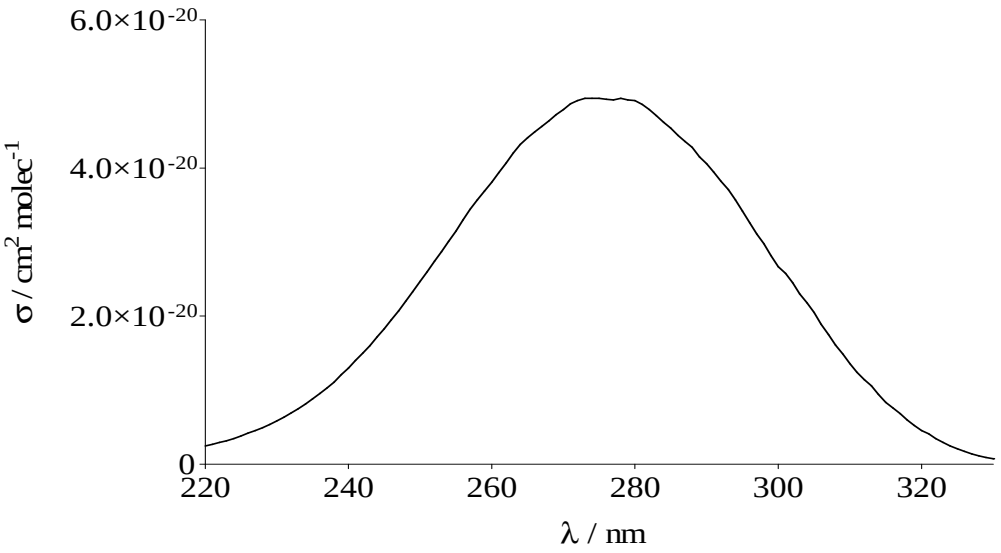

Figure III-1 UV absorption cross section for acetone at 298 K (Gierczak, Burkholder et al. 1998).

The photodissociation of acetone was studied by several groups as early as 1926 (Bowen and Watts 1926). The first investigations on the photodissociation mechanism were performed by Norrish in a series of papers published in the 1930's (Crone and Norrish 1933; Norrish 1934; Norrish, Crone et al. 1934). At 193 nm, acetone dissociates into two methyl radicals and carbon monoxide. Whatever the wavelength is, the first process is an α-cleavage of one C-C bond leading to one methyl radical

CH_3 and to one acetyl radical CH_3CO. The question whether the acetyl radical is able to dissociate into CH_3 and CO has been addressed by most of the studies. The previous quantum yield determinations are discussed in details in (Rajakumar, Gierczak et al. 2008) and are summarized in Table III-1.

Acetone is expected to dissociate according to two main pathways (Rajakumar, Gierczak et al. 2008):

$$CH_3COCH_3 + h\nu \rightarrow CH_3CO + CH_3 \ (\lambda < 338 \text{ nm}) \qquad \text{III-1}$$

$$CH_3COCH_3 + h\nu \rightarrow 2CH_3 + CO \ (\lambda < 299 \text{ nm}) \qquad \text{III-2}$$

CH_3CO formed in reaction III-1 after absorption of a photon can possesss sufficient energy (CH_3CO^*) to dissociate into CH_3 and CO (III-3) or can be stabilized by collision (III-4).

$$CH_3CO^* \rightarrow CH_3 + CO \qquad \text{III-3}$$

$$CH_3CO^* + M \rightarrow CH_3CO + M \qquad \text{III-4}$$

In previous studies it has been shown that the lifetime of the activate CH_3CO^* radicals is lower than 100 ns (Somnitz, Fida et al. 2005; Rajakumar, Gierczak et al. 2008). On our time scale (ms) this reaction time can be considered immediate and as a consequence the dissociation reaction III-3 cannot be distinguished from reaction III-2 with our experimental set-up.

The quantum yield of reaction III-1 could be determined through monitoring CH_3 and / or CH_3CO. Khamaganov et al. (Khamaganov, Karunanandan et al. 2007) studied the photolysis of acetone at 248 and 266 nm monitoring the formation of methyl radicals by LIF at 216.4 nm. At 248 nm, they found that the quantum yield decreased with increasing pressure, starting from 1.4 at zero pressure and converging to 1 at twice the atmospheric pressure. This behaviour could be explained by hot acetyl radicals being stabilized by collisions with the bath gas at elevated pressure but dissociated to yield CH_3 at low pressures. In an experiment performed in a molecular beam in He, North et al. found that 30% of the acetyl radicals had enough energy to dissociate (North, Blank et al. 1995), while Khamaganov found 42%. Somnitz et al. (Somnitz, Fida et al. 2005) studied the same reaction using quantitative infrared diode laser spectroscopy of CO. At low pressures (up to 100 Torr), the results of both studies are in good agreement but differs at more elevated pressures. In 2009 Somnitz (Somnitz, Ufer et al. 2009) performed other experiments at 248 nm detecting directly CO and CO_2 in the range of pressure 19-675 Torr in different bath gas (He, Kr, Ar, SF_6, N_2, O_2 and N_2/O_2). He found different pressure dependences in the bath gases due to the efficiency of the

colliders. At 75 Torr he obtained a CO quantum yield of 0.49 for N_2, in agreement with Rajakumar who determined the quantum yield from the relation $\Phi_{CO} = 1 - \Phi_{CH3CO} = 1 - 0.53 = 0.47$ at a pressure of 60 Torr (Rajakumar, Gierczak et al. 2008). Khamaganov et al. (Khamaganov, Karunanandan et al. 2009) studied again the photolysis of acetone, monitoring atomic bromine generated by reaction of the photofragments CH_3 and CH_3CO with bromine. They showed that the overall quantum yield was 1 with no dependence on pressure at 248nm, while at 266 nm there was a slight dependence, starting from 0.96 at zero pressure to 0.82 at 760 Torr. This work confirmed their previous study.

Investigations on the mechanism of photodissociation were conducted by Emrich and Warneck (Warneck 2001) in 2001, and more recently by Blitz (Blitz, Heard et al. 2006). They determined the quantum yield of production of the acetyl radical between 266 and 330 nm as a function of pressure and temperature: Emrich converting it to PAN by reaction with O_2 and NO_2, while Blitz partially converted it to OH by reaction with O_2. They analyzed their experimental data by a Stern-Volmer graph: Blitz showed that there was a dependence on both, wavelength and pressure on the dissociating states S_1 and T_1. At a pressure higher than 25 Torr, the state T_1 is readily quenched (reaction III-11), and dissociation occurs from the S_1 state whatever the wavelength. They were able to determine that the intersystem crossing between (S1) and (T1) (reaction III-9) was more efficient above 320 nm, and almost zero below 295 nm. From an Arrhenius analysis of the temperature dependence of the photodissociation, barriers of dissociation respectively on the S_1 and T_1 states were located at respectively 300 and 306 nm, *i.e.* 34 kJ mol^{-1} and 56 kJ mol^{-1} above the S_1 and T_1 states (Figure III-2). Below 25 Torr, dissociation occurs exclusively from the S_1 state at wavelengths shorter than 300 nm, and from the S_1 and T_1 states above 300 nm. In a recent paper, Szilágyi et al. (Szilágyi, Kovács et al. 2009) found also a curvature in their Stern-Volmer analysis performed at 308 nm in different gases.

Blitz et al. found that the yield of CH_3CO at 248 nm was lower than yields at longer wavelengths, which was due to the competitive way of dissociation leading to methyl radicals and carbon monoxide. They derived a yield for CO of 0.63 at 248 nm and 0.37 at 266 nm. The temperature dependence on the yield of CO is due to the dissociation of the acetyl radical which needs at least 71 kJ mol^{-1}. This energy comes from both, the internal excitation of the acetyl radical after the photodissociation, and from the ambient thermal energy. Blitz et al. tested the following mechanism available above 300 nm (reactions III-5 to III-11 and Figure III-2) :

$$CH_3COCH_3\ (S_0) + h\nu \rightarrow CH_3COCH_3\ (S_1, S_1^*) \qquad \text{III-5}$$

$$(S_1) \rightarrow CH_3CO + CH_3 \qquad \text{III-6}$$

$$(S_1^*) \rightarrow 2\ CH_3 + CO \qquad \text{III-7}$$

$$S_1 + M \rightarrow S_0 + M \qquad \text{III-8}$$

$$(S_1) \rightarrow (T_1) \qquad \text{III-9}$$

$$(T_1) \rightarrow CH_3CO + CH_3 \qquad \text{III-10}$$

$$(T_1) + M \rightarrow S_0 + M \qquad \text{III-11}$$

Below 300 nm, only the four first reactions (III-5) to (III-8) are to be considered, *i.e.* there is not ISC from (S_1) to (T_1).

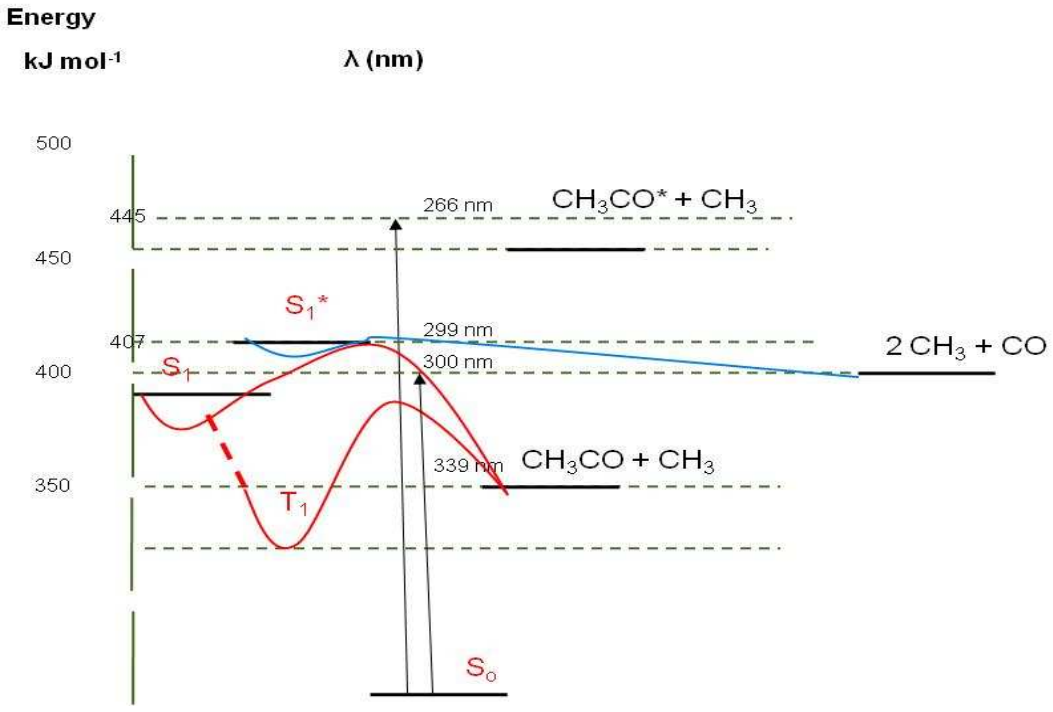

Figure III-2 Schematic of the energy diagram for acetone photolysis (adapted from (Blitz, Heard et al. 2006) and (Somnitz, Fida et al. 2005)).

Authors	Experimental conditions	λ / nm	Φ_{CH3CO}	Φ_{CO}	Φ_{CH3}	Φ_{tot}
(Meyrahn, Pauly et al. 1986)	250 to 300 nm - 760 Torr – Bath gas : air. CH_3CO converted to PAN by addition of NO_2 PAN, CO, CO_2 quantified by GC	250 260 270	0.76 0.80 0.64	0.45 0.18 0.10	- - -	- - -
(Gierczak, Burkholder et al. 1998)	248 to 337 nm – 100 to 760 Torr – Synthetic air Loss of acetone measured by GC	248 266	- -	- -	- -	1.10 0.94
(Khamaganov, Karunanandan et al. 2007)	248 and 266 nm – 298 K – 5 to 1500 Torr of N_2 CH_3 and CH_3CO monitored by LIF	248 266			1.42 to 1.0 0.93	
(Khamaganov, Karunanandan et al. 2009)	248 and 266 nm – 60 to 760 Torr of N_2 Reaction of CH_3 and CH_3CO with Br_2 to yield Br atoms detected by time-resolved resonance fluorescence 248 nm : 224, 234 and 298 K 266 nm : 298 K	248 266				0.98 0.96 to 0. 82
(Blitz, Heard et al. 2006)	266 to 327.5 nm – 0.3 to 400 Torr of He – 218 to 295 K CH_3CO partially converted to OH by reaction with O_2 OH monitored by LIF	250 265	0.37	0.62 0.37		
(Somnitz, Fida et al. 2005)	248 nm – 298 K – 15 to 675 Torr of N_2 Detection of CO by diode laser absorption spectroscopy	248		0.45 to 0.25		
(Somnitz, Ufer et al. 2009)	248 nm – 298 K – 19 to 675 Torr of (He, Kr, Ar, SF_6, N_2, O_2 and N_2/O_2)	248		N_2 :0.51 to 0.30		

	Detection of CO by diode laser absorption spectroscopy			He :0.54 to 0.37		
(Rajakumar, Gierczak et al. 2008)	248 nm – 296 K – 60 to 670 Torr in N_2 or He CH_3CO detected by CRDS	248	0.60 to 0.82			
(Emrich and Warneck 2000)	280 to 300 nm – 97 to 750 Torr of air Conversion of CH_3CO to PAN by addition of NO_2	280	1.00 to 0.77			
(Szilágyi, Kovács et al. 2009)	308 nm – 10 to 760 Torr of He / Xe / Air / O_2 Loss of acetone measured by GC	308				0.58 to 0.11 (in air).
(Gardner, Wijayaratne et al. 1984)	279 to 313 nm = 272 to 301 Torr – 25 to 745 Torr in air	279 290 299 313		0.015 0.026 0.0211 0.0169		
(Gandini and Hackett 1977)	330-240 nm, pressures (0- 1000 Torr) 21°C. CO monitored by resonance fluorescence	240 250 265 275 305		0.64 0.35 0.19 0.06 0.03		

Table III-1 Previous determinations of quantum yields of photodissociation of acetone. Pressures expressed in mbar in the papers are converted in Torr in this table.

III.2 Experimental details

A mixture of acetone (Sigma Aldrich reagent 99.9% purity) in He or N_2 was prepared in 10 L balloons using a volumetric method. For details regarding the preparation, the reader is referred to paragraph II.5.1 page 39. Typically, ≈ 30 Torr of acetone were introduced in the balloon, which was then completed up to ≈ 1000 Torr with He or N_2. The mixture was flown to the cell through a flow meter which was calibrated taking into account the presence of acetone in the mixture. The flow rates were varied between 2 and 60 ccm min^{-1} STP, while the carrier gas was flown at a rate of 175 to 750 ccm min^{-1} STP. The concentration of acetone was then in the range $0.4 – 1.3\times10^{16}$ molec cm^{-3}. Acetone was photolyzed at 266 nm at room temperature (295 K) and at the average pressure of 30 Torr. Most experiments have been performed in N_2, He as buffer gas has been used only once in order to detect upper vibrational states of CO. In this experiment, performed at 35 Torr, the concentration of acetone was kept fixed at 5.4×10^{16} molec cm^{-3}.

III.3 Photolysis signals

III.3.1 Description of the time-profiles.

The CO concentration time profiles obtained from the acetone photolysis at 266 nm have been fitted to equation III-12, such as already presented in paragraph II.7.4 page 53.

$$[CO] = ([CO]_{direct} + [CO]_{slow} \times (1 - e^{-k' \times t})) \times e^{-k_{diff} \times t} \qquad \text{III-12}$$

In this chapter are presented some typical signals and the calculation on the kinetic parameters. Typical profiles we have obtained at different concentrations of acetone are shown Figure III-3.

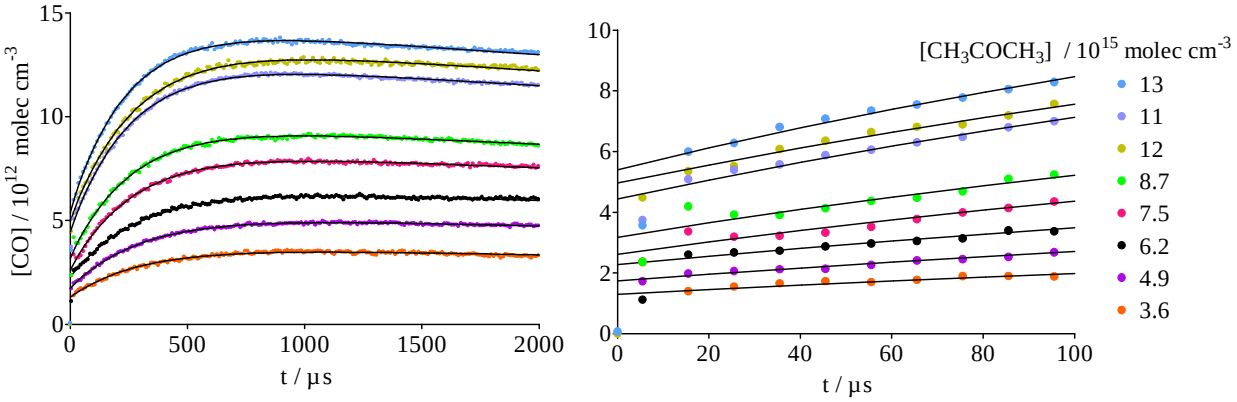

Figure III-3 Time resolved profiles of [CO] after photolysis of different acetone concentrations (reported in legend) at 36 Torr N_2 and a laser energy of 54 mJ at a repetition rate of 5Hz. The right graph shows a zoom on the first 100 µsec.

The presence of the non zero component at the origin, *i.e.* at very short times after the laser pulse, proved the existence of CO formed immediately after the UV photolysis pulse, in the first microseconds (Figure III-3). In this part of the profile we were not able to distinguish any kinetics because the increase was too fast to be time-resolved. In the following, this CO formed just after the laser pulse is called CO_{direct} and is considered to be formed in reaction III-7.

This almost instantaneous formation of CO_{direct} was followed by a slower formation of CO which extended up to ≈ 750 µs (named CO_{slow} in what follows). This component is suspected to originate from the relaxation of CO, formed in reaction III-7 in excited vibrational states, to the ground state CO (v=0).

This hypothesis was confirmed in the current work by the direct detection of CO in upper vibrational states as explained further down in paragraph III.3.4 page 76. In the next paragraph, the rate of formation of CO_{slow} will be analyzed.

III.3.2 Origin of the slow kinetic in the time-profiles of CO

In order to study the origin of CO_{slow}, the time-profiles of [CO] were fitted to equation III-12. From the signals recorded in different experiments we extracted the value of the pseudo first order kinetic constant k and we plotted the results versus the acetone concentration as shown in Figure III-4. Even though the scatter of the data is quite high, a linear dependence can be determined with a slope of $(9.6 \pm 0.7)\times10^{-14}$ cm^3 $molec^{-1}$ s^{-1} that can be interpreted as the rate constant of relaxation of CO(v=1) to CO(v=0) by collision with acetone molecules. No literature value is, to our knowledge, available for this rate constant. However, this value seems reasonable if compared to the literature

value for the relaxation of CO(v=1) with propynal: k = 4.43×10^{-14} cm^3 $molec^{-1}$ s^{-1} (Chowdhury 2003).

In the case of CO profiles recorded in N_2, the CO(v=1) will relax also by collisions with buffer gas molecules (N_2). In Figure III-4 the rate constant of the relaxation by N_2 can be extrapolated from the intercept of the linear regression (Y_0 = 2408 s^{-1}). With [N_2] = 1×10^{18} molec cm^{-3}, this value leads to a rate constant k= 2804 /1×10^{18} = 2.8×10^{-15} cm^3 $molec^{-1}$ s^{-1}. This value can be compared to literature values: Stephenson (Stephenson 1973) indicates the rate constant $k_{CO/N2}$ = 177 s^{-1} $Torr^{-1}$, which can be converted to $k_{CO/N2}$ = 5.1×10^{-15} cm^3 $molecule^{-1}$ s^{-1}. The value found in our work is lower than the literature value, but still in the same order of magnitude.

This difference in the rate constant is probably due to the presence of CO in the upper vibrational excited states, *i.e.* v>1. The relaxation to CO v=0 might be then slowed down by the progressive re-population of CO(v=1) through a relaxation of the upper vibrational states.

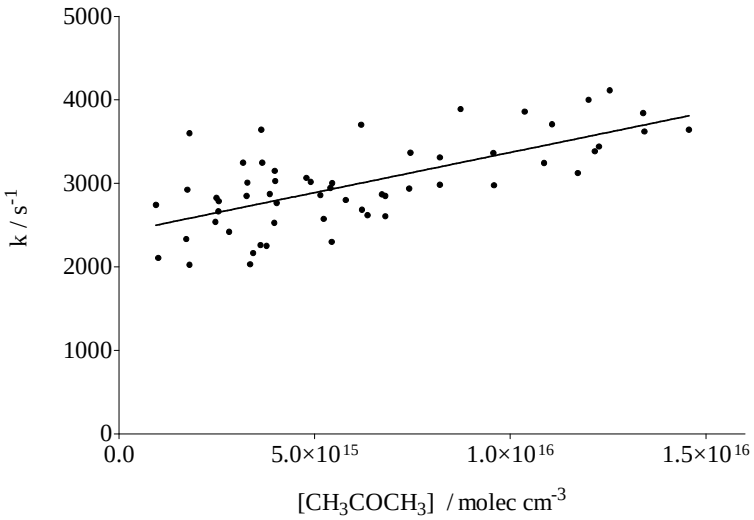

Figure III-4 Pseudo first order kinetic constant plotted versus acetone concentration. The values refer to fits of different experiments. The linear regression results in Y = 9.62×10^{-14} X + 2408.

In order to clarify the nature of the component CO_{slow} we decided to neglect the presence of a reaction radical-radical originating CO. To prove that CO_{slow} is not formed by secondary reactions R+R we normalized the profiles of Figure III-3 according to $[CO]_{direct}$ (Figure III-5 left). After normalization, all signals start at the same point and grow with at different rates forming the same amount of CO_{slow}.

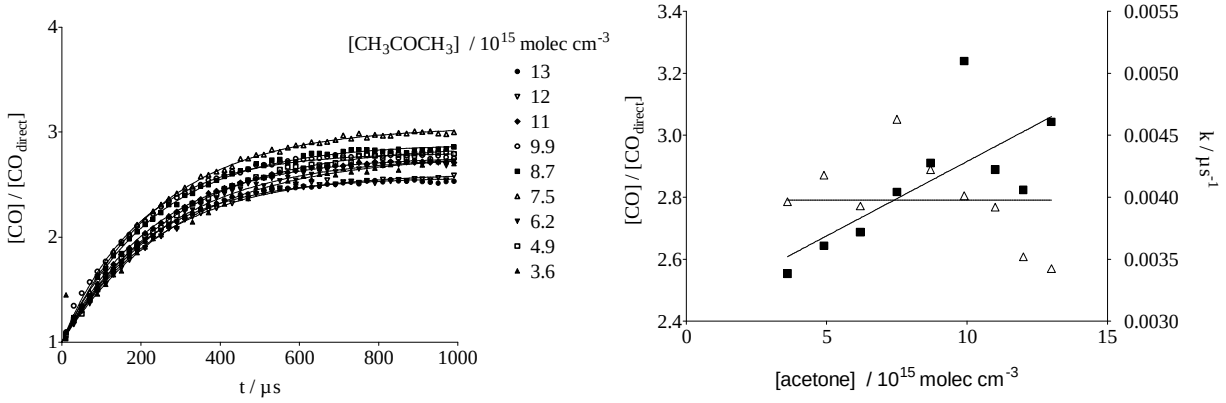

Figure III-5 Left: CO profiles of Figure III-3 normalized respect to the CO_{direct}. Right: Dependence between the k (■), CO_{slow} (Δ) and the [acetone] introduced in the cell.

The results of the fit for the normalized signals are displayed in Figure III-5 right. It is possible to remark that the values of CO_{slow} are highly scattered around the value 2.8 and the plotted rate constants draw a linear trend (slope = 1.02×10^{-13} cm^3 $molec^{-1}$ s^{-1}) with a non null intercept (Y0 = 3090 s^{-1}). The non null intercept can rationally represent the relaxation CO by N_2 because for [N_2] = 10^{18} molecule cm^{-3} we can determine a rate constant k = 3.5×10^{-15} cm^3 $molec^{-1}$ s^{-1}, slightly lower than the expected 5.1×10^{-15} cm^3 $molec^{-1}$ s^{-1} given by Stephenson (Stephenson 1973) but still of the same order of magnitude. This difference may be due to the relaxation of upper vibrational excited states that, populating CO v=1, lowers the apparent constant. The slope (1.02×10^{-13} cm^3 $molec^{-1}$ s^{-1}) instead can represent the relaxation of CO by acetone. The determined value is in good agreement with what found in Figure III-4 but higher than that found for propynal: k = 4.43×10^{-14} cm^3 $molec^{-1}$ s^{-1} by Chowdhury (Chowdhury 2003). Considering the differences between the two molecules we can consider this value reasonable for the CO relaxation operated by acetone molecules.

III.3.3 Energy balance in the photodissociation of acetone.

At 248 nm, Somnitz et al. estimated the energy threshold for the acetone photodissociation to be 399 kJ mol^{-1} for the direct formation of CO, and 353 kJ mol^{-1} for the dissociation into CH_3 and CH_3CO*. In his work Somnitz determined also the distribution of remaining energy after photodissociation (135 kJ mol^{-1}). He found that 46% (63 kJ mol^{-1}) is kept within CH_3CO*, and 43% (≈58 kJ mol^{-1}) in the relative motion of the photofragments CH_3 and CH_3CO. Only 11 % (14 kJ mol^{-1}) is associated to the CH_3 radical (Somnitz, Fida et al. 2005).

The photolysis of acetone at 248 nm was already studied in 1995 by North (North, Blank et al. 1995). They. found a value in agreement with the value of Somnitz for the average translational energy of the fragments CH_3 and CH_3CO, estimated to be ≈ 60 kJ mol^{-1}.
A 266 nm-photon provides an energy of 448 kJ mol^{-1}. The remaining energy after the absorption of one photon at 266 nm will be 95 kJ mol^{-1}. Considering the same percentage found by Somnitz, CH_3CO will keep 59 kJ mol^{-1}. CO needs ≈ 25 kJ mol^{-1} for each quantum of vibrational excitation. As a result, a 266-nm photon carries enough energy to enable the production of CO in the vibrational state up to v=2. This energy calculation justified the record of the CO profiles performed in Figure III-6 but not for the CO v = 3 that will require 75 kJ mol^{-1}.

III.3.4 Excited states

In order to prove that the CO appearing at longer time kinetic was effectively coming from the excited states we decided to detect and record the CO formed, during photolysis, in the upper vibrational excited states. The detection of these states represented a real challenge in the detection due to the weakness of the line, the low population of these states (v=2 and v=3) and the limitations imposed by our reference cell: pressure achievable and optical path length (paragraph II.6.1 page 43). As a matter of fact, we had to perform the detection of the CO vibrational states v>1 using a different method with respect to the CO v=0.
With our instrumental set-up the excited states absorption lines were selected with the help of an interferometer of Fabry Perot. The interferometer is a Germanium bar, placed at the entrance of the monochromator, capable to introduce regular interferences in the signal of the diode. Knowing the tabulated wavelength of the excited states (Jacquinet-Husson, Scott et al. 2008) and having as reference a fundamental line it was possible to set the detection on the excited one. The operation of stabilization was than performed on the position where the absorption line was supposed to be, but without any possibility of visual verification. The same problem emerged at the moment of the baseline subtraction that was chosen in a zero signal position close to the absorption line.

Signals of CO in the excited vibrational states (v=1,2) have been successfully recorded in He as buffer gas. The signals presented in Figure III-6 have been simulated in order to verify the relaxation constant of the upper vibrational excited states. No adapted model was found to reproduce the kinetics recorded. Firstly, the intensity of the signals could not be reproduced accurately due to the difficulty of the stabilization on the absorption lines and because of the lack of literature on the CO(v>0) absorption cross sections. In any case, to give an idea of the expected

concentration, CO(v=1) and CO(v=2) intensities were multiplied respectively by 2 and 3 (see paragraph II.7.3 page 49). Secondly, the kinetics cannot be related with the vibrational relaxation because of irregularities generated by the baseline subtraction.

Still we can obtain information from the shape:
CO(v=1) signal corresponds in shape and structure to the CO(v=0). A rapid rise immediately after the photolysis pulse is followed by an exponential kinetic. This form will be expected in presence of a relaxing CO(v=2) vibrational state.
CO(v=2) profile instead shows the presence of a non zero component at t=0 followed by a fast relaxation. For this vibrational state it was impossible to identify a secondary formation. It is then possible to deduce that the CO(v=3) relaxation occurs too fast to be detected or that CO is not formed in the vibrational state v=3.

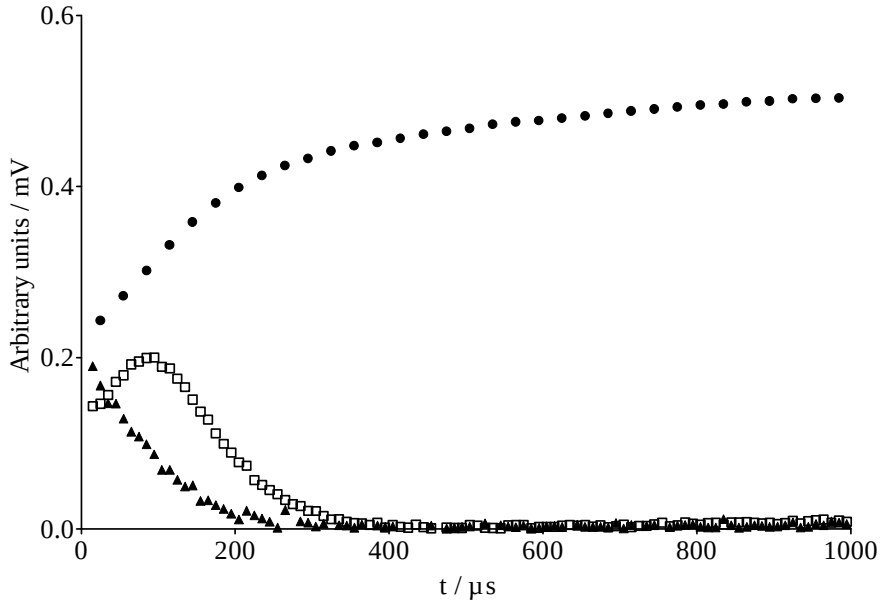

Figure III-6Excited states recorded in He for a concentration of [CH_3COCH_3] = 5.4×10^{16} molec cm^{-3}. CO(v=0) profile (•), CO(v=1) profile (□) CO(v=2) profile (▲). The photolysis was performed at 30 Torr and the laser energy was 94 mJ for a repetition rate of 5Hz.

III.4 Quantum yield results

The CO formed in the acetone photolysis, as described by equation III-13, depends on the wavelength of the radiation, on the laser fluence and on the quantum yield parameter (Φ).

$$[CO] = \Phi_{CO} \times \{[CH_3COCH_3] \times F_{266} \times \sigma_{266}\} \qquad \text{III-13}$$

The quantum yield of the photolysis process can be determined from the plot (Figure III-7) of the measured CO concentrations versus ($[CH_3COCH_3] \times F_{266} \times \sigma_{266}$) as the slope of the linear regression. The good linearity is confirmed by the correlation coefficient greater than 0.95 for both curves.

The CO_{direct} (originated from reaction III-7) has a lower slope, consequently a lower quantum yield $\Phi_{CO\ direct} = 0.11 \pm 0.02$. On the other hand, the CO_{slow} formed at longer reaction time (from the relaxation of the excited states of CO), has a quantum yield defined by $\Phi_{CO\ slow} = 0.29 \pm 0.04$. For CO, the total quantum yield value ($\Phi_{CO\ tot}$) determined for the acetone photolysis at 266 nm can be estimated as the sum of the two components:

$$\Phi_{COtot} = \Phi_{COdirect} + \Phi_{COslow} \qquad \text{III-14}$$

The result of equation III-14 is $\Phi_{CO\ tot} = 0.40 \pm 0.04$.

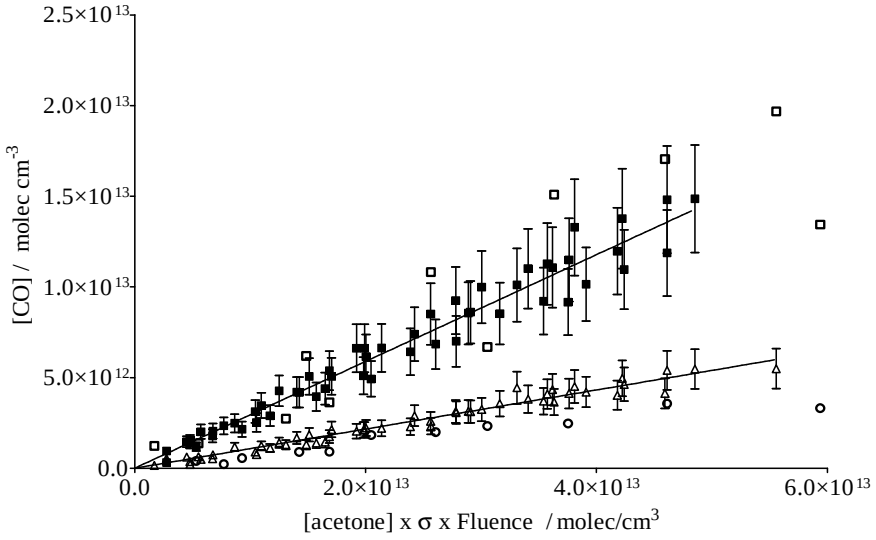

Figure III-7 Linear relation occurring between the different components of CO formed from the relaxation of the upper vibrational excited states (■) and CO from reaction III-7 (Δ) and the acetone concentrations introduced multiplied by the absorption cross section and the fluence. Clear squares and clear dots represent the outliers. The results of the linear regressions Y = a X are respectively: – a =.0.1079 for the triangles and – a =.0.2944 for the dark squares.

III.5 Acetone conclusions

It has been proved the presence of CO formed immediately after the photolysis pulse, confirming the mechanism proposed in literature (Blitz, Heard et al. 2006; Rajakumar, Gierczak et al. 2008). It has been proved also the existence of another pathway of CO formation at longer reaction time. The estimated quantum yields for these two pathways of CO formation are respectively $\Phi_{CO\ direct}$ =0.11±0.02 and $\Phi_{CO\ slow}$ = 0.29 ± 0.04. This CO_{slow} represents the relaxation to the v=0 state from of CO in the upper vibrational excited states (CO v=1 and CO v=2) that have been directly detected and recorded on a 1 ms time scale. The total quantum yield value of CO determined for the acetone photolysis at 266 nm is estimated to be $\Phi_{CO\ tot}$ =0.40±0.04 in good agreement with the values of Somnitz and Khamaganov (Somnitz, Fida et al. 2005; Khamaganov, Karunanandan et al. 2007).

IV. Photolysis of hydroxyacetone (CH_3COCH_2OH) at 266 nm.

IV.1 Introduction

Hydroxyacetone (HAC) is formed in the atmosphere as a secondary product of the OH-initiated oxidation of isoprene. HAC can be removed by reaction with OH or photolysis.

Dillon et al. extensively studied the reaction of OH with hydroxyacetone in the temperature range 233 – 263 K at a pressure of 60 Torr in N_2 or He in different conditions (Dillon, Horowitz et al. 2006). The kinetics was followed by measuring time profiles of [OH] using PLIF. OH radicals were generated using three different methods. The photolysis of HONO generated *in situ* was performed at 351 nm where HAC was not photolyzed. In this method, $O(^3P)$ was also produced from traces of NO_2, which resulted in undesired chemistry taken into account in the analysis. The photolysis of H_2O_2 at 248 nm was found not to be suitable because the slow formation of OH produced by photofragments perturbed the kinetic. The last method was the photolysis of O_3 at 248 nm in the presence of CH_4. The large cross section of O_3 at this wavelength made it possible to use low fluences, and hence to neglect the photolysis of HAC. This method was particularly adapted for studies at low temperatures. The results showed that the rate constant could be described by the following Arrhenius expression (II-1) indicating that the kinetics is faster and faster as temperature decreases.

$$k_{HAC+OH} = (2.15 \pm 0.3) \times 10^{-12} e^{\frac{305 \pm 10}{T}} \qquad \text{IV-1}$$

Baasandorj et al. (Baasandorj, Griffith et al. 2009) recently remeasured the temperature dependence of the reaction HAC + OH and derived the following Arrhenius expression (eq. IV-2) which is in complete contradiction with Dillon's result :

$$k_{HAC+OH} = (1.88 \pm 0.75) \times 10^{-12} e^{\frac{-(545 \pm 60)}{T}} \qquad \text{IV-2}$$

At 298 K, the above expression (eq. II-1) gives a value of $k_{HAC+OH}(298\ K) = (5.98 \pm 0.5) \times 10^{-12}$ cm^3 s^{-1}, while (eq. IV-2) gives $k_{HAC+OH}(298\ K) = (3.02 \pm 0.28) \times 10^{-12}$ cm^3 s^{-1}. This latter rate constant is in agreement with values obtained by other groups : Orlando et al. in 1999 used a relative method and found $(2.5 \pm 0.6) \times 10^{-12}$ cm^3 s^{-1} with respect to $k_{(CH3OH + OH)}$ and $(3.5 \pm 0.7) \times 10^{-12}$ cm^3 s^{-1} with respect to $k_{(C2H5OH + OH)}$ (Orlando, Tyndall et al. 1999); Dagaut et al. in 1989 found $(3.0 \pm 0.3) \times 10^{-12}$ cm^3 s^{-1} (Dagaut, Liu et al. 1989) and Chowdhury found in 2002 $(2.8 \pm 0.2) \times 10^{-12}$ cm^3 s^{-1} (Chowdhury, Upadhyaya et al. 2002). Dillon measured his concentrations of HAC by UV spectroscopy at 184.9 nm, using its own value $\sigma_{184.9} = (5.43 \pm 0.08) \times 10^{-18}$ cm^2 $molecule^{-1}$, which

was confirmed by Baasandorj in 2009. He said that the discrepancy between its value and the others might come from erroneous measurements of [HAC] performed by volumetric methods. The lifetime of HAC with respect to removal by OH is then unclear, ranging from 2 to 4 days in the upper troposphere. Photolysis of HAC may be predominant over removal by OH.

The photoexcitation of HAC from the ground electronic state (S_0) to its first electronically excited state (S_1) results in a low and wide absorption band from 220 to 300 nm with its maximum at 266 nm. The absorption maximum of HAC is slightly higher than that of acetone and is blue-shifted approximately by 15 – 20 nm. The UV spectrum of HAC was first measured by Orlando et al. in 1999 (Orlando, Tyndall et al. 1999). In 2006, Butovskaya et al. (Butokovskaya, Pouvsesle et al. 2006) measured again the spectrum and they found that the values of Orlando were overestimated by more than 20% near the maximum of absorption at 266 nm : $\sigma_{266(Orlando)} = 6.74\times10^{-20}$ cm^2 and $\sigma_{266(Butkovskaya)} = 5.43\times10^{-20}$ cm^2. The absorption profiles of Orlando and Butkovskaya are presented in Figure IV-1.

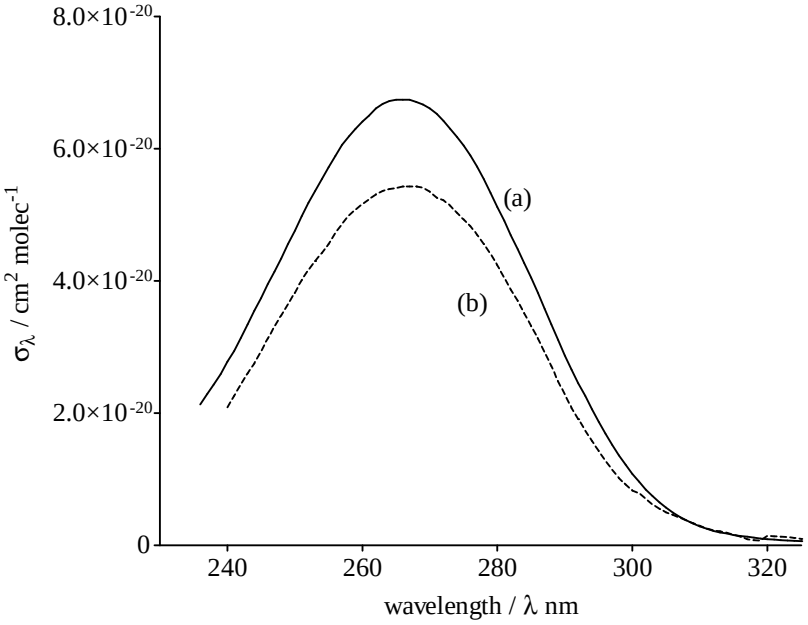

Figure IV-1 UV absorption cross section of hydroxyacetone at 298 K according to (a) (Orlando, Tyndall et al. 1999) (b) (Butokovskaya, Pouvsesle et al. 2006).

Data about the energies required to break bonds in HAC were given by Chowdhury et al. (Chowdhury, Upadhyaya et al. 2002). The primary dissociation is likely to occur through C-C bond rupture (eq. IV-3 and IV-4). The wavelength thresholds were determined from the enthalpies of dissociation given in figure IV.2.

$$CH_3COCH_2OH + h\nu \rightarrow COCH_2OH + CH_3 \quad \text{IV-3}$$

$$CH_3COCH_2OH + h\nu \rightarrow CH_3CO + CH_2OH \quad \text{IV-4}$$

$$CH_3COCH_2OH + h\nu \rightarrow CH_3COCH_2 + OH \quad \text{IV-5}$$

CH_3CO formed in reaction IV-4 after absorption of a photon can possess sufficient energy (CH_3CO^*) to dissociate into CH_3 and CO (III-3) or be stabilized by collision (III-4).

$$CH_3CO^* \rightarrow CH_3 + CO \quad \text{IV-6}$$

$$CH_3CO^* + M \rightarrow CH_3CO + M \quad \text{IV-7}$$

In previous studies it has been shown that the lifetime of the activate CH_3CO^* radicals is lower than 100 ns (Somnitz, Fida et al. 2005; Rajakumar, Gierczak et al. 2008). On our time scale (ms) this reaction time can be considered immediate and as a consequence the dissociation reaction III-3 cannot be distinguished from reaction IV-9 with our experimental set-up.

$$CH_3COCH_2OH + h\nu \rightarrow CH_3 + CO + CH_2OH \quad \text{IV-8}$$

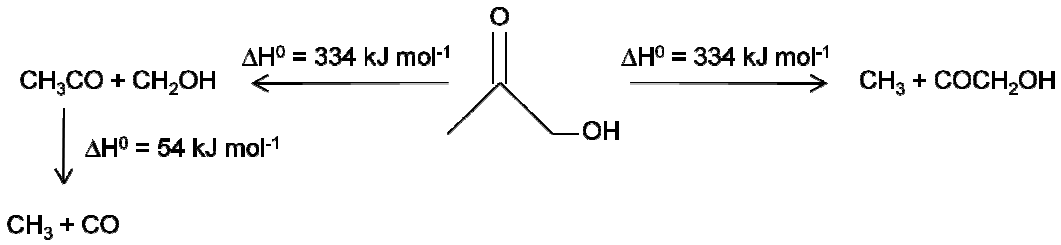

Figure IV-2 Energies required for bond breaking in HAC.

The radical $COCH_2OH$ formed in reaction (IV-3) may decompose according to (eq. IV-9) :

$$COCH_2OH \rightarrow COCH_2 + OH \ (\Delta H^0 = 151 \text{ kJ mol}^{-1}) \quad \text{IV-9}$$

The first study of the photolysis of HAC was given by Orlando et al. in 1999 (Orlando, Tyndall et al. 1999). A mixture of HAC in air in a 47 L stainless-steel chamber was illuminated with a Xe-arc lamp equipped with two different filters, enabling the photolysis to occur in the 240 – 420 nm range or at wavelengths higher than 290 nm. Fluence was measured using the photolysis of Cl_2 as an actinometer. After 5 to 1000 s of irradiation, the mixture was analysed by FTIR spectroscopy. They determined the photolysis rate of HAC relative to that of chlorine and they derived the overall quantum yield of photolysis $\Phi = 0.65 \pm 0.25$ in the 240 – 420 nm range. For wavelengths longer

than 290 nm, the absorption of HAC is low and measurements were subjected to too many uncertainties due to extremely slow photolysis rates.

The analysis of the products formed in the course of the photolysis showed that formaldehyde H_2CO, carbon monoxide CO and carbon dioxide CO_2 were the main products. These compounds are signatures of a photolysis occurring through a C-C bond scission (Norrish type I mechanism, eq. IV-3 and IV-4).

Reactions IV-3 and IV-4 were justified also by theoretical studies made by Wu (*ab initio* calculations) and measurements by Chowdhury (LP-LIF). They proved that the C-C bond breaking in the α position of the kenotic group led to two reactions with equal energetic probabilities (Chowdhury, Upadhyaya et al. 2002; Wu, Xie et al. 2003).

In the following, we present our results on the photolysis of hydroxyacetone at 266 nm. The rates of formation of CO and CH_2O were investigated.

IV.2 Experimental details.

Hydroxyacetone was purchased from Aldrich (technical grade, 90%) and used without further purification. It has a high boiling point (145 °C) and a low vapor pressure at room temperature (4 Torr). A recent publication by Petitjean et al. (Petitjean, Reyès-Pérez et al. 2010) on the measurement of the vapor pressure of hydroxyacetone gives a value of 20.7 Torr at 323 K. Our own measurement (see Annex B.4 page 148) made at 323 K gave a value of 21 mbar, in fair agreement with the published value. Hydroxyacetone was then flown to the cell using a pre-warmed carrier gas (He or N_2) bubbling in the liquid (see paragraph II.5.2 page 41). The temperature of the bubbler was set at 323 K. For the experiments performed in N_2 the flow of the carrier gas was controlled by a mass flow meter and was set to achieve concentrations in the range 3.15×10^{15} – 1.06×10^{16} molec cm^{-3}. The pressure inside the bubbler was in the range of 400 to 800 mbar and was manually controlled by throttling a needle valve placed at the exit of the bubbler. The cell and the windows, the valves and all the tubes were heated at 60°C in order to prevent hydroxyacetone to condense on the walls. The working pressure was set at 26 Torr. The experiment performed in He was focused on the detection of CO vibrational state. In this case the concentration of hydroxyacetone was fixed at 1.2×10^{16} molec cm^{-3} for 28 Torr and the cell warmed at 60°C.

The photolysis of hydroxyacetone was performed at 266 nm and the repetition rate was set at 5 Hz. The expected photoproducts at this wavelength are the hydroxymethyl radical CH_2OH and the acetyl radical CH_3CO. CH_2OH was readily converted into formaldehyde CH_2O by reaction with O_2

introduced in a large excess. At a typical concentration of O_2 of 10^{16} molec cm^{-3}, the total conversion of CH_2OH into CH_2O took place in less than 100 μs.

IV.3 Time resolved signals of CO in the photolysis of hydroxyacetone at 266 nm.

The time profiles of [CO] obtained after photolysis of HAC are shown in Figure IV-3. They are composed of a fast increase of [CO] occurring in the first μs after the laser pulse, followed by a slower formation of CO. The last part of the profile is due to diffusion of CO out of the photolysis beam cylinder. The experimental traces were fitted to equation IV-10:

$$[CO] = ([CO]_{direct} + [CO]_{slow} \times (1 - e^{-k' \times t})) \times e^{-k_{diff} \times t} \qquad \text{IV-10}$$

The presence of the non-zero component at the origin (after the laser pulse) proved the existence of CO formed immediately after the UV photolysis pulse, in the first microseconds (Figure IV-3). In this part of the profile we could not distinguish any kinetics because the increase was too fast to be resolved. This CO formed just after the laser pulse is called CO_{direct} and is considered to be originated by reaction III-3.

This almost instantaneous formation of CO_{direct} was followed by a slower formation of CO which extended to ≈ 750 μs. This component is suspected to be originated CO formed by reaction III-3 and present in the excited vibrational states which relax to populate the fundamental one.

This hypothesis was confirmed in the current work by the record of the CO upper vibrational states produced in the hydroxyacetone photolysis (paragraph IV.4 page 91). It can be also proved initially with the study of the pseudo first kinetic rate constant extracted from the fit of the CO profiles already presented in Figure IV-3.

A series of pseudo first order constant have been recorded for the photolysis of HAC in N_2 and the results of the fit have been plotted in Figure IV-4. Even if the points are scattered (probably due to the noise found in the first 25 μs, see paragraph II.7.3 page 49) the dependence is linear and present a slope of 1.81×10^{-13} cm^3 $molec^{-1}$ s^{-1}. This value can rationally represent the relaxation of CO (v=1) by collision with hydroxyacetone molecules if it is considered that in literature we found a k = 4.43×10^{-14} cm^3 $molec^{-1}$ s^{-1} for propynal (Chowdhury 2003).

Experiments were carried out in N_2 or in He. The shape of the kinetic part was greatly affected by the bath gas. In He the quenching of vibrationally excited states of CO is not efficient. At 294 K, the rate constant for the vibrational deactivation of CO in He is $k_{CO/He} = 1.66 \times 10^{-17}$ cm^3 $molecule^{-1}$ s^{-1} (Reid, Simpson et al. 1995). In N_2 the rate constant $k_{CO/N2} = 177$ s^{-1} $Torr^{-1}$, which can be converted to $k_{CO/N2} = 5.1 \times 10^{-15}$ cm^3 $molecule^{-1}$ s^{-1}, was proposed by Stephenson in 1973 (Stephenson 1973).

From the non-zero intercept of the pseudo first order plot (Figure IV-4)(Y_0 = 1163 s^{-1}), a rate constant of the vibrational quenching of CO with [N_2] = 1×10^{18} molec cm^{-3} can be derived (k= 1.16×10^{-15} cm^3 $molec^{-1}$ s^{-1}). Our value is lower than the literature one, but still is of the same order of magnitude. This difference in the kinetic is probably due to the presence of CO in several excited states. The relaxation to CO(v=0) will be then slowed down by the refill of the state CO(v=1) due to relaxation of upper vibrational states (see paragraph IV.4 page 88). Even with this difference, it is possible to affirm that N_2 participates as collisional partner for the CO(v=1) relaxation.

It is then likely that in He, quenching occurs mainly by collisions with molecules of HAC rather than by collisions with He. At a typical [HAC] of 10^{15} to 10^{16} molecule cm^{-3} and [He] of 10^{18} molecule cm^{-3}, quenching by [HAC] is four to forty times more efficient than quenching by He. Quenching by N_2 is less efficient than quenching by HAC, but due to the large amount of molecules of N_2, it dominates over quenching by HAC.

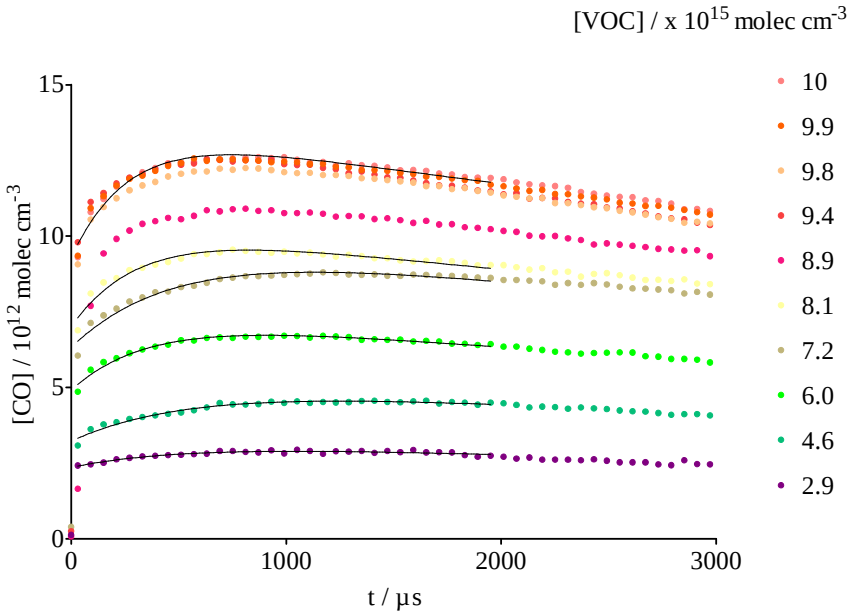

Figure IV-3 Time resolved kinetic signals of the [CO] formation in the photolysis of different [HAC]. The photolysis was performed at 26 Torr in N_2 and the laser energy was 83 mJ for a repetition rate of 5Hz.

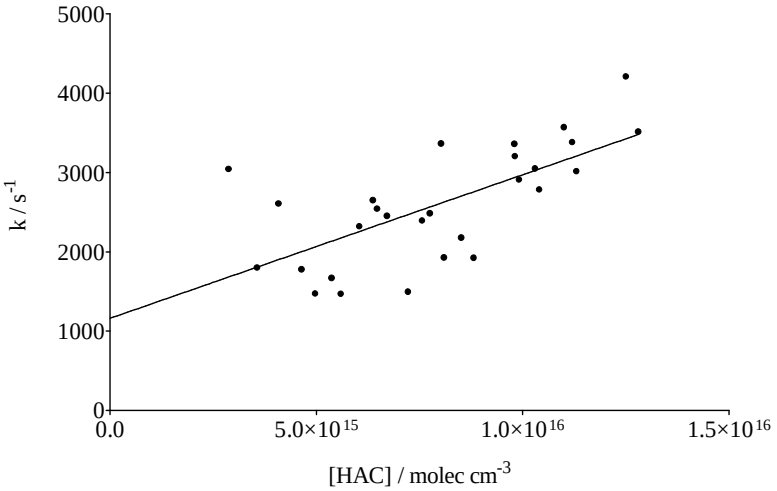

Figure IV-4 Pseudo first order kinetic constant plotted versus HAC concentration with N_2 as buffer gas. The values refers to the fits of different experiments and the result of the linear regression is $Y = 1.81\times10^{-13} X + 1163$.

In order to clarify the nature of the component CO_{slow} we decided to neglect the presence of a reaction radical-radical originating CO. To prove that CO_{slow} is not formed by secondary reactions R+R we normalized the profiles of Figure IV-3 dividing by the CO_{direct}. After this operation all signals start at the same point (Figure IV-5 left) and grows with different k to form the same amount of CO_{slow}. The results of the fit for the normalized signals are displayed in Figure IV-5 right. In case of a radical-radical reaction the normalized profiles at different [HAC] would be disposed proportionally to the [HAC], and it is not the case. In fact it is possible to remark that the values of CO_{slow} are highly scattered around the value 1.28 and that the k values draws a linear trend. The high dispersion of the points had already been encountered in Figure IV-4 and it is probably introduced by the choice of the fitting range of the raw CO profiles. The presence of an interference in the first 25 μs (paragraph II.7.3 page 49) prevented the possibility to start the fit at t=0.

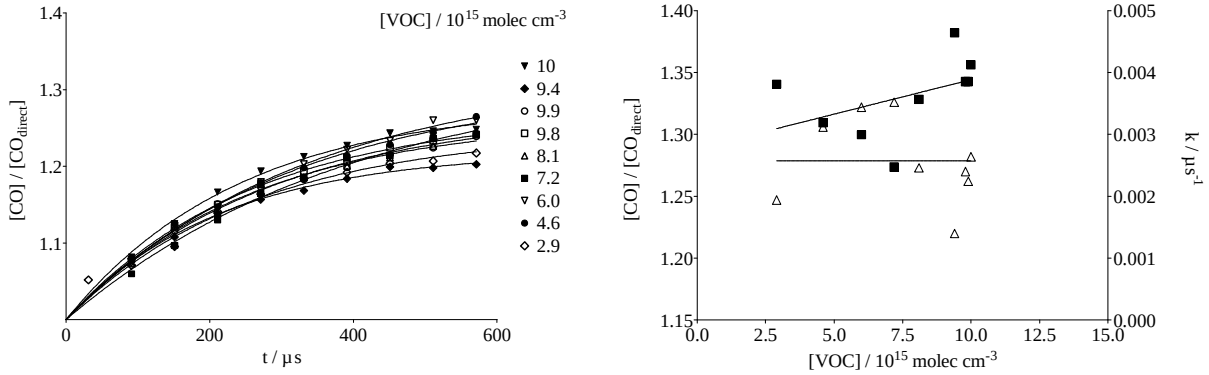

Figure IV-5 right: CO profiles of Figure IV-3 normalized respect to the CO_{direct}. Left: Dependence between the k (■) and CO_{slow} (Δ) versus the [HAC] introduced in the cell.

IV.4 CO vibrational excited states

In order to prove that the CO appearing at longer time kinetic was effectively coming from the excited states we decided to detect and record the CO formed, during photolysis, in the upper vibrational excited states. The record of these states represent a real challenge in the detection due to the weakness of the line, the low population of these states ($v \geq 1$) limitations imposed by our reference cell: pressure achievable and length of the cell (paragraph II.6.1 page 43). As matter of fact, we were obliged to perform the detection of the CO vibrational states $v>1$ using a different method with respect to CO $v=0$ (paragraph II.7.3 page 49).

Signals of CO in the excited vibrational states ($v=1,2,3$) have been successfully recorded in He as buffer gas. The signals presented in Figure IV-6 have been modelled in order to verify the relaxation constant of the upper vibrational excited states. As happened for acetone (see paragraph III.3.4 page 76), no adapted model was found to reproduce the kinetics recorded. Firstly, the intensity of the signals could not be reproduced accurately due to the difficulty on the stabilization on the absorption lines and because of the lack of literature on the CO($v>0$) absorption cross sections. In any case, to give an idea on their ratio, CO($v=1,2,3$) intensities were multiplied respectively by a factor: 2 and 3 and 4 to take into account the difference in the dipolar moments (see paragraph II.7.3 page 49). Secondly, the kinetics cannot be related with the vibrational relaxation because of irregularities generated by the baseline subtraction. Still we can obtain some important information from their shape. The first observation is that in all profiles there is a non-zero component at t=0, meaning that CO in excited states was produced almost instantaneously after the laser shot. The increase of respectively $[CO]_{v=1}$ and $[CO]_{v=2}$ just after the rapid rise could be attributed to relaxation of CO in the respectively v = 2 and v = 3 states. It might be distinguished

a very slight increase in profile of v = 3, suggesting that CO is produced also in states higher than v= 3.

Signals of the excited state CO(v=1) have been recorded also in N_2 as buffer gas (Figure IV-7). In N_2 the signals were converted into CO concentrations and a correction factor of 2 has been applied on the absorption cross section of CO(v=1) to take into account the different dipolar moment (see paragraph II.7.3 page 49). In N_2 the $[CO]_{v=1}$ presents a rapid increase in the signal predicting CO formed immediately after the laser pulse. In addition, the slight increase found in the first μs suggests the presence of a CO(v=2) state relaxing into the CO(v=1). Profiles, converted into [CO], were modelled with a Labview homemade program. The model employed is reported in Table IV-1.

reactions			*k (s^{-1})*	concentrations	*molecules cm^{-3}*
CO	->	diff	40	CO	1.90E+12
v1	->	diff	40	v1	6.50E+11
v1	->	CO	3500	v2	2.80E+11
v2	->	v1	10000		

Table IV-1 Model employed for the simulation of Figure IV-7 with relative relaxation constants and concentrations.

Differently from the signals recorded in He, the model succeed in the fit of the profiles (Figure IV-7). This difference is probably due to the simplicity of the N_2 system (only v=1) respect to He were the excited state are present up to v=4. In order to best reproduce the experimental signals we were obliged to introduce CO in the excited state v=2. Unluckily CO in the vibrational state v=2 in N_2 as buffer gas was not recorded. As previously said in the paragraph, the [CO] intensities were determined with respect to the difference in the dipolar moment (see paragraph II.7.3 page 49) but without knowing the exact cross section of the upper vibrational excited state. From the model applied we have noticed that the CO(v=1) cross section is not exactly estimated. In fact we were obliged to rise the concentration of the CO(v=1) by a factor of 1.4 to reproduce the concentration of CO_{slow} formed in the fundamental state. We can conclude that, seen the large uncertainty on the absorption cross section of the CO(v≥1), little information can be extracted from the intensities. In any case, concerning the kinetic, a great concordance with the model has been found. In the model the rate constant for the relaxation of CO(v=1) was found to be k=3500 s^{-1}. This value just approaches the rate constant k = 5000 s^{-1} found in literature (Stephenson 1973) but is in good agreement with our previous measurement (Figure IV-4). This difference can represent the effect of

the upper excited states relaxation. We suppose in fact that the kinetic of CO_{slow} formation is lowered by the progressive relaxation of the upper vibrational excited states. This means that while the vibrational state CO(v=1) relaxes, populating the fundamental state CO(v=0), CO(v=2) relaxes too, re-populating the state CO(v=1).

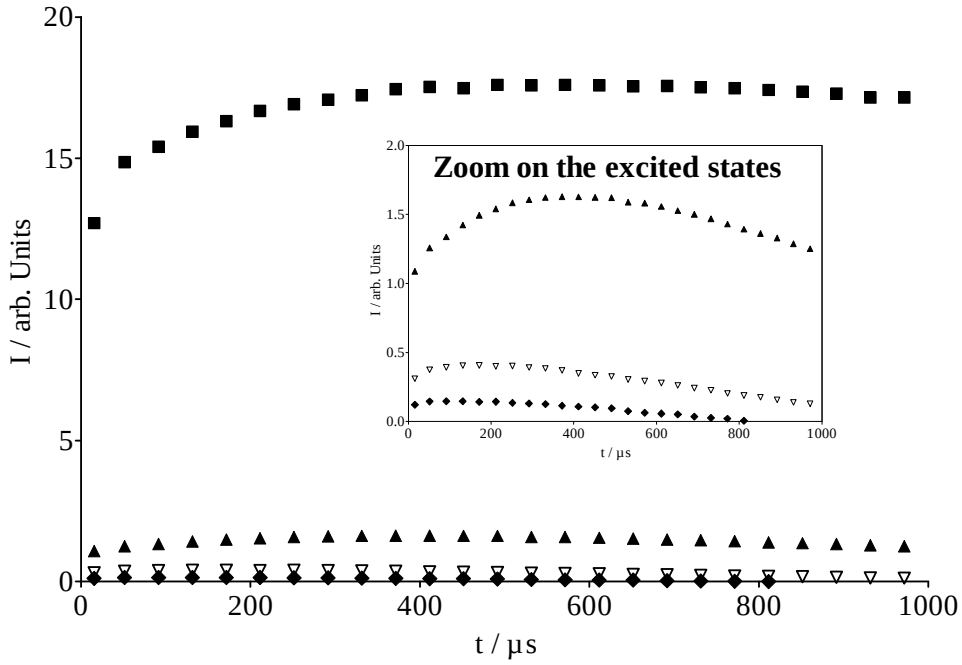

Figure IV-6 [CO] signals recorded for different vibrational states: CO v=0 (■), CO v=1 (▲), CO v=2 (∇), CO v=3 (♦), in He for a concentration of [HAC] = 1.2×10^{16} molec cm^{-3}. The photolysis was performed at 28 Torr and the laser energy was 94 mJ for a repetition rate of 5Hz.

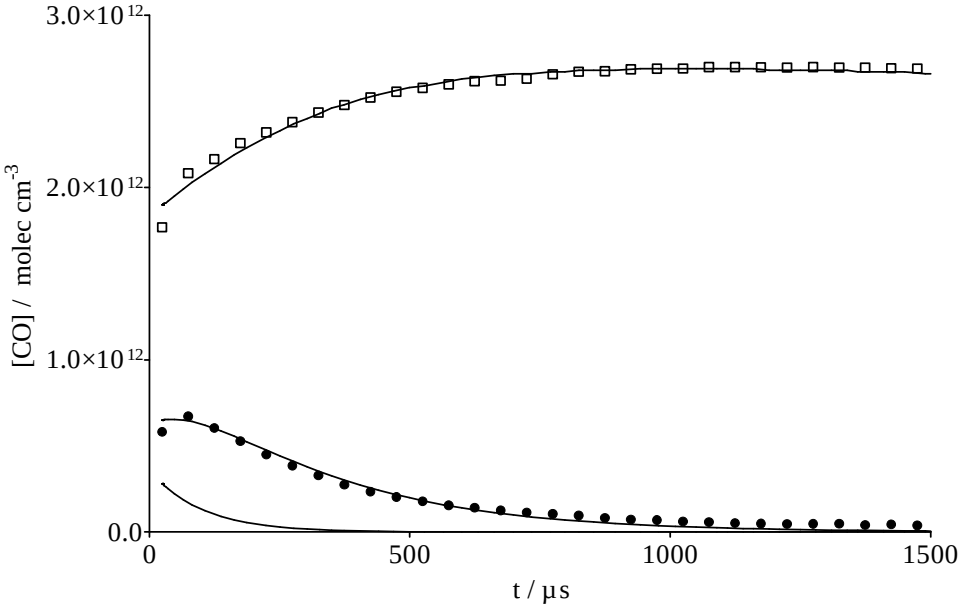

Figure IV-7 CO profiles recorded for vibrational states v=0 (□) and v=1 (•) in N_2 for a concentration of [HAC] = 1.4×10^{16} molec cm^{-3}. The photolysis was performed at 34 Torr and the laser energy was 94 mJ for a repetition rate of 5Hz. Lines represent the result of the simulation obtained applying the model presented in Table IV-1.

IV.5 Energy balance in the photodissociation of HAC.

After photodissociation of acetone at 248 nm in molecular beam conditions, North et al. (North, Blank et al. 1995) found that the average translational energy of the fragments CH_3 and CH_3CO was ≈ 60 kJ mol^{-1}. Since no data are available for hydroxyacetone, this value can be used as a hint. Dissociation of hydroxyacetone needs 334 kJ mol^{-1} and dissociation of CH_3CO 71 kJ mol^{-1}. The energy required to produce CO from the photodissociation of hydroxyacetone is then higher (465 kJ mol-1) than 448 kJ mol^{-1} if we trust the thermodynamical values reported above. It should also be noted that experiments were performed at 323 K, which could help the dissociation of CH_3CO. A 266 nm-photon provides an energy of 448 kJ mol^{-1} and CO needs ≈ 25 kJ mol^{-1} for each quantum of vibrational excitation. Even if a 266-nm photon carries enough energy to enable the production of CO in the vibrational ground state, excitation of CO up to v = 3 (which requires 75 kJ mol^{-1}) is clearly not possible.

IV.6 CO (v=1) energy dependence

In order to know whether CO in vibrational excited states came from a single or multi-photon absorption process, we recorded CO in the v = 1 state according to the fluence which was varied using a polarizer (the higher fluence was obtained removing the polarizer). The curve we have

obtained is shown in Figure IV-8. The experimental data were fitted to a polynomial function. The exponent returned is (2.02 ± 0.04), which shows that CO in vibrational states is a two-photons absorption process. The same analysis could not be performed for v = 2 and v = 3 because the S/N ratio was too low at the lower fluences used. The fact that this excited CO may come from photolysis of residual products can be discarded because the repetition rate of the laser was set at 1 Hz, which enabled the complete renewal of the mixture between two pulses.

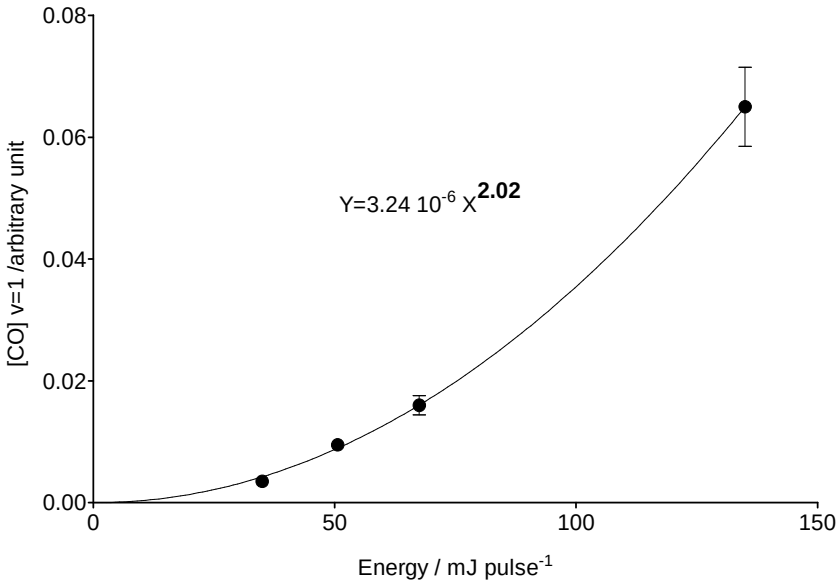

Figure IV-8 Energy dependence of [CO] (in arbitrary unit) in the vibrational state v = 1. Experimental conditions were : [HAC] = 6.6×10^{15} molecule cm^{-3}, repetition rate of the laser = 1 Hz. The fit of the experimental data to the function [CO] = $A \times E^n$ gave $A = 3.2\times10^{-6}$ and n = 2.02 ± 0.04.

IV.7 CO quantum yield results

The linear dependence of CO with the concentration of VOC introduced in the reaction cell is proportional to the quantum yield (Φ_{CO}). This condition is emphasized multipling the [VOC] by the fluence and the absorption cross section. The result of such operation is represented in Figure IV-9 where we found both CO components for three different days of analysis. From the good linearity of the regression [CO] versus the number of photons absorbed we can extract the quantum yield as the slope as presented in equation IV-11.

$$[CO] = \Phi_{CO} \cdot \{[CH_3COCH_2OH] \cdot F_{266} \cdot \sigma_{266}\} \qquad \text{IV-11}$$

From a first observation of the Figure IV-9, the weight of each photolysis pathways emerges immediately. Differently from what we found in acetone, the CO formed directly in the first µs after the UV photolysis pulse (reaction IV-4) represents the most important pathway $\Phi_{CO\ direct}$ =0.15±0.02. For hydroxyacetone in fact the CO_{slow} has little weight in the photolysis process, quantifiable as almost half of the CO direct: $\Phi_{CO\ slow}$ =0.08±0.01.

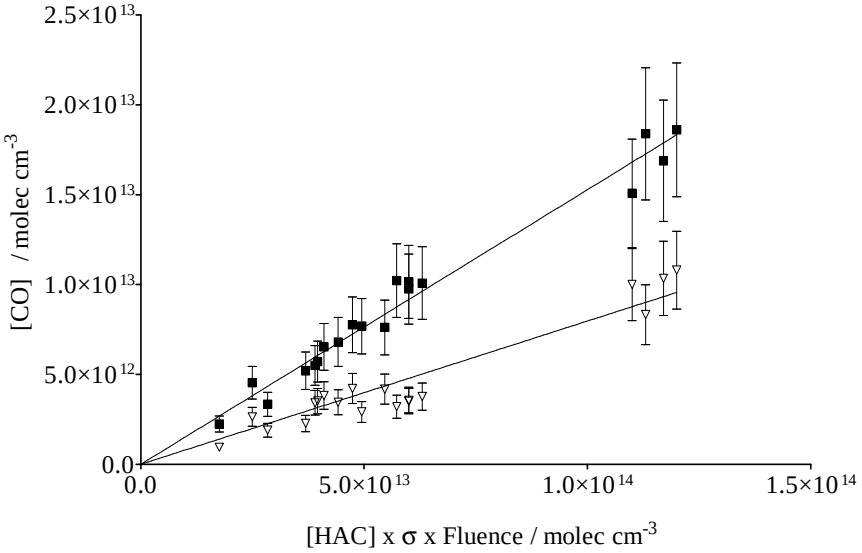

Figure IV-9 Linear relation occurring between the different component of $[CO]_{direct}$ (■) and $[CO]_{slow}$ (∇) and the [HAC] introduced multiplied by the absorption cross section and the fluence. The results of the linear regressions Y = a X are respectively: –a =0.1528 for the dark squares and –a =0.07973 for the clear triangles.

IV.8 H_2CO photolysis signals

The hydroxyacetone after photolysis produce CH_2OH radicals (IV-4) that react in the presence of O_2 to produce formaldehyde as in reaction IV-12 (Atkinson, Baulch et al. 2001).

$$CH_2OH + O_2 \rightarrow H_2CO + HO_2 \qquad \text{IV-12}$$

For the H_2CO detection, as for the CO detection, the hydroxyacetone has been introduced in the cell with the method for low vapour pressure compounds (paragraph II.5.2 page 41). Signals of H_2CO differently from the CO ones did not present any slow component because of the high concentrations of O_2 introduced in the cell. The choice of such high concentrations has been taken voluntarily to convert totally the radical in detectable formaldehyde. As we can immediately notice from Figure IV-10 the conversion of CH_2OH occur in less than the 25 µs, time close to the temporal limit of detection. H_2CO profiles presented in Figure IV-10 were fitted to a line as previously presented in paragraph II.7.4 page 53.

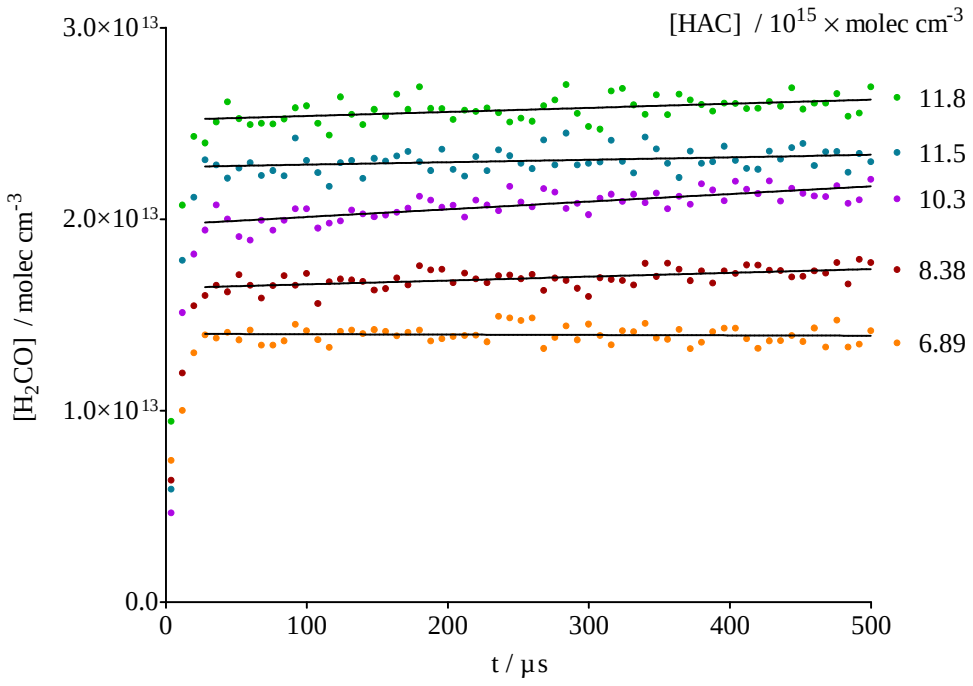

Figure IV-10 Time resolved kinetic signals of the [H_2CO] formation in the photolysis of different [HAC] in the presence of O_2. The photolysis was performed at 32 Torr in N_2 and the laser energy was 83 mJ for a repetition rate of 5Hz.

IV.9 H_2CO Quantum yield

As proved by IV-13 the concentration of H_2CO generated after photolysis of hydroxyacetone in the presence of O_2 varies linearly with the initial hydroxyacetone concentration. As previously seen for CO, from the linearity of the [H_2CO] versus the number of photons absorbed (IV-13), it is possible to obtain the value of quantum yield of the photodissociation pathway IV-4.

$$[H_2CO] = \Phi_{H_2CO} \cdot \{[CH_3COCH_2OH] \cdot F_{266} \cdot \sigma_{266}\} \qquad \text{IV-13}$$

To prove the quality of the linear regression method several series of experiments have been plotted, as function of absorbed photons, on a same graph (Figure IV-11). It is possible to remark that a good linearity and a strong agreement within different series of experiments can be found in the H_2CO yield. From the linear regression of Figure IV-11 we obtained a quantum yield of Φ_{H2CO}=0.25±0.02.

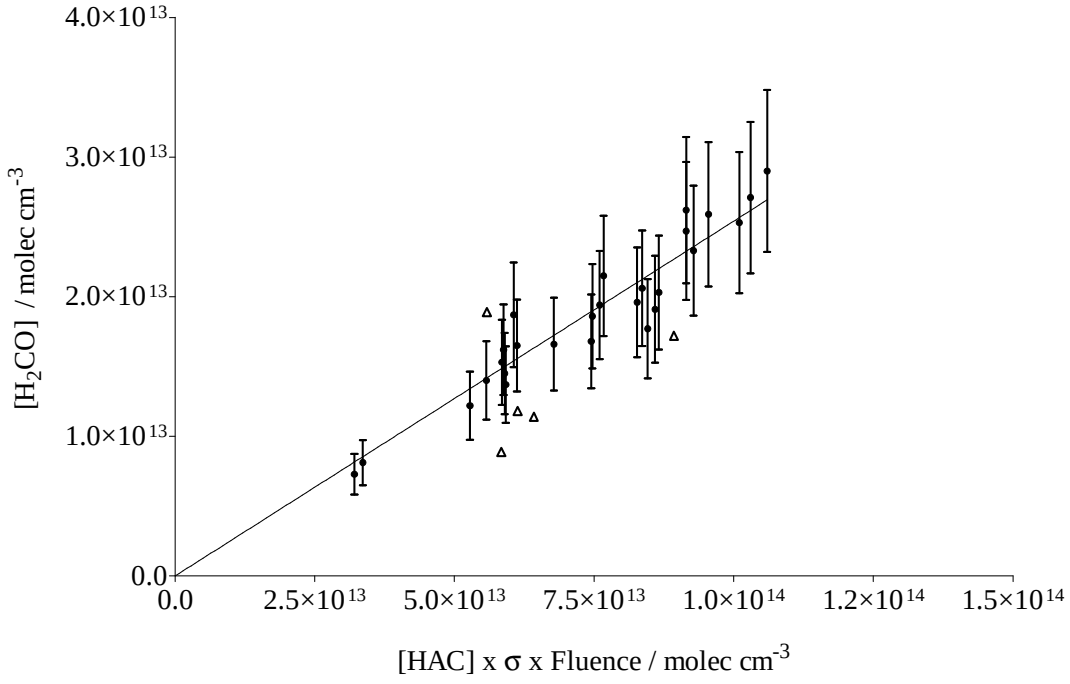

Figure IV-11 Linear dependence of the [H_2CO] with the [HAC] in presence of O_2 for different days of analysis. Clear triangles (Δ) represent the outliers. The result of the linear regressions is Y = 0.254X.

IV.10 Hydroxyacetone conclusions

With the TDLAS technique we have been capable to trace the temporal evolution of CO and H_2CO in the photolysis process of hydroxyacetone at 266 nm. Confirming the model proposed in literature for the photodissociation of ketones (Chowdhury, Upadhyaya et al. 2002; Blitz, Heard et al. 2006) we detect and record the formation of CO immediately after the photolysis pulse, proof of the existence of the reaction III-3. Varying the hydroxyacetone concentration inside the cell we established the parameter of the quantum yield for the photodissociation process at 266 nm. This value for CO direct formed in reaction III-3 is determined to be $\Phi_{CO\ direct}$ =0.15±0.02. This photolysis way is considered to be the predominant at the chosen wavelength because of the estimated $\Phi_{CO\ slow}$ =0.08±0.01 over a total of $\Phi_{CO\ tot}$ =0.23±0.04.

CO formed in the kinetic is supposed to be the CO in the vibrational excited states, relaxing by collisions with N_2 or He. The presence of CO in the upper vibrational excited states have been documented in two different buffer gas He (CO v=1, 2, 3) and in N_2 (limited at CO v=1). The energetic balance is justified by a two photons absorption process proved varying the UV fluence for the photolysis.

Formaldehyde formed in the reaction of the CH_2OH fragment with O_2, has been detected as a product of the hydroxyacetone photolysis at 266. The estimation of the H_2CO quantum yield gives a value of Φ_{H2CO}=0.25±0.04.

The possibility to detect both CO and H_2CO gave an opportunity to evaluate the photodissociation pathway IV-4 from the point of view of both photofragment: in the detection of H_2CO we followed the CH_2OH radical while in the CO detection we trace the dissociation of CH_3CO^*. Due to the O_2 excess, the CH_2OH radical was totally converted into formaldehyde (IV-12); as a consequence the Φ_{H2CO} will represent the quantum yield of the photodissociation path (IV-4). On the other hand the lower quantum yield of CO is limited by the dissociation ratio of the CH_3CO^* radical. From the ratio of the two quantum yield we can estimate that, in our experimental condition, the dissociation of the CH_3CO^* is quantifiable as:

$$CH_3CO^*_{not\cdot dissociated} = \frac{\Phi_{H_2CO} - \Phi_{COtot}}{\Phi_{H_2CO}} = \frac{0.25 - 0.23}{0.25} = 0.08 \qquad \text{IV-14}$$

This value can be compared with the calculation made by Rajakumar (Rajakumar, Gierczak et al. 2008) on the ratio of the dissociated CH_3CO^* over the stabilized by collision. He reported a value of $k_{(III-4)}/k_{(III-3)} = 8\times10^{-20}$. For $[N_2] \approx 10^{18}$ molecule cm^{-3} give a ratio of 0.08. This value is in agreement with that found in our experiment and can represent an additional proof of the dissociation path III-3.

V. Photolysis of methyl vinyl ketone at 355 nm

V.1 Previous studies

Methylvinylketone (MVK) is the simplest unsaturated ketone which can be formed in the atmosphere by the troposheric oxidation of isoprene (Paulot, Crounse et al. 2009). The main pathway of degradation of MVK is its reaction with the OH radical which was studied by Gierczak *et al.* in 1997 (Gierczak, Burkholder et al. 1997) and in 2005 by Romero *et al.* (Romero, Blitz et al. 2005).

Gierczak measured the rate coefficients for the reaction of OH with MVK over the temperature range 232 – 378 K mainly at a pressure of 100 Torr of N_2. OH radicals were produced by pulsed photolysis of H_2O_2 at 248 nm or 266 nm, where the photolysis of MVK did not influence the results. Their value at 298 K is 2.03×10^{-11} cm^3 $molec^{-1}$ s^{-1}. They were able to derive the Arrhenius parameters from their results at various temperatures and found $A = (2.67 \pm 0.45)\times10^{-11}$ cm^3 $molec^{-1}$ s^{-1} and $E/R=(-612 \pm 49)$ K. The reaction of MVK with OH results in a lifetime in the atmosphere of 6 to 10 hours.

The photolysis of MVK can occur in the three following pathways depending on the photolysis wavelength (Romero, Blitz et al. 2005):

$$CH_3COCHCH_2 + h\nu \rightarrow C_2H_3 + CH_3CO \qquad \Delta H°_1 = 405 \text{ kJ mol}^{-1},\ \lambda_1 = 295.3 \text{ nm} \qquad \text{V-1}$$

$$CH_3COCHCH_2 + h\nu \rightarrow C_2H_3CO + CH_3 \qquad \Delta H°_2 = 449 \text{ kJ mol}^{-1},\ \lambda_2 = 266 \text{ nm} \qquad \text{V-2}$$

$$CH_3COCHCH_2 + h\nu \rightarrow C_3H_6 + CO \qquad \Delta H°_3 = 247 \text{ kJ mol}^{-1},\ \lambda_3 = 484.2 \text{ nm} \qquad \text{V-3}$$

For MVK the single bond cleavage leads to the production of two different acyl radicals but the molecular channel (V-3) is the most accessible. Working at 355 nm we will expect only the molecular channel (V-3) to occur.

The photolysis of MVK was studied at 193.3 nm by Fahr *et al.* in 1993 (Fahr, Braun et al. 1993) as a clean source of vinyl radicals. In 1997, Gierczak *et al.* (Gierczak, Burkholder et al. 1997) performed quantum yields measurements of MVK at 308, 337 and 351 nm, with fluence varying in the range 6 – 140 mJ cm^{-2} $pulse^{-1}$, measured using the photolysis of NO_2 as reference. Quantum yields were derived from the loss of MVK using gas chromatographic analysis. O_2 was added in large excess in order to reduce unwanted secondary reactions. Pressure was set to 25 or 650 Torr.

At 351 nm, which is close to our study at 355 nm, the quantum yield was found to be extremely small, lower than 0.01, with no effect of pressure. At 308 nm, the quantum yield decreased with

increasing pressure, which was not any more the case at 337 nm. They did not observe CO or CO_2 as end products of photolysis. Major detected end products were acetylene, propylene and methanol in agreement with a study by Raber and Moortgat (Raber and Moortgat 1996) who concluded that the major primary photolysis products of MVK was C_3H_6 and CO.

In their paper published in 2005, Romero *et al.* gave quantum yields for acyl radical production at 308 nm and 320 nm for MEK, DEK and MVK, by monitoring the OH production from the RCO + O_2 reaction by LIF at 282 nm. They concluded that the dominant radical dissociation mechanism was CH_3CO + R (Romero, Blitz et al. 2005).

Two acyl radicals may be expected. The pressure dependence of the rate coefficients for OH production in the photolysis of MVK and acetone is the same and clearly different of the pressure dependence of the reaction C_2H_5CO + O_2. For MVK, the dominant radical pathway is the vinyl radical elimination but the main pathway is clearly C_3H_6 + CO.

In 2009, Earle *et al.* (Earle, Mills et al. 2009) photolyzed MVK at 308 nm in order to determine the importance of each pathway of photolysis and to analyse the effect of the presence of oxygen on these yields. Chemical analysis was performed by gas chromatography with a good resolution for CH_4, C_2H_2, C_2H_6, C_3H_6 and 1,3-C_4H_6. Photolysis of NO_2 was used as comparison to obtain reliable quantum yields. The fluence of the laser in the experiments was in the order of a few mJ cm^{-2} $pulse^{-1}$. The used cross section at 308 nm was taken as 6.24×10^{-20} cm^2 assumed not to depend on temperature, which was varied in the range 300 – 475 K. At room temperature, they derived a ratio [C_3H_6] / [CO] of 0.78 ± 0.04, in agreement with the previous value of Raber and Moortgat (Raber and Moortgat 1996), indicating that there could exist another source of CO than the molecular channel. If CH_4 was formed, one would expect CH_2=C=C=O to be detected (or CO + C_2H_2). It was not the case, but the authors pointed out that this compound could have been missed in their chromatographic analysis.

Small yields of C_2H_2, C_2H_4, C_2H_6 and 1,3-C_4H_6 were detected, but only at high temperatures. The conclusion is that the radical channels are not the main channels in the photolysis of MVK at 308 nm.

The quantum yield of C_3H_6 varied linearly with the fluence, which showed the process not to be multiphoton. Secondary chemistry was also discarded because the yields of C_3H_6 and CH_4 were independent of the number of pulses. The variation with pressure observed by Gierczak et al. and Raber and Moortgat in their experiment measuring the loss of MVK is consistent with the observed dependence of the yields of C_3H_6 or CH_4.

At 474 K, which is quite a high temperature, a radical channel seems to be opened, since C_2H_2, C_2H_4, C_2H_6 and 1,3-C_4H_6 were detected. The quantum yield of propylene formation at 10 Torr and 300 K was found to be 0.08 ± 0.02 in pure MVK.

Measurements of the absorption cross section of methyl vinyl ketone (see Figure V-1) were performed in the range 213 – 359 nm with the absorption maximum occurring at around 330 nm ($\sigma_{330} = 7.3\times10^{-20}$ cm^2) (Raber and Moortgat 1996; Gierczak, Burkholder et al. 1997). The absorption rapidly drops at 380 nm but at 355 nm, methyl vinyl ketone still has an appreciable absorption cross section of $\sigma_{355} = 4.15\times10^{-20}$ cm^2.

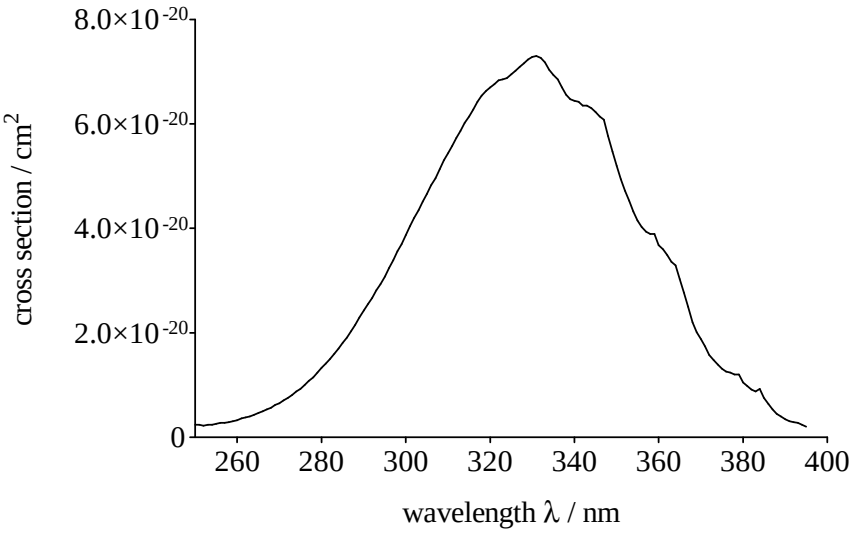

Figure V-1 Linear UV absorption cross section of methyl vinyl ketone at 298 K (Gierczak, Burkholder et al. 1997).

It should be taken into account that working at 355 nm, the energy of one photon (338 kJ mol^{-1}) is not sufficient to generate the acyl radical (V-1 and V-2), reason why no other possible ways of CO formation exists at this wavelength and in the time scale of the reaction. In addition, seen the low energy threshold of the molecular channel (247 kJ mol^{-1}), a small amount of exceeding energy will be distributed within the nascent CO and C_3H_6 (91 kJ mol^{-1}). Somnitz et al. evaluated the distribution of remaining energy after photodissociation for acetone (Somnitz, Fida et al. 2005) and estimate that 43% will be dissipated in the relative motion of the photofragments and 46% is kept within the CH_3CO* radicals. Seen that no data are available for MVK and seen that the molecular channel is the most energetically probable, we take the value of 11 % as an indication to evaluate the energy conserved by CO after photolysis. This energy (10 kJ mol^{-1}) is not sufficient to reach the vibrational state CO v=1 (≈ 25 kJ mol^{-1} for each quantum of vibrational excitation).

V.2 Experimental details.

In this work the photolysis of methyl vinyl ketone has been performed at 355 nm achieved by changing the laser YAG harmonic 4ω crystal for the 3ω tripling frequency crystal (paragraph II.3 page 34). The compound has been introduced in the cell with the method of the bubbler, placed in a thermo-stated bath at 40°C (paragraph II.5.2 page 41). Actually, the high vapor pressure of methyl vinyl ketone allows operating at the ambient temperature. The concentrations of the methyl vinyl ketone have been determined, during the course of the analysis, with the manually stabilized bubbler pressure presented in paragraph II.5.2 page 41. The bubbling pressure (from which depends the concentration inside the cell) was manually stabilized regulating a needle valve. The pressure inside the bubbler was read by a pressure gauge having an operation range of 1-1000 ±1 Torr. A flux of N_2 (AirLiquid products 99%purity) has been used to achieve concentrations of VOC in the cell in the range $2.6\times10^{16} – 5.5\times10^{16}$ molec cm^{-3}.

V.3 CO profiles in the MVK photolysis at 355 nm

As for acetone and hydroxyacetone, previously presented in chapter III and IV, CO signals present the same shape and were fitted to equation V-4.

$$[CO] = ([CO]_{direct} + [CO]_{slow} \times (1 - e^{-k' \times t})) \times e^{-k_{diff} \times t} \qquad \text{V-4}$$

They are composed by two different components (Figure V-2): a first component called CO_{direct} appearing immediately after the photolysis pulse and a second one called CO_{slow} formed at longer reaction time. The first component is the CO formed by the molecular channel (V-3), while the CO_{slow} is suspected to be originated CO formed by reaction V-3 and present in the excited vibrational states that relaxing populate the fundamental one.

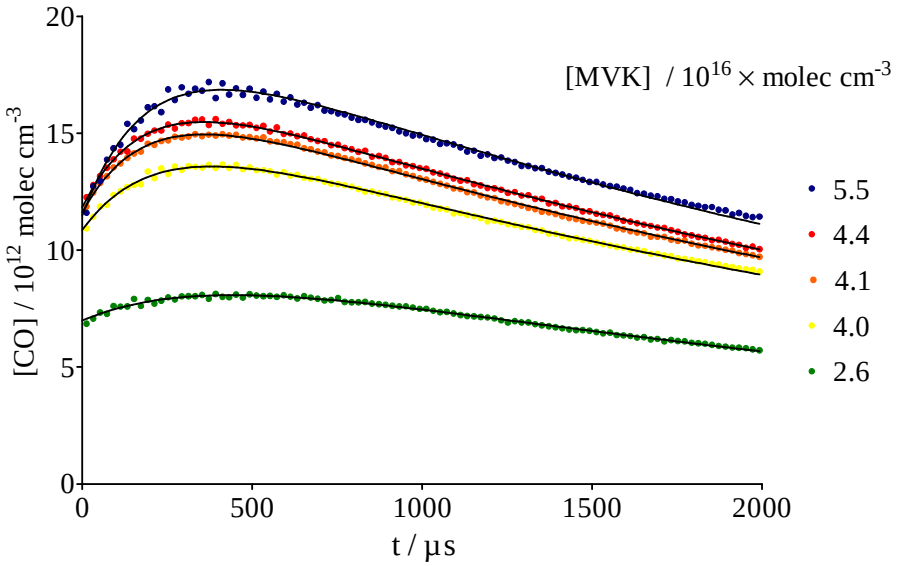

Figure V-2 Time profiles of [CO] obtained in the photolysis at 355 nm of different MVK concentrations. The photolysis was performed at 28 Torr in N_2 and the laser energy was 135 mJ for a repetition rate of 5 Hz.

The two component CO_{slow} and CO_{direct} extracted from the fit of Figure V-2 are shown in Figure V-3. Both components present a linear dependence with the methyl vinyl ketone concentrations introduced in the cell. For the linear regression of the CO_{direct} (dots in Figure V-3) concentrations the last point of the curve has been excluded because of a saturation of methyl vinyl ketone in the bubbler. The removal of this point is also justified by the Pearson coefficient. The R^2 parameter of the linear regression with the last point included was $R^2 = 0.3267$, absolutely too low, while with its exclusion it rose to $R^2 = 0.9845$. From the linearity encountered in Figure V-3 we can deduce that the process of CO_{slow} formation is due to relaxation of vibrational excited states of CO and cannot be a radical-radical reaction, from which we will have expected an exponential dependence.

In addition, to clarify the nature of the component CO_{slow} and to prove that CO_{slow} is not formed by secondary reactions R+R we normalized the CO profiles dividing by the CO_{direct}. After this operation all signals start at 1 (Figure V-4) and grows with different k to form the same amount of CO_{slow}. It is possible to remark that the values of CO_{slow} are highly scattered around the value 2. In case of a radical-radical reaction the normalized profiles at different [MVK] will be disposed proportionally to the [MVK], and it is not the case.

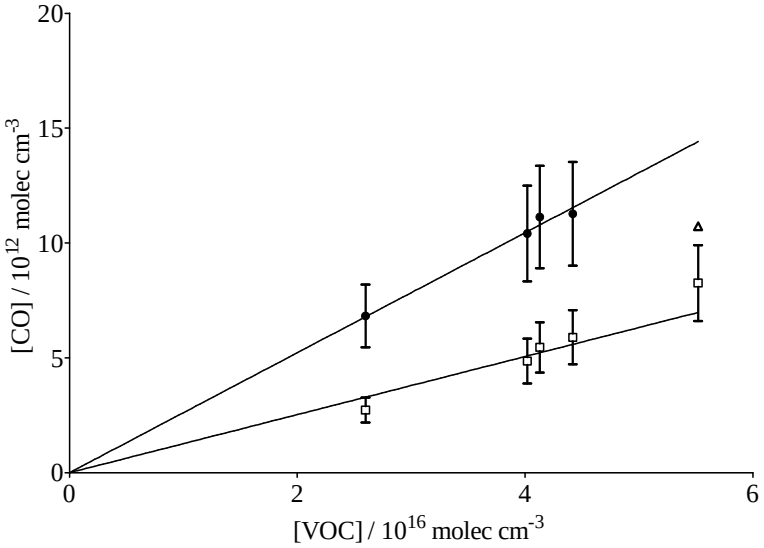

Figure V-3 CO_{direct} (•) and CO_{slow} generated in the upper vibrational excited states (□) as function of the methyl vinyl ketone concentrations. Triangle (Δ) represent the outlier.

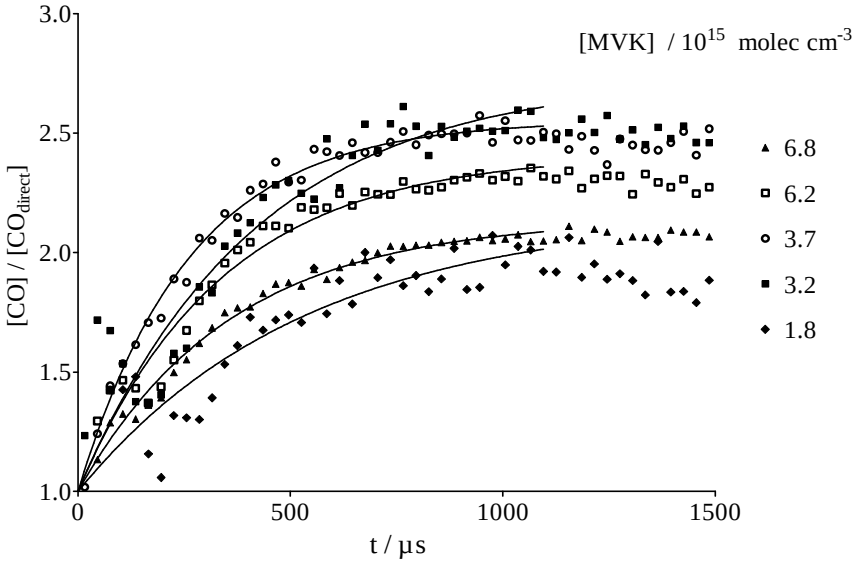

Figure V-4 CO profiles at different [MVK] normalized respect to the CO_{direct}. Experiments were performed at 29 Torr in N_2.

V.4 Quantum yield results

The CO formed in the methyl vinyl ketone photolysis, as described in equation V-5, depends on the wavelength of the radiation, on the laser fluence and on the quantum yield

$$[CO] = \Phi \times \{[CH_3CO\text{CHCH}_2] \times F_{355} \times \sigma_{355}\} \qquad \text{V-5}$$

where the absorption cross section σ_{355} = 4.15×10^{-20} cm^2 $molec^{-1}$ and the fluence F = 3.8×10^{17} photons cm^{-2} .

Plotting [CO] versus absorbed photons is possible to derive the quantum yield simply from the slope of the equation formed fitting the points (Figure V-5) with a linear regression. The results of this calculation give back the values of the quantum yield for each CO pathways $\Phi_{CO\ direct}$ = 0.016 ± 0.002 and $\Phi_{CO\ slow}$ = 0.008 ± 0.001. For CO, the total quantum yield value determined for the MVK photolysis is estimated as the sum of both:

$$\Phi_{COtot} = \Phi_{COdirect} + \Phi_{COslow} = 0.016 + 0.008 = 0.024 \qquad \text{V-6}$$

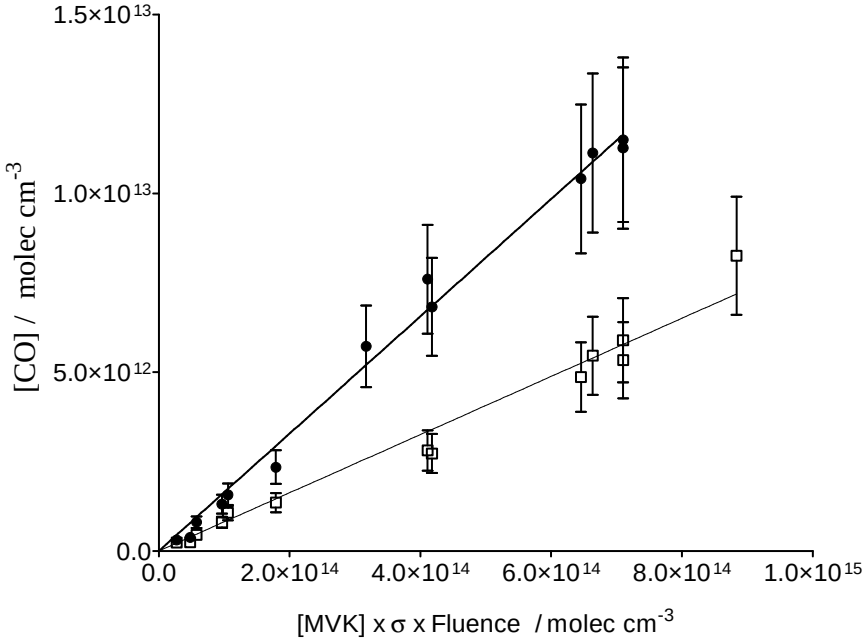

Figure V-5 Quantum yield for the photolysis of methyl vinyl ketone with the distinction of the two components : CO_{direct} (•) , CO_{slow} (□).

V.5 Methyl vinyl ketone conclusions

The technique of TDLAS is proved to be a useful tool for the detection of CO in the photolysis of methyl vinyl ketone at the wavelength 355 nm. The great advantage of this technique is the capability to follow the apparition of CO on a ms time scale. It has been proved the presence of CO formed immediately after the photolysis pulse, confirming the mechanism (V-3) proposed in the literature (Raber and Moortgat 1996). This direct path of CO formation has been detected to be the major pathway and it is quantified from the value $\Phi_{CO\ direct} = 0.016 \pm 0.002$. It has been proved also the existence of another pathway of CO formation at longer reaction time. This CO_{slow} is suspected to be the relaxation of upper vibrational excited state of CO. The quantum yield obtained for this process is defined by $\Phi_{CO\ slow}=0.008 \pm 0.001$. The total quantum yield value determined for the methyl vinyl ketone photolysis ($\Phi_{CO\ tot} = 0.024$) is in good agreement with the values of Raber and Moortgat, estimated to be $\Phi_{CO\ tot} = 0.023 \pm 0.003$.

VI. Photolysis of 3,3,3-trifluoro propionaldehyde (CF_3CH_2CHO) at 266 nm

VI.1 Previous studies

The phase out of chlorofluorocarbons (CFCs) began in the 1987 with the Montreal protocol that planned their slow diminution until the zero emission fixed in 1996 (UNEP). This decision was justified by the discovering by Molina and Rowland (Molina and Rowland 1974) a few years before of their implication in the destruction of the stratospheric ozone. Major chemical factories started to be interested in alternatives to CFCs since the 1980s. CFCs were progressively replaced by Hydro Chloro Fluoro Carbons (HCFCs), also responsible for the ozone depletion but much less than their precursors CFCs (EPAdefinition). The HCFCs are less stable in the lower atmosphere than their ancestors CFCs. The direct consequence of their higher reactivity at low altitude is the lower impact that these compounds have in the enlargement of the ozone hole (Kelly, Bossoutrot et al. 2005). More recently in 2007, approximately 200 countries agreed to accelerate the entire elimination of hydrochlorofluorocarbons by 2020 (UNEP) .

The modern successors of HCFCs are hydrofluorocarbons (HFCs), that progressively enter in the markets because they are not ozone destructors. For example, DuPont began to produce HFCs immediately after the ban of the CFCs (DUPONT). The hydrofluorocarbons (HFCs), chlorine free alternatives, have even shorter lifetimes in the lower atmosphere then their ancestors (Wallington, Dagaut et al. 1987; Hurley, Wallington et al. 2004). They are used principally as refrigerants and widely employed in mobile air conditioning systems. Their large application is principally driven by their excellent thermodynamic properties and performances at high temperatures. At the same time, these three groups of halocarbons are powerful greenhouse gases with very high Global Warming Potential. Exactly for this reason, in 2005, the HFCs have been included in the Kyoto Protocol (www.kyotoprotocol.com).

Recently, hydrofluoroethers (HFEs) and partially fluorinated alcohols, like the family of $CF_3(CH_2)_xCH_2OH$, have been suggested as alternatives for HFCs and HCFCs (Sellevåg, Kelly et al. 2004; Sellevåg, Stenstrøm et al. 2005). As their ancestors, partially fluorinated alcohols have been used in applications such as: cleaning of electronic components, refrigeration, and carrier compounds for lubricants. Since their introduction on the market, a number of investigations on the kinetics and mechanisms for the atmospheric degradation of CF_3CH_2OH has been performed trying to prevent the great damage occurred with the CFCs (Wallington, Dagaut et al. 1987).

Nowadays, it is known that fluoroaldehydes (C_xF_yCHO), are primary degradation products in the gas-phase oxidation of the respective alcohols (Sellevåg, Kelly et al. 2004; Antiñolo, Jiménez et al. 2009). For fluorinated aldehydes, as it has been observed for the ketones, the major tropospheric sinks are the reaction with OH radicals and photolysis (Kelly, Bossoutrot et al. 2005). In recent years, several studies have been performed on the determination of the OH rate constant with CF_3CH_2CHO. The results obtained by LIF and FTIR are presented in Table VI-1.

Temperature / K	k / 10^{-12} × cm^3 $molec^{-1}$ s^{-1}	technique	reference
298	2.59	PLP/LIF	(Antiñolo, Jiménez et al. 2009)
298	2.96	PLP/LIF	(Kelly, Bossoutrot et al. 2005)
296	2.57	RR/FTIR	(Hurley, Wallington et al. 2004)

Table VI-1 Rate constant for the reaction of CF_3CH_2CHO with OH radicals, determined by several authors.

A first reason for the study of fluorinated aldehydes is that up to now no natural source has been found for the trifluoroacetic acid, but in a recent study fluorinated aldehydes were thought to be an indirect source of CF_3COOH in the atmosphere (Antiñolo, Jiménez et al. 2009) . A second reason justifying this study is that, while their reaction with OH radicals is well documented (Table VI-1), only few data are present in the literature describing the photolysis process of the 3,3,3-trifluoro propionaldehyde. A study on the photolysis of CF_3CH_2CHO between 290-400nm was performed by Sellevåg (Sellevåg, Kelly et al. 2004) reporting a quantum yield lower than 0.04. Another pioneer study was performed in the frame of the EU project "RADICAL" (Moortgat 2000), where it was found that the effective quantum yields of CF_3CHO and CF_3CH_2CHO photolysis were respectively 0.06±0.1 and 0.25±0.04. Another study of the photolysis process of this fluorinated aldehyde has been performed by Chiappero in 2006 (Chiappero, Malanca et al. 2006). In his work, performed at 700 Torr (very different from our conditions: 30 Torr), they estimated the quantum yield to be Φ_{tot} = 0.74±0.08 at 254 nm and only Φ_{tot} = 0.04±0.01 at 308 nm (Chiappero, Malanca et al. 2006). A more recent work on the photolysis of the 3,3,3-trifluoro propionaldehyde at 308 nm has been performed by Antiñolo et al. (Antiñolo, Jiménez et al. 2011). They measured the quantum yield at 308 nm and trace the time resolved evolution of the photoproducts by FTIR. The quantum yield has been found as Φ_{tot} = 0.026±0.01 at 760 Torr Air, in good agreement with the earlier literature (Sellevåg, Kelly et al. 2004; Chiappero, Malanca et al. 2006).

In both studies the different possible photolysis pathways of 3,3,3-trifluoro propionaldehyde photolysis process have been proposed to be as follows (Chiappero, Malanca et al. 2006; Antiñolo, Jiménez et al. 2011):

$$CF_3CH_2CHO + h\nu \rightarrow CF_3CH_2 + HCO \qquad \text{VI-1}$$

$$CF_3CH_2CHO + h\nu \rightarrow CF_3CH_2CO + H \qquad \text{VI-2}$$

$$CF_3CH_2CHO + h\nu \rightarrow CF_3CH_3 + CO \qquad \text{VI-3}$$

In the presence of O_2, HCO radicals formed in reaction II-1 are converted into CO, detectable by our system, through the fast reaction VI-4.

$$HCO + O_2 \rightarrow HO_2 + CO \qquad \text{VI-4}$$

This reaction has been widely studied using many different techniques; from UV-Vis absorption (Colberg and Friedrichs 2006) to mass spectrometry (Nesbitt, Gleason et al. 1999) and its rate constant is well known: $k_{VI-4} = 5.2\times10^{-12}$ cm^3 $molec^{-1}s^{-1}$ (Atkinson, Baulch et al. 2001).

Antiñolo et al. (Antiñolo, Jiménez et al. 2011), determined the degradation products of the 3,3,3-trifluoro propionaldehyde photolysis at 308 nm and found the CF_3CH_3 IR absorption can be below the detection limit and an upper limit for that channel was reported to be 5%. The same result has been found in a more recent work after 266 and 248nm photolysis (E. Jimenez, private communication). For this reason they have neglected the possibility of the third channel (VI-3) to be open and interpreted their data considering only reaction (VI-1) and (VI-2). To justify the detection of CO they proposed two reactions: the conversion of HCO in presence of O_2 (VI-4) and the possible decomposition of CF_3CH_2CO from (VI-5).

$$CF_3CH_2CO \rightarrow CF_3CH_2 + CO \qquad \text{VI-5}$$

They estimated, like Somnitz has done for the CH_3CO radical (Somnitz, Fida et al. 2005), the internal energy available for the dissociation to be 49 kJ mol^{-1}. They conclude that at 308 nm the barrier of dissociation can be achieved with one photon and, as a consequence, part of the CO detected originated also from reaction VI-5.

In this work we detect the CO formed after the photolysis of CF_3CH_2CHO at 266 nm. At this wavelength the photon energy is sufficient to open channel (VI-2). In previous studies it has been shown that the lifetime of the excited CH_3CO^* radical is lower than 100 ns (Somnitz, Fida et al.

2005; Rajakumar, Gierczak et al. 2008). No study has been performed on the CF_3CH_2CO lifetime, however we estimate it to be on the same order of magnitude and consider, that all CO that is formed immediately on our time scale originates from a decomposition of $CF_3CH_2CO^*$.

In order to quantify the yield of HCO radicals formed in reaction II-1 we performed the photolysis in presence of high concentration of O_2, leading to a rapid conversion of HCO radicals, formed in reaction (VI-1), into detectable CO (VI-4).

The UV spectrum of CF_3CH_2CHO displayed in Figure VI-1 was measured by Sellevåg, Chiappero and later by Antiñolo et al (Sellevåg, Kelly et al. 2004; Chiappero, Malanca et al. 2006; Antiñolo, Jiménez et al. 2011). There is a slight difference between the spectra but the values at 266 nm are in good agreement within each other. We employed the value of Sellevåg that at 266 nm gives an absorption cross section of $\sigma_{266\ nm} = 1.96\times10^{-19}$ cm^2 molec^{-1}.

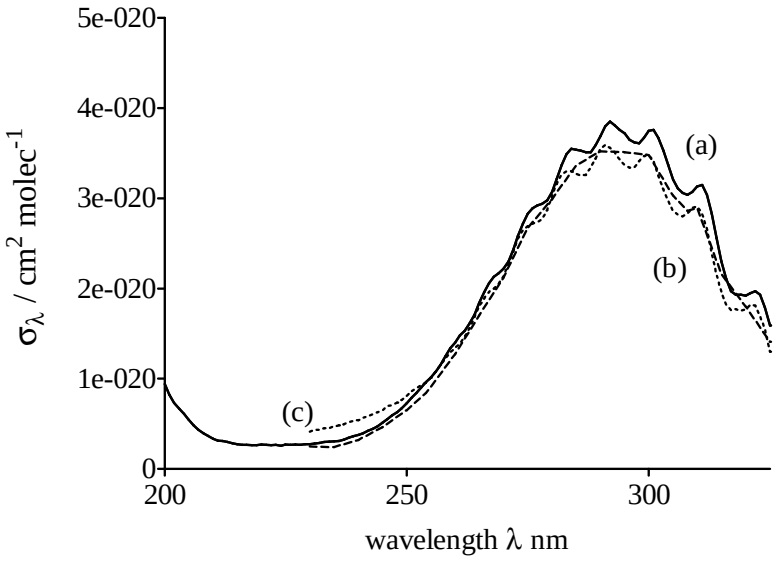

Figure VI-1 UV absorption cross section of 3,3,3-trifluoro propionaldehyde at 298 K by (a) solid line (Sellevåg, Kelly et al. 2004) and (b) dash line (Chiappero, Malanca et al. 2006) (c) dot lines (Antiñolo, Jiménez et al. 2011).

VI.2 Control of 3,3,3-trifluoro propionaldehyde concentration in the photolysis cell

The 3,3,3-trifluoro propionaldehyde was purchased from Apollo Scientific Reagents. It has been introduced into the cell from diluted mixtures, prepared in balloons as explained in paragraph II.5.1 page 39. The balloons have been prepared introducing a pressure of 30 Torr of 3,3,3-trifluoro propionaldehyde and subsequently diluted with He or N_2 up to a pressure of 1000 Torr. Either N_2 or He (AirLiquid products 99% purity) have been used as carrier gas. Experiments were performed at room temperature using aldehyde concentration between 2.1×10^{15} and 7.7×10^{15} molec cm^{-3}, at a total pressure of 30 Torr and a temperature of 293 K. A flow of pure O_2 (AirLiquid products 99%

purity) was added to the mixture inside the cell in order to convert HCO radical into detectable CO. The O_2 flow was varied to achieve concentrations between 0.8×10^{15} (minimum achievable O_2 concentration due to leak rate) and 2.6×10^{17} molec cm^{-3}.

VI.3 CO profiles with high and low O_2 concentration

Typical CO signals obtained are shown in Figure VI-2. The profile displayed in black was obtained using a high concentration of O_2, while the profile displayed in gray was obtained with a very low concentration of O_2 due to a leak (see paragraph VI.4 page 112). Even this latter showed an instantaneous (at our time scale) production of CO which meant that it was produced by a direct photodissociation of the aldehyde (VI-5). The concentration of CO increased until around 500 μs: this slow formation is due to the presence of trace amounts of O_2 that converts HCO slowly into CO by reaction VI-4. From a fit of these data to an exponential increase (typically $k \approx 4000\ s^{-1}$) the O_2 concentration due to the leak can be estimated to be around $[O_2] = 8\times10^{14}$ cm^{-3}. The decay at longer times was due to diffusion of CO out of the IR probe beam.

The profile in dark gray showed a fast increase of [CO] in the first few microseconds. This fast increase was due both to direct production of CO (VI-5) and fast conversion of HCO into CO (VI-4) which could not be distinguished when high O_2 concentrations was used.

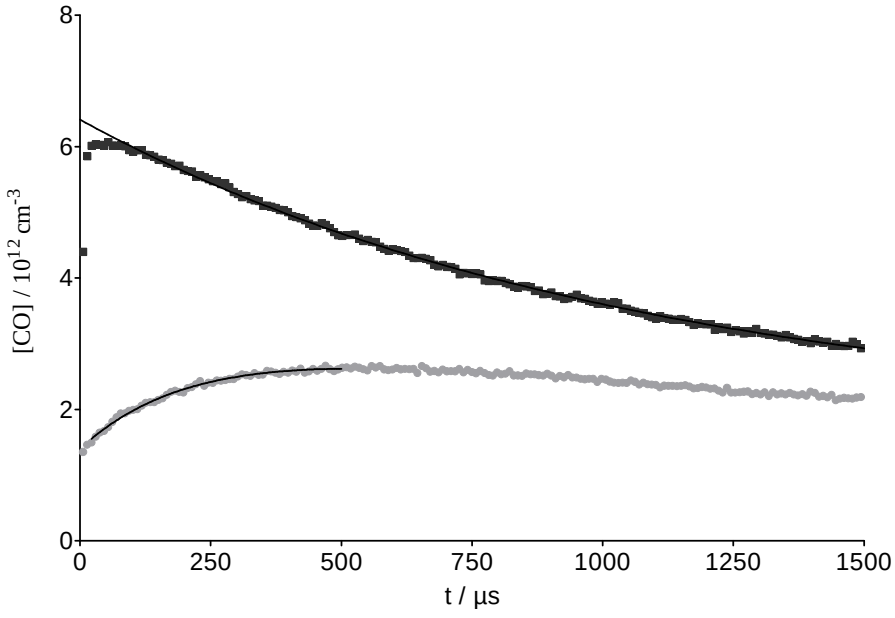

Figure VI-2 CO profiles originated from the photolysis of the 3,3,3-trifluoro propionaldehyde with low O_2 concentrations $[O_2] = 8.2\times10^{14}$ molec cm^{-3} (gray dots) and in presence of high O_2 concentrations $[O_2] = 3.3\times10^{16}$ molec cm^{-3} (black dots).

VI.4 Origin of the kinetic part in the time-profiles of [CO]

The rate constant of the HCO+O_2 reaction (VI-4)(equal to the CO formation rate after the laser pulse) was verified by carrying out experiments in an excess of O_2 ([O_2] = from 4.4×10^{15} to 4.2×10^{16} cm^{-3}). The CO concentration-time profiles obtained using 10 different [O_2] are shown in Figure VI-3. O_2 was in large excess with respect to HCO with highest expected initial concentrations of $\approx 10^{13}$ cm^{-3}. Under these conditions the kinetic of CO formation can be described by a pseudo-first order kinetics:

$$\frac{d[CO]}{dt} = k[O_2][HCO] = k'[HCO] \qquad \text{VI-6}$$

where k is the rate constant of the HCO + O_2 reaction, and k' = k[O_2] is the pseudo-first order rate constant.

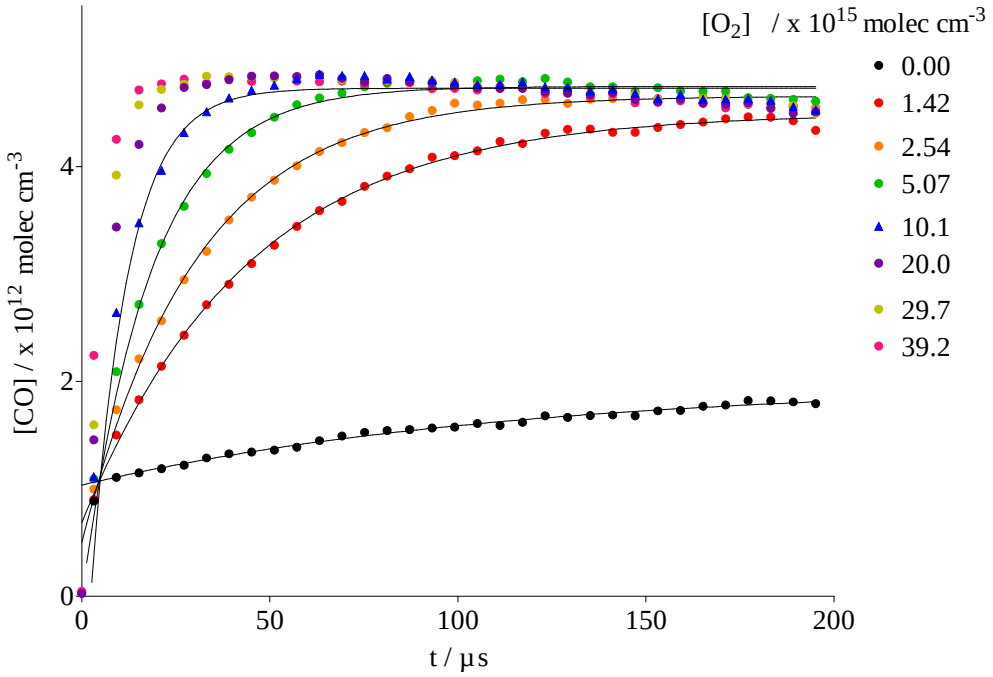

Figure VI-3 HCO + CO kinetic presented as CO signals at variable O_2 concentrations.

The time profiles were fitted to the following equation (VI-7) :

$$[CO] = ([CO]_{direct} + [CO]_{secondary} \times (1 - e^{-k' \times t})) \times e^{-k_{diff} \times t} \qquad \text{VI-7}$$

The results of the fits provided a set of pseudo-first order rate constants k' which were plotted against $[O_2]$ (Figure VI-4). As can be seen, the points are almost perfectly aligned and the slope of the line lead to $k = 5.17\times10^{-12}$ cm^3 molecule^{-1} s^{-1}. The rate constant k available in literature is $k = 5.2\times10^{-12}$ cm^3 molecule^{-1} s^{-1} (NIST ; Atkinson, Baulch et al. 2001). The good agreement confirms that the slow increase of CO is due to the conversion of HCO into CO. In addition, we were not able to distinguish any other way which would have led to CO.

The value obtained from the fit of the CO signal recorded in presence of the O_2 leak (gray dots in Figure VI-2) was k' = 4262 s^{-1}. The oxygen concentration determined from this pseudo-first order rate constant using $k_{HCO+O2} = 5.2\times10^{-12}$ cm^3 molec^{-1} s^{-1} was $[O_2] = 8.2\times10^{14}$ molec cm^{-3}, in good agreement with the estimated leak $[O_2] = 1\times10^{15}$ molec cm^{-3}. The oxygen leak has been taken into account and added to the lowest O_2 concentration presented in Figure VI-4. Using concentrations of O_2 higher than 10^{16} cm^{-3}, this leak could be neglected.

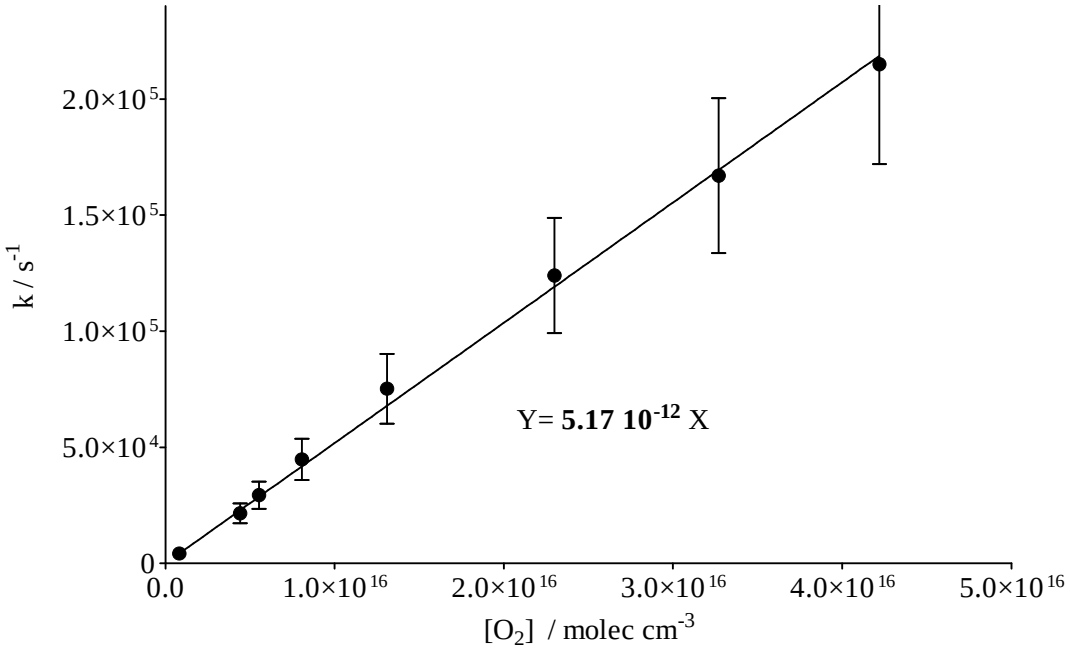

Figure VI-4 : Extrapolation of the rate constant for the reaction of HCO + O_2 obtained from the fit of the CO concentration-time profiles at different $[O_2]$ concentrations, corrected with respect to a leak $[O_2] \approx 10^{15}$ molec cm^{-3} . The result of the linear regression is $Y = 5.17\times10^{-12}$.

VI.5 Determination of the quantum yield of CO by varying the laser fluence

In order to determine the quantum yield of CO, a series of experiments was performed at a given concentration of aldehyde ($[CF_3CH_2CHO] = 3.2\times10^{15}$ molec cm^{-3}) and in presence of a large excess of O_2 ($[O_2] = 4\times10^{16}$ molec cm^{-3}). In this condition the HCO radical will be totally converted into CO and the quantum yield will comprehend (VI-8) the two photolysis pathways:

$$\Phi_{COtot} = \Phi_{HCO} + \Phi_{COdirect} \qquad \text{VI-8}$$

where Φ_{HCO} and $\Phi_{COdirect}$ are respectively the quantum yield of the photoproducts generated in (II-1) and (VI-2).

The fluence was varied by changing the angle of a lame followed by a polarizer. A telescope was used to increase the fluence by a factor of 2 in order to get a better S/N ratio. The CO concentration time profiles obtained this way are shown in Figure VI-5.

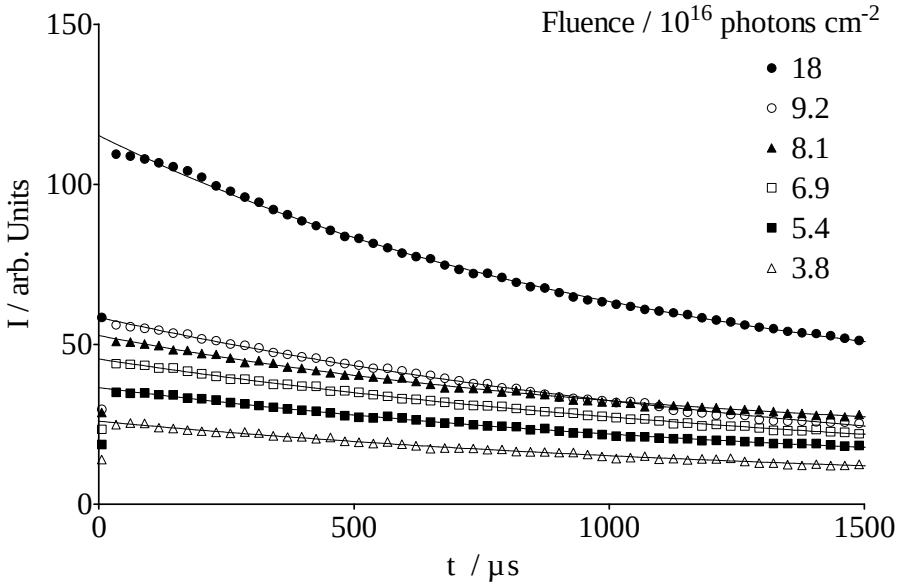

Figure VI-5 Time resolved profiles of [CO] for different laser fluences. The photolysis was performed at 30 Torr in He and the aldehyde concentration was $[CF_3CH_2CHO] = 3.15\times10^{15}$ molec cm^{-3} and in presence of high O_2 concentration $[O_2] = 4.09\times10^{16}$ molec cm^{-3}.

It should be mentioned that the measurement of the fluence using CH_3COBr as an actinometer (see paragraph II.8.2 page 61) was performed just after doing this set of experiments, without modifying the alignment of the IR and UV beams. We remind for convenience that the maximal fluence with the telescope and the polarizer placed in the UV beam was 9.1×10^{16} photons cm^{-2}. The data with a fluence of 18.2×10^{16} photons cm^{-2} was obtained by removing the polarizer. In this series of experiments we were not able to distinguish CO formed directly (VI-5) from that formed by conversion of HCO (VI-4), reason why the profiles were fitted to VI-9:

$$[CO] = [CO]_{tot} \times e^{-k_{diff} \times t} \qquad \text{VI-9}$$

where $[CO]_{tot}$ is the concentration of CO comprising CO formed directly (VI-5) and CO formed from conversion of HCO (VI-4), and k_{diff} is the diffusion rate constant.

The plot of $[CO]_{tot}$ versus the fluence is shown Figure VI-6. The data could be fitted to a line, with the intercept imposed to be zero. From this figure it can be seen that the photodissociation, in our experimental conditions, is consistent with a one-photon process. The slope S of the line is related to the quantum yield by the following relationship (VI-10).

$$\Phi_{COtot} = \frac{Slope}{[CF_3CH_2CHO]\times\sigma_{266}} \qquad \text{VI-10}$$

The quantum yield of production of CO and HCO in the photolysis of CF_3CH_2CHO at 266 nm was found to be $\Phi_{COtot} = 0.48\pm0.07$.

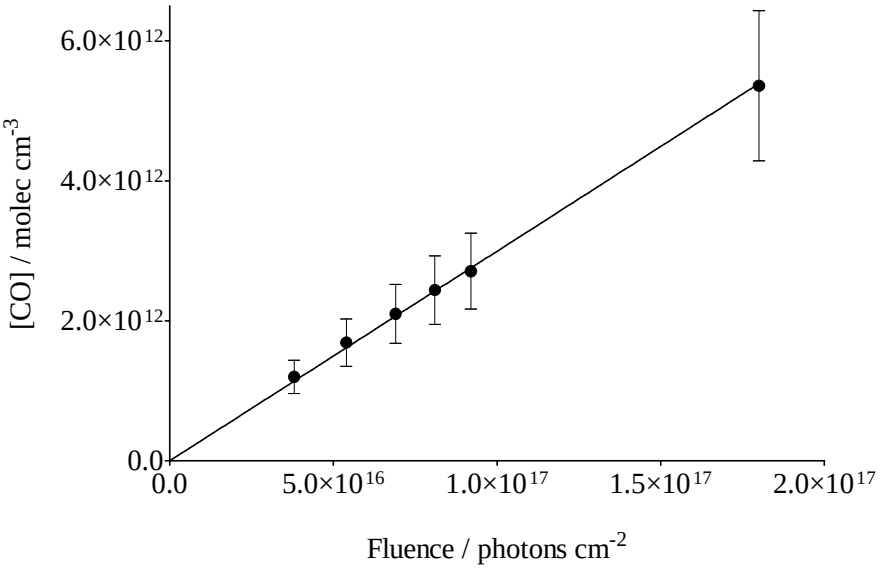

Figure VI-6 CO formed from reaction II-1 and reaction VI-2 in presence of high O_2 concentrations and at laser energies. The result of the linear fit is $Y = 2.99\times10^{-5}$ X.

VI.6 Determination of the quantum yield of direct CO

Using O_2 in large excess, it was impossible to distinguish the formation of direct CO from the conversion of HCO into CO (dark gray trace on Figure VI-2). In order to determine the quantum yield of CO formed directly by pathway VI-2, we photolyzed CF_3CH_2CHO without introducing O_2. There was still a small amount of O_2 due to a leak (see paragraph VI.4 page 112), which explained the slow increase of [CO] due to partial and slow conversion of HCO (VI-4) (Figure VI-7). The [CO] profiles were fitted to equation VI-7, with k_{diff} fixed to 0 (*i.e.* no diffusion was taken into account).

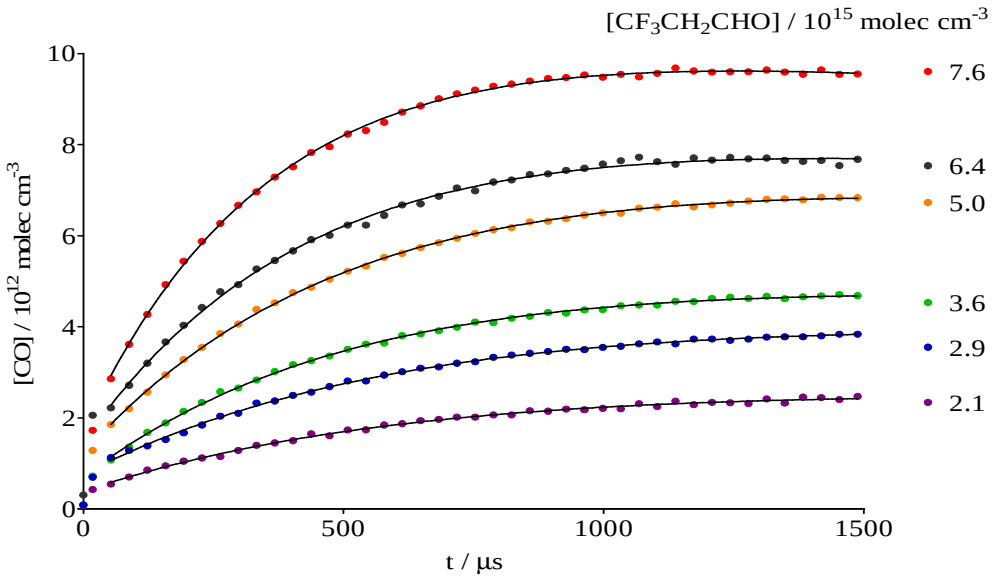

Figure VI-7 Time resolved profiles of [CO] for different aldehyde concentrations. The photolysis was performed at 28 Torr in N_2 and the laser energy was 76 mJ for a repetition rate of 1Hz.

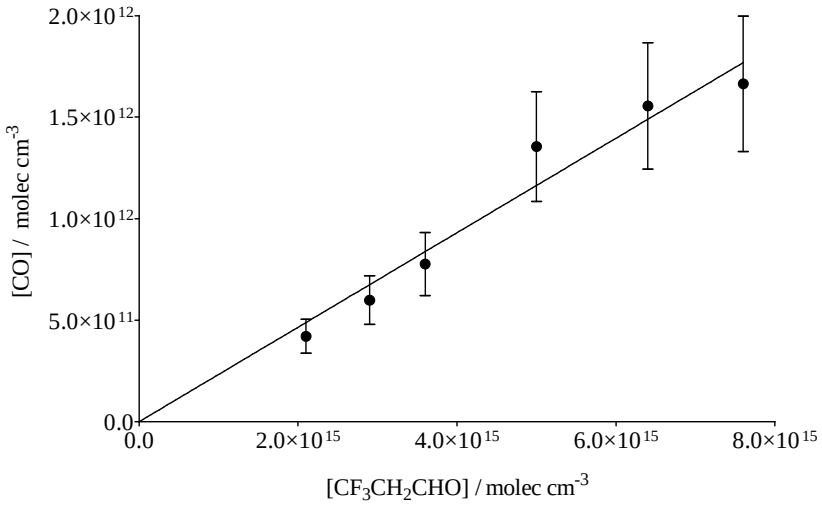

Figure VI-8 CO formed from reaction XI-3 in presence of low O_2 concentrations (leak). The result of the linear fit is Y = 2.3×10^{-4} X.

The plot of $[CO]_{direct}$ against $[CF_3CH_2CHO]$ is displayed Figure VI-8. Once again the quantum yield will be directly related to the slope of the linear regression.

$$\Phi_{COdirect} = \frac{S}{\sigma_{266} \times F} \qquad \text{VI-11}$$

The fluence was 1.1×10^{17} photons cm^{-2} and the quantum yield derived from the slope (Figure VI-8) is then $\Phi_{CO} = 0.11\pm0.02$. This quantum yield represent only the contribution of CO formed by reaction VI-5.

From the quantum yields obtained in presence of high concentration of O_2 and with the leak only it is possible to determine the quantum yield of channel II-1, simply as the difference of the two values (VI-12). Form this calculation we obtain a value of $\Phi_{HCO} = 0.37\pm0.07$.

$$\Phi_{HCO} = \Phi_{COtot} - \Phi_{COdirect} \qquad \text{VI-12}$$

VI.7 CRDS experiments at 248 nm

In the current work of thesis a great help to the interpretation of the mechanism of photo-dissociation has been given by measuring the formation of HO_2 radicals after photolysis of the VOC by Cavity Ring Down Spectroscopy (CRDS) (Thiebaud, Crunaire et al. 2007; Thiebaud, Parker et al. 2008). The choice of the CRDS has been driven by the possibility to convert HCO (II-1) radical and H atoms (VI-2) formed after the aldehyde photolysis into detectable HO_2 (details in the Annex).

These reactions occur with O_2 and can be pushed to the total conversion in presence of an excess of O_2, as it was already seen for the CO detection (paragraph II.7 page 45).

In this experiment different concentrations of aldehyde 3,3,3-trifluoro propionaldehyde have been photolyzed with an excimer laser at 248 nm and the HO_2 originated from the reaction of the photofragments with O_2 have been detected. Signals and calculations are reported in details in Annex CRDS. From these records emerges two different ways of formation. The major HO_2 concentration is formed from the rapid conversion of HCO radical and is characterized by a Φ_{HCO} = 0.51±0.01. The second, clearly less important, is probably due to the reaction of H atoms coming from the single bond breaking in the alpha position of the aldehydic group and was estimated $\Phi_H \approx$ 0.1. This results confirm the pathway of photodissociation (VI-2) corresponding to the CO_{direct} recorded with the TDLAS in absence of O_2.

Both quantum yields obtained by CRDS at 248 nm are in good agreement with the values recorded at 266 nm with the TDLAS, confirming the photolysis pathway proposed.

VI.8 3,3,3-trifluoro propionaldehyde conclusions

With this technique we have been able to distinguish and quantify two ways of photolysis at 266 nm (reaction II-1 and VI-2), in agreement with what has been proposed in literature articles (Sellevåg, Kelly et al. 2004; Chiappero, Malanca et al. 2006; Antiñolo, Jiménez et al. 2011). The photolysis pathway giving birth to HCO (reaction VI-4) has been directly detected from the conversion of this last one into CO by reaction with O_2. From the variation of the O_2 concentration inside the cell the value of the rate constant for the reaction HCO + O_2 has been determined to $k = 5.2\times10^{-12}$ $cm^3 s^{-1}$, in good agreement with the literature value (Atkinson, Baulch et al. 2001). The record of different time resolved signals of CO, formed after photolysis, made accessible also the quantum yield for the direct formation of CO after photodissociation at 266 nm. Value obtained for the direct CO formation after the break of the two bonds in the alpha position (reaction VI-2) is $\Phi_{COdirect}$ = 0.11±0.02. The quantum yield of the HCO radical (reaction II-1) has been shown to be the major pathway of photolysis with a Φ_{HCO} = 0.37±0.07. Ulterior confirmation of the photolysis pathways was given by the CRDS signals. With this thecnique the photofragment HCO and H were detected after conversion into HO_2. The results lead to quantum yield for HCO of Φ_{HCO} = 0.51±0.01 and for H atoms of $\Phi_H \approx 0.1$, in good agreement with the value obtained at 266 nm.

VII. Photolysis of acrolein (CH_2=CHCHO) at 355 nm

VII.1 Previous studies

Propenal (acrolein, CH_2=CHCHO) is found to be a principal component smog of the Los Angeles type (Stephens, Darley et al. 1961). In the troposphere acrolein has been observed at concentrations that can reach 13 ppbv, but the typical levels are much lower and expected to be about 15% of those of formaldehyde observed in urban air masses (Gardner, Sperry et al. 1987). Acrolein is emitted into the atmosphere by different sources such as combustion and chemical industries. It is also used in a number of agricultural chemicals and released to the atmosphere from the combustion of wood, polymers, tobacco, and gasoline. Like other carbonyl compounds, acrolein is subjected to reactions with the OH radical and photolysis.

The reaction of acrolein with the OH radical was studied by Magneron et al. in 2002 (Magneron, Thévenet et al. 2002) in the temperature range 243 – 372 K. The reaction proceeds by addition of OH to the double bond (35 %) or by abstraction of the aldehydic hydrogen (65 %). They were able to derive an Arrhenius expression (III-1) which showed negative temperature dependence:

$$k_{OH} = (6.55 \pm 1.22) \times 10^{-12} \times e^{\frac{333 \pm 54}{T}} \qquad \text{VII-1}$$

At room temperature, the rate constant determined using equation III-1 is $k_{OH} = (1.99 \pm 0.24) \times 10^{-11}$ cm^3 $molec^{-1}$ s^{-1}. Magneron et al. also studied the photolysis of acrolein in the simulation chamber EUPHORE. They were not able to observe any photolysis product by FTIR spectroscopy and they concluded that the photolysis quantum yield of acrolein was below 0.005. The predominant sink of acrolein in the atmosphere is then oxidation initiated by the OH radical.

The UV spectrum of acrolein, shown in Figure III-1, was recorded by Magneron et al. in 2002 (Magneron, Thévenet et al. 2002) over the wavelength range 220 – 400 nm, in static conditions at 298 K from 0.02 to 10 Torr. The spectrum exhibits a broad band between 250 and 400 nm assigned to the $n \rightarrow \pi^*$ transition. The S_1 and T_1 states lays, respectively 298 kJ mol^{-1} and 278 kJ mol^{-1}, above the ground state S_0. In this study, the cross section was measured at 354 nm and 356 nm, the values being respectively 4.18 and 3.63×10^{-20} cm^2. At 355 nm, it seems reasonable to use $\sigma_{355} = 3.9 \times 10^{-20}$ cm^2.

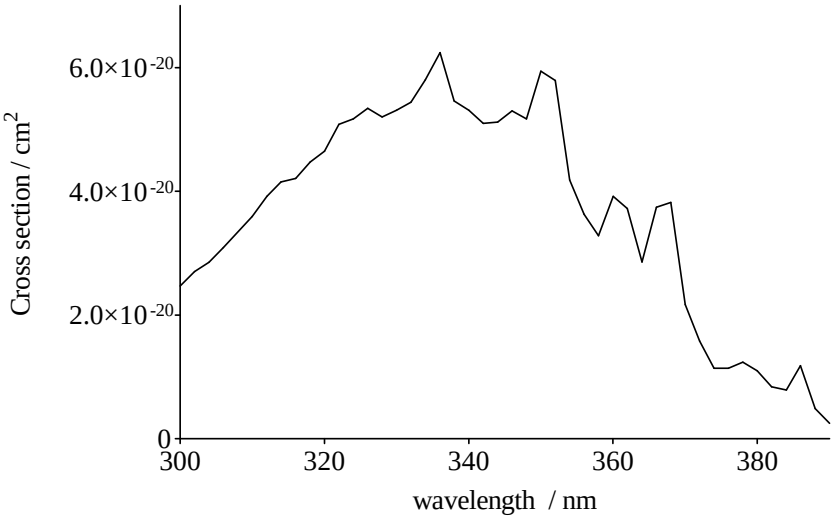

Figure VII-1 Absorption cross section of acrolein at 298 K (Magneron, Thévenet et al. 2002).

Gardner et al. (Gardner, Sperry et al. 1987) studied the photolysis of acrolein at 313 nm and 298 K in conditions close to the tropospheric ones, *i.e.* in presence of oxygen. They proposed the following scheme to explain their results:

$$CH_2=CHCHO + h\nu \rightarrow (S1) \qquad \text{VII-2}$$

$$S_1 (+M) \rightarrow T_1 (+M) \qquad \text{VII-3}$$

$$T_1 + (O_2 \text{ or } N_2) \rightarrow S_0 + (O_2 \text{ or } N_2) \qquad \text{VII-4}$$

$$S_1 \text{ or } T_1 \rightarrow CO + C_2H_4 \qquad \text{VII-5}$$

$$S_1 \text{ or } T_1 \rightarrow CH_3CH \text{ (singlet)} + CO \qquad \text{VII-6}$$

$$S_1 \text{ or } T_1 \rightarrow CH_3CH \text{ (triplet)} + CO \qquad \text{VII-7}$$

$$S_1 \text{ or } T_1 \rightarrow CH_2=CH + HCO \qquad \text{VII-8}$$

$$S_1 \text{ or } T_1 \rightarrow CH_2=CHCO + H \qquad \text{VII-9}$$

Channels VII-5 to VII-7 are molecular channels which are decarbonylations. The second channel (VII-8) is a C-C cleavage which is a Norrish type I mechanism. The last channel (VII-9) leads to radical products resulting of a C-H α cleavage. The minimum excitation energy required for acrolein decomposition by processes VII-5 to VII-9 are respectively 17, 414, 343, 305 and 364 kJ mol^{-1} [(Gardner, Sperry et al. 1987) and references cited therein]. We remind for convenience that

313 and 355 nm corresponds respectively to 382 kJ mol^{-1} and 337 kJ mol^{-1}. Fang (Fang 1999) performed detailed *ab initio* calculations on the three photodissociation pathways. The potential energy profiles he derived are gathered in Figure VII-2 (with the original energies given in kcal mol^{-1} converted in kJ mol^{-1}). At 313 or 355 nm, acrolein can be excited to the S_1 state, which lays 298 kJ mol^{-1} above the ground state.

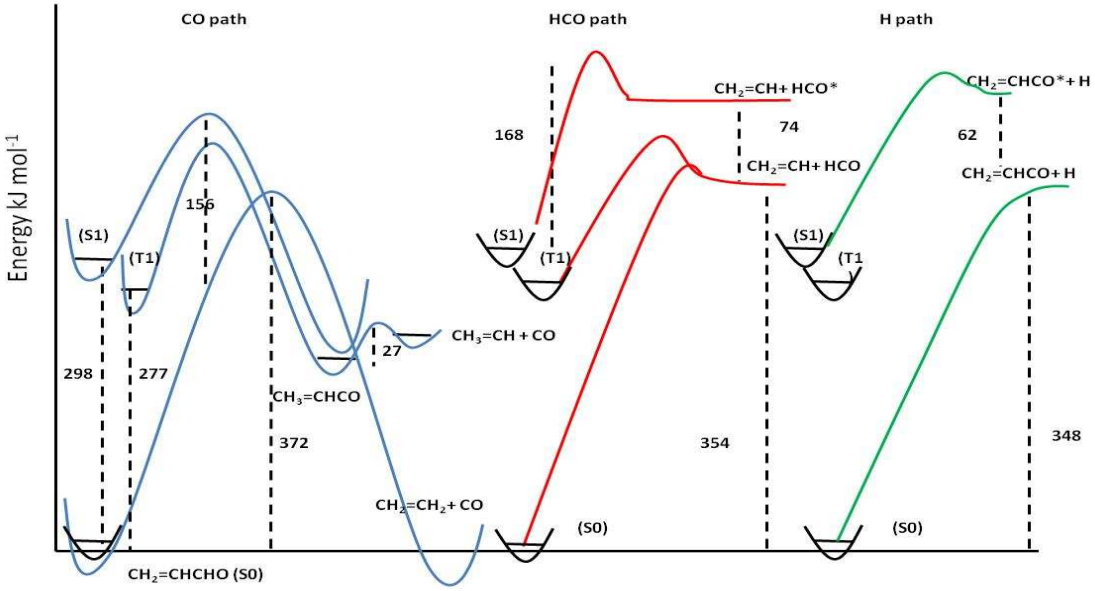

Figure VII-2 Schematic potential energy profiles of the CH_2CHCHO dissociation, with distinction of the three different paths (adapted from (Umstead, Shortridge et al. 1978; Fang 1999)).

From the S_1 state, acrolein can evolve according to three main pathways:

- Decarbonylation (see profiles at left in Figure VII-2): Fang showed that decarbonylation through channels VII-6 and VII-7 involves a two-step mechanism. The first step is an exothermic isomerization of acrolein to methylketene CH_3CHCO which implies a migration of the aldehydic hydrogen to the terminal carbon highly favored in the twisted geometry of the T_1 state rather than in the planar geometry of the S_1 state. Intersystem crossing is known to be efficient between the S_1 and T_1 states. From the T_1 state, the barrier to isomerization was determined to be 156 kJ mol^{-1}. The saddle point lays 207 kJ mol^{-1} above the ground state. Decarbonylation then takes place through a small barrier of 27 kJ mol^{-1}. Due to the high barrier to overcome for the isomerization, this channel should not operate at 313 nm or at 355 nm. In fact, the main pathway of photodissociation leading to C_2H_4 and CO is probably nonadiabatic, *i.e.* it proceeds on the ground state surface. This decarbonylation is slightly exothermic and the barrier height to dissociation is at least of 355 kJ mol^{-1}. If we take into account the energy carried by acrolein at room temperature (≈ 295 K) which can be

estimated to 20 kJ mol^{-1}, dissociation following this pathway is possible when acrolein absorbs 355 nm-photons, but we are just at the threshold.

- Norrish type-I mechanism (see profiles in the middle in Figure VII-2) : an intersystem crossing from S_1 populates the T_1 state. Dissociation into CH_2CH and HCO occurs through a barrier of 130 kJ mol^{-1}.
- C-H cleavage (see profiles at right in Figure VII-2): the reaction is endothermic by 354 kJ mol^{-1}. It may proceed from the S_1 or T_1 states, but it is likely to occur on the ground state surface after relaxation via the S_0/S_1 intersection point.

In their paper, Gardner et al (Gardner, Sperry et al. 1987) found evidence that all the channels should be taken into account to explain their results at 313 nm. The main products they detected were CO and C_2H_4, their quantum yield being respectively at 26 Torr 0.07 and 0.05. At high pressure, close to the atmospheric one, these quantum yields decreased, being respectively 0.005 and 0.002. The quantum yield for the acrolein loss was 0.08 at 26 Torr and 0.0065 at atmospheric pressure. They also detected formaldehyde H_2CO, methanol CH_3OH and glyoxal $(HCO)_2$. The vinyl radical produced in channel VII-8 was believed to yield glyoxal and formaldehyde by reaction with O_2. They showed that the formation of CH_3CH through the channels VII-6 and VII-7 was necessary to rationalize their experimental observation. According to them, at low pressures of O_2, 73 % of the CH_3H rearranged to C_2H_4 while the remaining reacted with O_2. At atmospheric pressure, reaction with O_2 was predominant.

VII.2 Experimental details.

Acrolein (Sigma Aldrich reagent 90% purity) has been introduced in the reaction cell with the bubbler system (paragraph II.5.2 page 41) thermostated at 25°C. The suitable concentration for the analysis has been achieved adding a dilution flux of an inert gas: N_2 or He. Due to the expected low quantum yield, the photolysis was performed at 355 nm, near the maximum of absorption. Analyses were performed at room temperature varying the aldehyde concentration in the range 1.2 - 1.7 × 10^{17} molec cm^{-3} at a pressure close to 30 Torr. The photolysis has been performed at 355 nm to reach the maximum of absorption possible. A flow of pure O_2 (AirLiquid products 99% purity) was added to the mixture to convert HCO radical into detectable CO reaction VII-10. The flow was varied to achieve O_2 concentrations between 1×10^{15} and 1.6×10^{17} molec cm^{-3}.

$$HCO + O_2 \rightarrow HO_2 + CO \qquad \text{VII-10}$$

VII.3 Photolysis signals

The photolysis of acrolein was studied in presence of oxygen in low or high concentration. We first present the photolysis of acrolein without added O_2 or with a low concentration of O_2, followed by the results obtained with a high concentration of O_2.

VII.3.1 CO profiles without O_2

The [CO] signals originated from the photolysis at 355 nm of different acrolein concentrations in He as the bath gas are presented in Figure VII-3. In these records we observe two different components of CO: one formed in the first microseconds, called CO_{direct}, and a second one appearing at longer reaction time called CO_{slow}, the maximum being reached at ≈ 250 µs. Diffusion of CO out the photolyse beam cylinder constitutes the last part of the time profile.

The curves were fitted using equation :

$$[CO] = \left([CO]_{direct} + [CO]_{slow} \times \left(1 - e^{-k \cdot t}\right)\right) \times \left(e^{-k_{diff} \cdot t}\right) \qquad \text{VII-11}$$

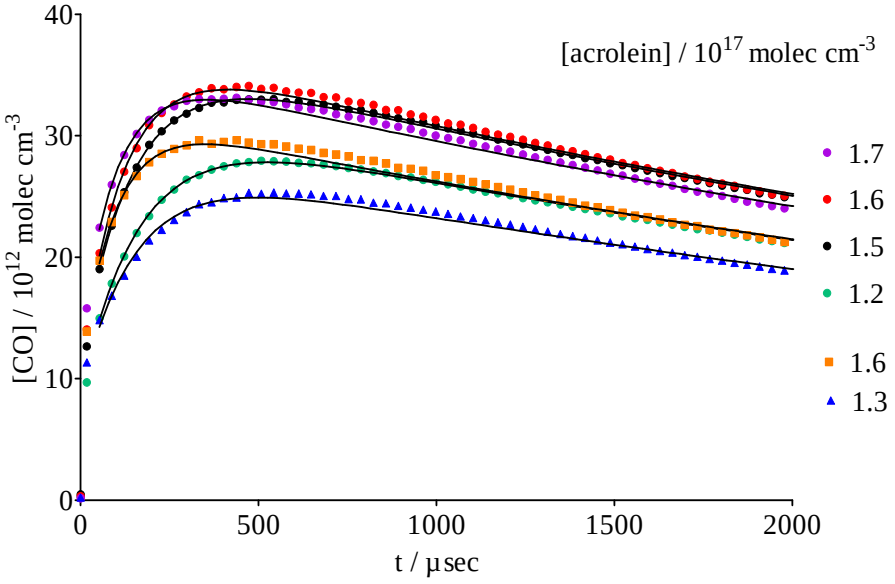

Figure VII-3 Time resolved kinetic signals of the [CO] in the photolysis of different acrolein concentrations, without added O_2 (O_2 was nevertheless present in the cell due to a leak, see text). The photolysis was performed in 33 Torr of He and the laser energy was 113 mJ pulse^{-1} for a repetition rate of 5Hz.

In Figure VII-3 the CO signals presented are proportional to the concentration of the acrolein introduced in the cell. A brief observation should be made on the signals at 1.3×10^{17} molec cm^{-3} (orange squares) and at 1.6×10^{17} molec cm^{-3} (blue triangles) that present a CO_{slow} component lower than expected. The concentration of acrolein was too close and small variations in the bubbler (temperature of the liquid, pressure) might have affected them. Even with this difference, the two components: CO_{direct} and CO_{slow} are still linear with the VOC concentration introduced in the cell (Figure VII-4). The variation of the CO_{slow} previously detected is enlightened also in the high dispersion of the points (squares) representing the results of the fits of the CO profiles.

The second component (CO_{slow}) is hardly explainable with the model proposed in literature because the only reported pathway of CO formation is the decomposition of the CH_2=CHCO* radical. If we assume that the lifetime of the CH_2=CHCO* radical is comparable (of the same order of magnitude) with that one of the CH_3CO* radical estimated to be lower than to 100 ns (Somnitz, Fida et al. 2005; Rajakumar, Gierczak et al. 2008) it results that no other pathway of CO formation is possible. This CO_{slow}, appearing at longer reaction time, is in fact suspected to come from the relaxation of CO in the upper vibrational excited states. Confirmations of the presence of upper vibrational states (CO v=1,2) relaxing and populating the fundamental one will be reported in paragraph VII.4 page 126.

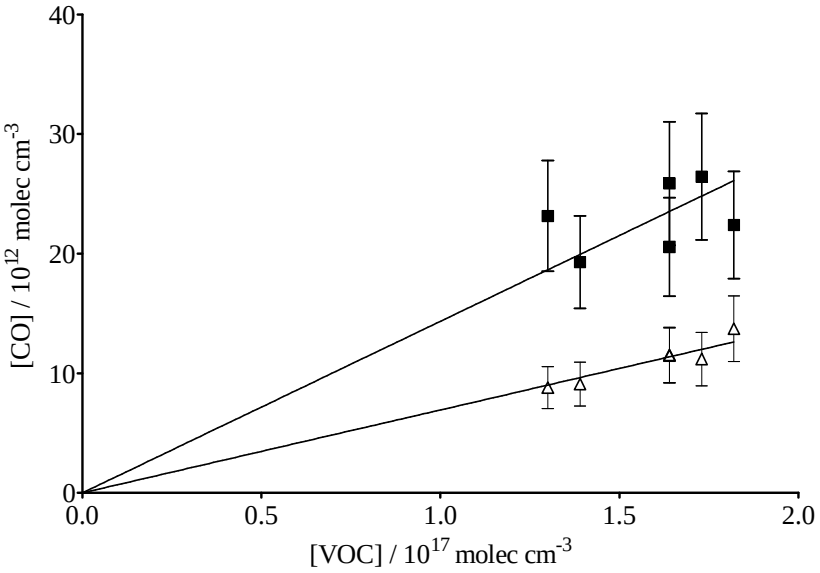

Figure VII-4 Linear relation occurring between the CO formed from the relaxation of the upper vibrational excited states (■) and CO formed directly (Δ) versus the acrolein concentrations.

VII.3.2 CO profiles with high O_2 concentrations

The addition of high O_2 concentrations ($[O_2] > 2.6 \times 10^{16}$ molec cm^{-3}) totally converted HCO into CO in almost 7 µs, which was too fast to be time-resolved by our set-up. In this way, the HCO radical was detected after the laser pulse together with CO formed directly and the kinetic part which remained in the time-profiles was due to other processes than the HCO + O_2 reaction.

In Figure VII-5 are reported CO profiles at high O_2 concentrations, together with a signal recorded without O_2 to emphasize the difference. In the case of the CO profiles recorded at high O_2 concentrations, we still found a CO_{slow} component. This component, that is neither the HCO conversion nor the decomposition of the CH_2=CHCO* radical is a first proof of the presence of vibrational excited states of CO.

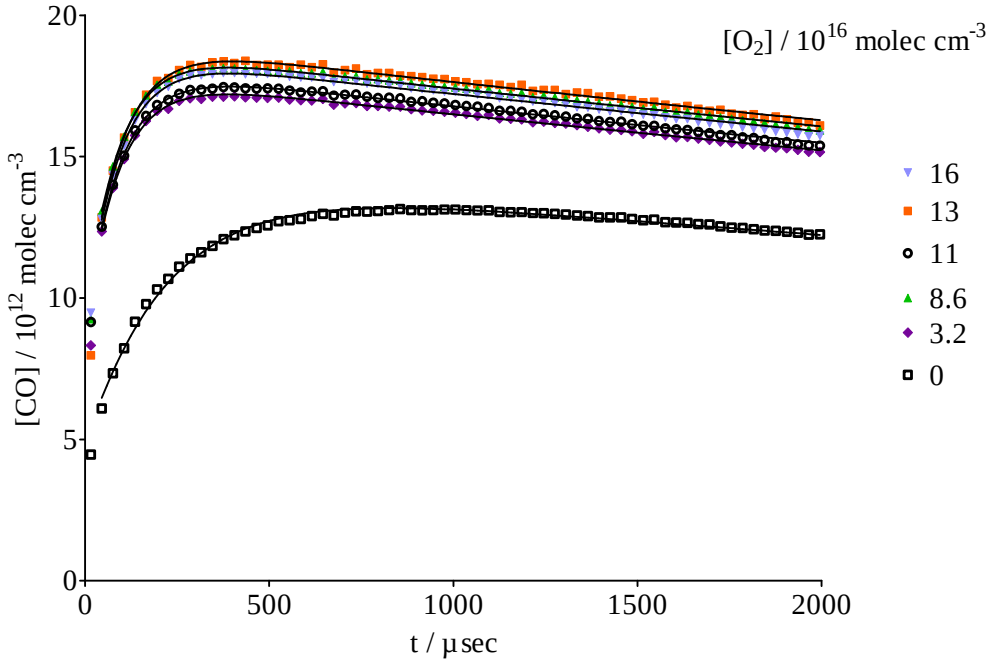

Figure VII-5 Time resolved kinetic signals of the [CO] in presence of high concentrations of oxygen, [CH_2=CHCHO] = 8.0 – 9.8 × 10^{16} molec cm^{-3}. The photolysis was performed at 35 Torr in N_2 and the laser energy was 94 mJ $pulse^{-1}$ for a repetition rate of 5Hz. Rate constant for the profile obtained without O_2 is 5347 s^{-1}, and it is 10 600 s^{-1} for the other profiles.

VII.4 Excited states

Introducing the paragraph on the excited states is important to remember that the energy of a 355 nm photon is not sufficient to create CO in the vibrational state. The energy threshold for the CO formation extracted from Figure VII-2 is 298 kJ mol^{-1} while the 355 nm photons have 337 kJ mol^{-1}; as a consequence the excess energy is 39 kJ mol^{-1}. From this energy should be subtracted of the roto-vibrational energy of each fragment to obtain the disposable energy for CO. Knowing that CO needs ≈ 25 kJ mol^{-1} for each quantum of vibrational excitation, even considering the entire amount of exceeding energy we will not be able to produce CO v=2 (Figure VII-6).

In the previous paragraph (VII.3.1 page 5) we presented the hypothesis on the origin of the CO_{slow}: the relaxation of the excited vibrational states. A first confirmation was given adding high O_2 concentration to exclude reaction XII-8, but the definitive proof to this hypothesis was given by the direct detection and record of CO v=1,2 time resolved signals. Profiles of the CO in the fundamental state and excited vibrational states v=1,2 have been recorded in a single day of analysis at same acrolein concentration and photolysis conditions (Figure VII-6). The shape of the CO v=1 signal corresponds to the fundamental one CO v=0: a rapid rise immediately after the photolysis pulse (CO_{direct}) is followed by an exponential kinetic (CO_{slow}). The CO v=2 signal is too low to identify a secondary formation. The CO profiles were fitted to extract the pseudo first order kinetic constant and to verify if the slow rise in CO v=0 can correspond to the relaxation of the excited state CO v=1. Form Figure VII-6 CO v=0 formation results k = 8337 s^{-1}, in pretty good correspondence with the k = 7661 s^{-1} of the CO v=1 excited state relaxation. Seen the difficulty encountered in the simple record of the CO excited state signal the simple information extracted from the CO v=2 was the presence of CO in such vibrational state.

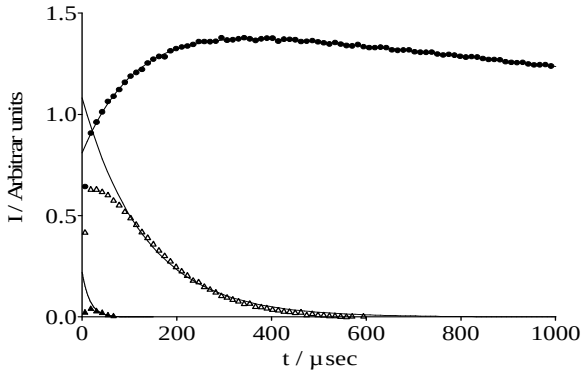

Figure VII-6 [CO] signals recorded for different vibrational states en He for a concentration of [CH_2CHCHO] = 4 × 10^{16} molec cm^{-3}. CO v=0 (•), CO v=1 (Δ), CO v=2 (▲). The photolysis was performed at 30 Torr and the laser energy was 94 mJ for a repetition rate of 5Hz.

The detection of the upper vibrational states of CO can be confirmed also with the study on the dependence of the pseudo first order rate constant (k) with the acrolein concentrations (Figure VII-7). In fact the CO formed in the upper vibrational states can relax by collision with acrolein itself other than the buffer-dilution gas (He or N_2) and O_2. Seen that the collision in He are less efficient that in N_2 the effect on the relaxation induced by the acrolein will be more effective in He then in N_2. In Figure VII-7 are presented the results of different rate constant (k in s^{-1}) versus the acrolein concentration in two buffer gas (He and N_2).

It is possible to note that in He there is an evident dependence of the relaxation with the concentration of acrolein. The slope of the linear regression gives $k = 4.78 \times 10^{-14}$ cm^3 $molec^{-1}$ s^{-1}. This value is in agreement with the rate constant $k = 4.43 \times 10^{-14}$ cm^3 $molec^{-1}$ s^{-1} proposed in literature for propynal by Chowdhury (Chowdhury 2003).

In Figure VII-7, the relaxation by N_2 can be extrapolated from the non null intercept of our regression ($Y_0 = 1626$ s^{-1}). With this value and a N_2 concentration $[N_2] = 1.2 \times 10^{18}$ molec cm^{-3}, we determined the rate constant to be $k = 1.35 \times 10^{-15}$ cm^3 $molec^{-1}$ s^{-1}. In literature Stephenson (Stephenson 1973) indicated that the rate constant of the relaxation of CO v = 1 driven by N_2 is $k = 5.09 \times 10^{-15}$ cm^3 $molec^{-1}$ s^{-1}. Even if the points for N_2 are concentrated on a small [VOC] range, we tried to apply a linear regression in order to check if acrolein plays a role on the relaxation on the CO vibrational excited state also in N_2. The slope of the fit is $k = 4.02 \times 10^{-14}$ cm^3 $molec^{-1}$ s^{-1}, which is the expected rate constant. From these observations we concluded that in N_2, both the bath gas and acrolein participate to the CO relaxation, while in He it depends mainly of the concentration of acrolein.

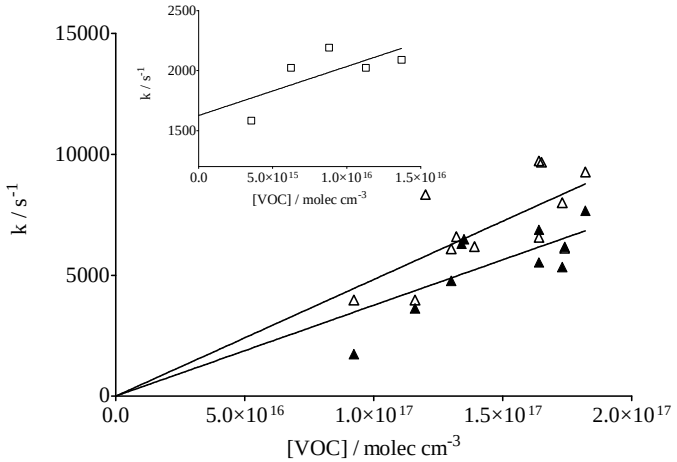

Figure VII-7 Pseudo first order kinetic constant of the CO v=0 formation (Δ), CO v=1 relaxation (▲), recorded for different concentrations of acrolein in He. (□) represent the CO v=0 formation in N_2.

VII.5 VII.4 Results

The CO formed in the acrolein photolysis at 355 nm, as described by equation VII-12, depends on the absorption cross section, on the laser fluence and on the quantum yield parameter (Φ).

$$[CO] = \Phi \times \{[CH_2 = CHCHO] \times F_{355} \times \sigma_{355}\} \qquad \text{VII-12}$$

The CO quantum yield of the photolysis process can be determined from the plot of the measured CO concentrations versus ([CH_2=CHCHO] x F_{355} x σ_{355}) as the slope of the linear regression. In absence of O_2 the component called CO_{direct} (Figure VII-3) was extracted from the regression of Figure VII-8 were the quantum yield was found to be Φ_{CO} =0.006±0.001. This component was originated by reactions from VII-5 to VII-7. In presence of high O_2 concentrations instead the component called CO_{direct} is comprehensive of two photolysis pathways: the CO formed by reactions from VII-5to VII-7and also reaction VII-8, where the HCO converted into detectable CO by reaction VII-10. As explained in the previous paragraphs the CO_{slow} represents the relaxation of the CO vibrational excited states into the fundamental one.

From the linear regression of Figure VII-9 we obtain values for the quantum yields that are respectively: $\Phi_{HCO + CO}$=0.013±0.002 and $\Phi_{CO\ slow}$ =0.013±0.002. For CO, the total quantum yield value (Φ_{COtot}) determined for the acrolein photolysis at 355 nm in presence of high O_2 concentrations is then estimated as the sum of the two components:

$$\Phi_{COtot \cdot withO_2} = \Phi_{HCO+CO} + \Phi_{COslow} = 0.013 + 0.013 = 0.026 \qquad \text{VII-13}$$

As a consequence the HCO quantum yield Φ_{HCO} can be determined as the direct substraction of the Φ_{HCO+CO} (Figure VII-9) in presence of high oxygen concentration and Φ_{CO} with low oxygen concentration (already evaluated in Figure VII-8) and is determined in equation VII-14:

$$\Phi_{HCO} = \Phi_{HCO+CO} - \Phi_{CO\ direct} = 0.013 - 0.006 = 0.007 \qquad \text{VII-14}$$

Form Figure VII-9 we can observe that in the current experiments no difference was found in the $\Phi_{CO\ slow}$ in two different buffer gas (N_2 and He). This experimental evidence is probably caused by a high efficient relaxation CO/acrolein due to the high aldehyde concentration in the cell ([acrolein] ≈ 10^{17} molec cm^{-3}).

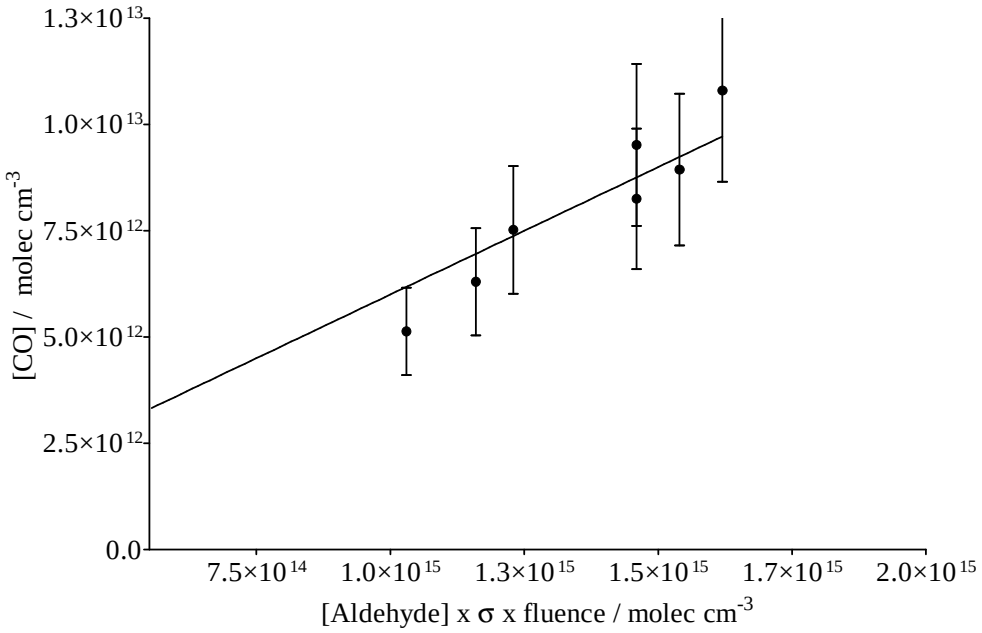

Figure VII-8 Linear relation occurring between the different CO_{direct} (•) and the acrolein concentrations introduced multiplied by the absorption cross section and the fluence. The result of the fit is Y=0.006 X.

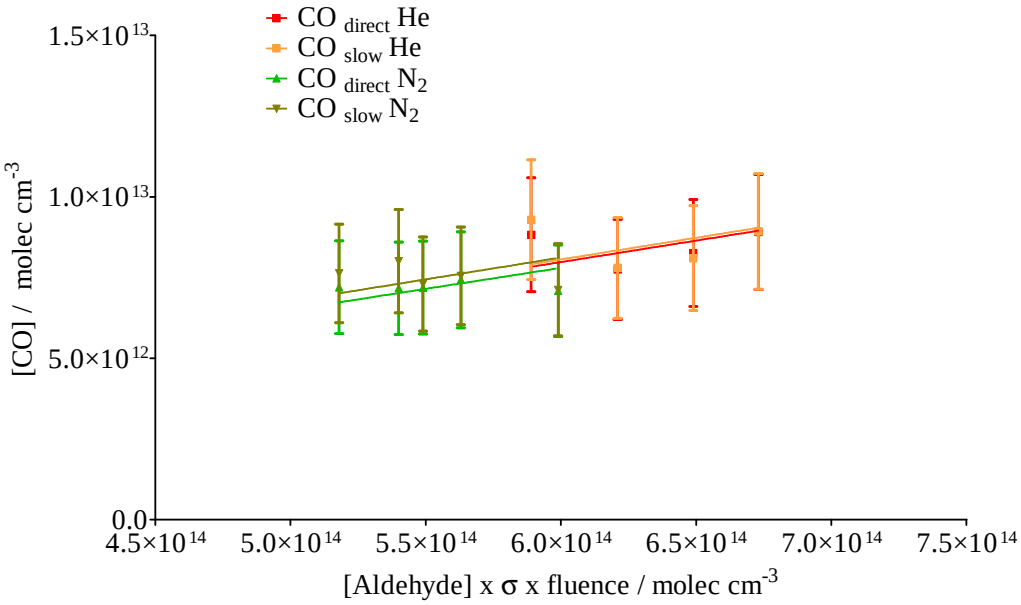

Figure VII-9 Linear relation occurring between the different component of CO formed in the photolysis process of acrolein in two different gas N_2 (green triangles) and He (red and orange squares). Clear circle represent the outliers. In He is presented CO_{direct} (clear green triangles) and CO_{slow} (dark green triangles). In N_2 is presented CO_{direct}(red squares) and CO_{slow} (orange squares).

VII.6 CRDS experiments at 248 nm

In the current work of thesis a great help to the interpretation of the mechanism of photo-dissociation has been given by the measure of the HO_2 radicals formed after photolysis by Cavity Ring Down Spectroscopy (CRDS) (Thiebaud, Crunaire et al. 2007; Thiebaud, Parker et al. 2008). The choice of the CRDS has been driven by the possibility to convert HCO (VII-8) radical and H atoms (VII-9) formed after the aldehyde photolysis into detectable HO_2 (details in the Annex A.2 page 136). These reactions occur with O_2 and can be pushed to the total conversion in presence of an excess of O_2, as it was already seen for the CO detection.

In this experiment different concentrations of acrolein have been photolyzed with an excimer laser at 248 nm. Signals and calculations are reported in details in Annex CRDS A.4.2 (page 142). The formation of HO_2 in the photolysis of acrolein at 248 nm seems to be composed by a single pathway. The HO_2 recorded came from the HCO conversion and no evidence of HO_2 coming from the H atom were detected, probably because of a too large time scale. The quantum yield associated to the photolysis pathway VII-8 is $\Phi_{HCO} = 0.028 \pm 0.001$. This quantum yields obtained by CRDS at 248 nm is in good agreement with the values recorded at 266 nm with the TDLAS, confirming the photolysis pathway proposed.

VII.7 Acrolein conclusions

It has been possible to distinguish and quantify two photolysis pathways of acrolein photolysis at 355 nm: the CO direct formation as presented in reactions from VII-5 to VII-7 and the HCO radical formation (reaction VII-8) in agreement with the model proposed in literature (Gardner, Sperry et al. 1987; Jen and Chen 1999). The photolysis pathway giving birth to HCO VII-8 has been directly detected from the conversion of this last one into CO by reaction with high O_2 concentrations ($[O_2] \approx 1 \times 10^{17}$ molec cm^{-3}). Values obtained for the direct CO formation for the photodissociation at 355 nm are $\Phi_{CO} = 0.006 \pm 0.001$, while the dissociation yield of the HCO radical has been proved to be the more important and defined with a $\Phi_{HCO} = 0.007 \pm 0.002$.

It has been proved that the CO_{slow} component is originated from the relaxation of the upper vibrational excited states of CO, that have been directly detected up to a state v=2 in He. It has been reported a correspondence within the CO v=0 pseudo rate constant formation and the pseudo rate constant relaxation of the vibrational state CO v=1. Both in He and in N_2 gas acrolein play a relevant role in the relaxation of the vibrational states with an associated $k = 4.02 \times 10^{-14}$ cm^3 $molec^{-1}$ s^{-1}.

VIII. Conclusions and perspectives

This work deals with the determination of quantum yields of photolysis of ketones and aldehydes produced by oxidation of isoprene, which is the most abundant hydrocarbon emitted, in the atmosphere by trees. The molecules we have studied are acetone, hydroxyacetone, methylvinylketone and acrolein.

Nowadays in the domain of the atmospheric chemistry, lots of studies have been performed on the theme of the degradation of volatile organic compounds and on their effect on the environment. Those studies approach the subject both in the theoretical and in the experimental ways, permitting the scientific community to have a global vision on the complex dynamics of the atmospheric reactivity. The present work finds its place in the experimental collection of data about the photolysis processes of volatile organic compounds. The experiments were performed with a double goal: to better understand the atmospheric fate of pollutants and radicals, produced from their degradation in the atmosphere, and to enlarge the databases of atmospheric processes, to furnish solid bases for further work on climate and pollutants modeling.

The lifetime of volatile organic compounds is principally limited by reaction with oxidants (O_2, O_3, NO_x) and by reaction with the radical OH. Though, for particular class of molecules like ketones and aldehydes photolysis has a significant part, especially in the UV region.

The experimental set-up used in this work was composed of a UV laser photolyse beam coupled to an IR spectrometer for detection of CO around 2200 cm^{-1} and H_2CO around 2800 cm^{-1}. The temporal resolution of the detection is of the order of 1μs. This set-up allows recording time-profiles of photofragments (CO or H_2CO in our case) during the first milliseconds after photolysis, *i.e.* before secondary reactions take place.

In the course of this study different VOCs have been photolysed at 266 nm or 355 nm. The conclusions obtained for three ketones (acetone, hydroxyacetone and methylvinylketone) and two aldehydes (3,3,3-trifluoro propionaldheyde and acrolein) are listed molecule by molecule in the following. The reader should refer to each chapter to find the corresponding references.

- Acetone

Acetone has been chosen as a reference for the other studies, since its photolysis was already well documented. The time-profiles of CO were made of an instantaneous rise of CO assigned to the dissociation of hot acetyl radicals and by CO appearing from a secondary kinetic during the first millisecond. We did not find any set of secondary reactions which could have given CO with such a kinetics. We then assigned this second rise of CO to relaxation from vibrational excited states, which was confirmed by the direct detection of CO in the vibrational state v = 1 and v= 2. For each component we have determined the quantum yield at 266 nm, estimated to be $\Phi_{CO\ direct}$ =0.11 ± 0.02 for CO formed immediately after the laser pulse and $\Phi_{CO\ slow}$ = 0.29 ± 0.04 for the CO appearing later in the kinetic. Finally the determined total quantum yield is $\Phi_{CO\ tot}$ =0.40±0.04, in agreement with the values proposed by Somnitz and Khamaganov (Somnitz, Fida et al. 2005; Khamaganov, Karunanandan et al. 2007).

- Hydroxyacetone

The time-profiles we have recorded during the photolysis of hydroxyacetone at 266 nm had the same shape of those of acetone previously described. Once again, for each dissociations pathway we have determined the quantum yield at 266 nm. The total quantum yield is estimated to be $\Phi_{CO\ tot}$ = 0.23 ± 0.02. CO formed immediately is considered to be the predominant pathway at 266 nm with $\Phi_{CO\ direct}$ = 0.15±0.02 while the quantum yield for the CO appearing later, in the kinetic, is defined by $\Phi_{CO\ slow}$ = 0.08 ± 0.01. The behaviour of CO in the upper vibrational excited states have been studied in two different buffer gas He (CO v=1, 2, 3) and N_2 (limited at CO v=1). The excitation of CO in the vibrational states can be hardly explained with the absorption of only one photon. The dependence of CO in the v = 1 state against the fluence showed that it was produced from a two-photons absorption process. Together with CO we detected CH_2OH through its conversion into H_2CO in presence of O_2. Its quantum yield estimation gave a value of Φ_{H2CO} = 0.25 ± 0.04. In fact the difference between the Φ_{H2CO} and the Φ_{COtot} can represent the fraction of CH_3CO^* dissociating into CO. From our results we estimate the ratio $CH_3CO^*_{dissociated}/CH_3CO^*_{stabilized}$ to be 0.08 in agreement with the value proposed by Rajakumar (Rajakumar, Gierczak et al. 2008).

- Methyl vinyl ketone

The photolysis of methyl vinyl ketone has been performed at 355 nm. As for the other two ketones, the presence of CO formed immediately after the laser pulse has been observed. We have determined the total quantum yield for the methyl vinyl ketone photolysis $\Phi_{CO\ tot}$ =0.023 ± 0.003, in agreement with the values of Raber and Moortgat. There was still a kinetic component in the time

profile of CO, but it was weaker than the one of acetone and hydroxyacetone ($\Phi_{COdirect}$ =0.016 ±0.002 and Φ_{COslow} = 0.008 ± 0.001)

- 3,3,3-trifluoro propionaldehyde

Using the TDLAS experiment, we were able to distinguish two channels of dissociation of the 3,3,3-trifluoropropionaldehyde at 266 nm. In presence of low O_2 concentrations, a small instantaneous increase of CO was observed, which is a first channel leading to trifluoroethane and CO. This fast increase was followed by a kinetic corresponding to the conversion of HCO with O_2, which was confirmed by the study of the kinetic using different concentrations of O_2. The quantum yield value obtained for the direct CO formation is $\Phi_{COdirect}$ = 0.10 ± 0.02 while the photodissociation yield of the HCO radical is Φ_{HCO} = 0.37 ± 0.07. The Norrish type I α cleavage is then the predominant way of photolysis. The third channel, which gives H atom and a carboxy radical, was investigated by CRDS at a sligthly different wavelength (248 nm).

- Acrolein

Acrolein has been photolysed at 355 nm. As for 3,3,3-trifluoro propionaldehyde, it has been possible to distinguish and quantify two ways of photolysis: that one generating CO direct after the laser pulse and the HCO radical. The quantum yield values obtained for the direct CO formation is $\Phi_{CO\ direct}$ =0.006±0.001, while the dissociation yield of the HCO radical is Φ_{HCO} = 0.007 ± 0.002 proving that it is the major photodissociaton pathway. It has been proved also that the CO_{slow} component is originated from the relaxation of the upper vibrational excited states of CO, that have been directly detected (on a ms time scale) up to a state v = 2 in He.

- CRDS

It should be noted that photolysis was carried out at 248 nm. A comparative study with the Cavity Ring Down Spectroscopy (CRDS) has been performed in collaboration with Chaithanya Jain, member of the group “homogeneous and heterogeneous atmospheric chemistry” directed by Christa Fittschen. These experiments confirmed the interpretations proposed in this work for the photolysis of the aldehydes. From the records made on the 3,3,3-trifluoro propionaldheyde we confirmed the H and HCO formation after photodissociation at 248 nm. The major pathway is the formation of the HCO radical, characterized by Φ_{HCO}=0.51 ± 0.01. A second one is the reaction of the H atom coming from the single bond breaking of the aldehydes hydrogen defined by $\Phi_H \approx 0.1$. In acrolein photolysis, differently from the fluorinated aldehyde, no evidence of the H dissociation channel have been found. The totality of the HO_2 recorded comes from the HCO conversion and the associated quantum yield is Φ_{HCO} = 0.028 ± 0.001.

In conclusion, the experiments we have presented are conclusive in the case of the 3,3,3-trifluoropropionaldehyde, but multi-photons absorption occurred for the other molecules. Our experimental set-up was not sensitive enough to enable working at low fluence.

Finally the research on the VOC photolysis can be extended to other molecules with atmospheric interest. For example, glycolaldehyde and glyoxal, that are atmospheric relevant carbonyl compounds formed from the photochemical oxidation of volatile organic compounds such as ethene, 1,3-butadiene, isoprene, methyl vinyl ketone and acrolein.

A. Annex Cavity Ring Down Spectroscopy (CRDS)

A.1. The choice of the CRDS technique

In the current work, the measurement of time-profiles of HO_2 formed in the photolysis of aldehydes (in presence of O_2) by Cavity Ring Down Spectroscopy (CRDS) was undertaken to help to the interpretation of the mechanism of photodissociation. We have used this technique to further study the photolysis of acrolein and of the 3,3,3-trifluoro propionaldehyde. The CRDS experiments have been performed in Lille by the graduate student Chaithanya D Jain, member of the group of "Homogeneous and Heterogeneous Atmospheric Chemistry" directed by Christa Fittschen. Material, set-up and procedure for these analyses were explained in detail in previous publications (Thiebaud, Crunaire et al. 2007; Thiebaud, Parker et al. 2008; Parker, Jain et al. 2009; Parker, Jain et al. 2011).

The HO_2 radical was formed by reaction of O_2 with the HCO radical (Atkinson, Baulch et al. 2001) which is a major sub-product of aldehyde photolysis (reaction VIII-1) :

$$HCO + O_2 \rightarrow HO_2 + CO \qquad \text{VIII-1}$$

For O_2 concentrations in the range $[O_2] = 1 - 10\times10^{16}$ molec cm^{-3}, it is reasonable to consider that the conversion is complete and immediate on the time scale of the experimental set-up because HCO will be converted in 2 to 20 µs, respectively.

It should be emphasized that time-profiles of CO or H_2CO using the TDLAS set-up were obtained by photolysing the carbonyl compounds at 266 nm (3,3,3-trifluoro propionaldehyde) or 355 nm (acrolein), while in the following the laser was an excimer one firing at 248 nm.

A.2. 3,3,3-trifluoro propionaldehyde photolysis at 248 nm

The detection of HO_2 radicals formed in the photolysis of the 3,3,3-trifluoro propionaldehyde can be useful to distinguish the two different photolysis pathways VIII-2 and VIII-3 (Chiappero, Malanca et al. 2006; Antiñolo, Jiménez et al. 2011) leading to the formation of HCO radicals or H atoms *(this work)*.

$$CF_3CH_2CHO + h\nu \rightarrow CF_3CH_2 + HCO \qquad \text{VIII-2}$$

$$CF_3CH_2CHO + h\nu \rightarrow CF_3CH_2CO + H \qquad \text{VIII-3}$$

In presence of a large excess of O_2, HCO radicals are readily converted into HO_2 (VIII-1) (Atkinson, Baulch et al. 2001). The H atoms also react with O_2 (reaction VIII-4) to give HO_2, the rate constant being $k_{(H+O2)} = 2.54\times10^{-14}$ cm^3 molec $^{-1}$ s^{-1}.

$$H + O_2 (+ M) \rightarrow HO_2 (+ M) \qquad \text{VIII-4}$$

A.2.1. HO_2 profiles and quantum yields

Absolute concentration time profiles for HO_2 radicals have been measured by cw-CRDS following the 248 nm photolysis of CF_3CH_2CHO in 40 Torr of helium. In these experiments, the concentration of CF_3CH_2CHO was fixed to 6.2×10^{14} molec cm^{-3} and a large excess of O_2 ($[O_2]/[CF_3CH_2CHO] \approx 200$) was used to completely convert the HCO radicals formed in reaction VIII-1. HO_2 profiles recorded for three different photolysis energies are shown in Figure VIII-1. There are made of a fast increase of $[HO_2]$ followed by diffusion.

Profiles were fitted using equation (VIII-5) :

$$[HO_2] = \left([HO_2]_0 + A\times\left(1 - e^{-k_{H+O2}\cdot t}\right)\right)\times\left(e^{-kdiff\cdot t}\right) \qquad \text{VIII-5}$$

where $[HO_2]_0$ is the concentration of HO_2 originating from the fast conversion of HCO, *A* represents the concentration of HO_2 originating from the reaction of H with O_2.

In the case of a large concentration of O_2 and low temporal resolution, equation VIII-5 could be simplified to :

$$[HO_2] = \left([HO_2]_0\right)\times\left(e^{-kdiff\cdot t}\right) \qquad \text{VIII-6}$$

where $[HO_2]_0$ is the concentration of HO_2 originating from the conversion of HCO and H.
From the plot of the formation of HO_2 radicals versus the absorbed photons (Figure VIII-3), it was possible to evaluate a total yield of $\Phi_{HO2} = 0.61 \pm 0.03$.

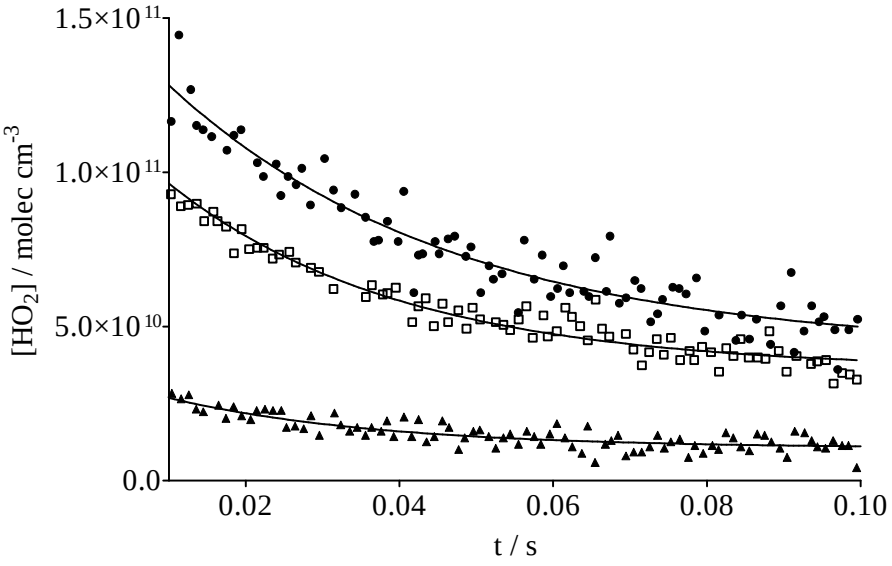

Figure VIII-1 Temporal profiles of HO_2 radicals obtained in the photolysis at 248 nm of $[CF_3CH_2CHO] = 6.2\times10^{14}$ cm^{-3} in the presence of $[O_2] = 1.3\times10^{17}$ cm^{-3}, for three different photolysis energies. Absorbed photons are 2.48, 1.27 and 0.63×10^{10} cm^{-3}.

Another experiment was performed varying the aldehyde concentration (from 0.28 to 1.5×10^{15} molec cm^{-3}) and represented in Figure VIII-2. These signals were recorded with a better time resolution and with a lower $[O_2]$ ($O_2 = 1.4\times10^{16}$ molec cm^{-3}) in order to distinguish the conversion of HCO from the formation of HO_2 by reaction (VIII-4) if H atoms were produced by reaction VIII-3. As it is possible to notice from Figure VIII-2, the HO_2 was mostly formed on very short time scales, too fast to be resolved by the cw-CRDS set-up. Even if the S/N ratio was not very good, a minor fraction of the HO_2 could be detected in a delayed way. This secondary formation of HO_2 represents the reaction of H-atoms with O_2 and suggests the existence of the photodissociation pathway (VIII-3). The profiles were fitted using the general equation VIII-5. *A* and $[HO_2]_{total}$ extracted from the fit of the profiles were respectively plotted versus the number of photons in Figure VIII-3 (respectively plain and clear triangles). From the linear regression of the curve (clear triangles) we determined the quantum yield of reaction VIII-3, estimated to be $\Phi_H = 0.10 \pm 0.03$. The total quantum yield determined from the slope of the line with plain triangles was found to be $\Phi_{HO2} = 0.50 \pm 0.02$. It is lower than the quantum yield obtained with the high O_2 concentration (squares in Figure VIII-3, $\Phi_{HO2} = 0.61$).

It is considered that the value of $\Phi_{HO2} = 0.50 \pm 0.02$ is underestimated because of the higher S/N and the presence of the kinetic.

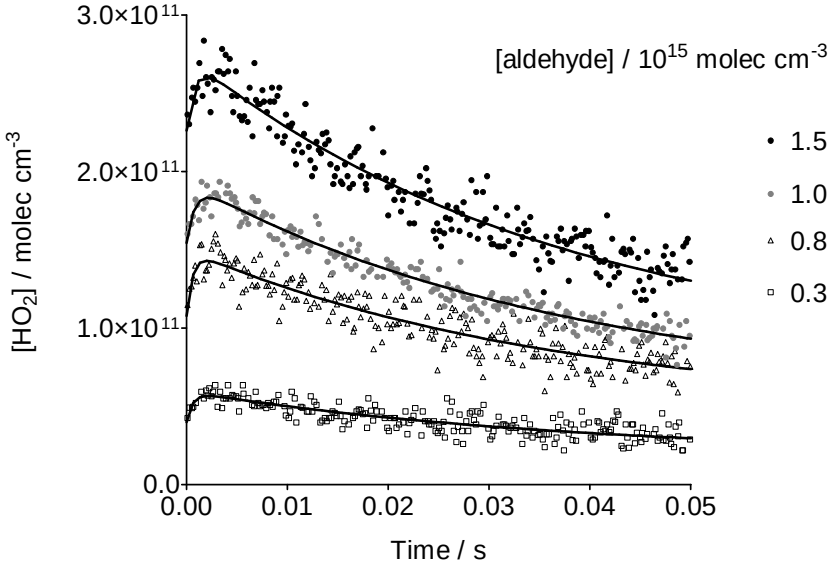

Figure VIII-2 Temporal profiles of HO_2 radicals obtained after photolysis at 248 nm of different [CF_3CH_2CHO] in the presence of [O_2] = 1.4×10^{16} cm^{-3} using constant photolysis energy (49.4 mJ cm^{-2}). Total pressure was 40 Torr in He.

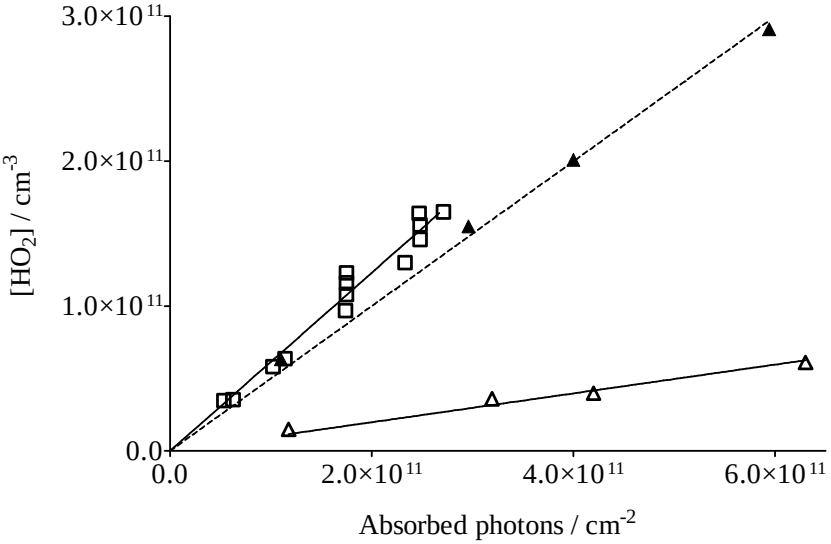

Figure VIII-3 HO_2 radical concentration obtained from 248 nm photolysis as a function of absorbed photons. HO_2 tot results (▲) and H results (Δ) from photolysis of 6.2×10^{14} cm^{-3} CF_3CH_2CHO in the presence of 1.3×10^{17} cm^{-3} O_2 at various energies. (□) are results from the photolysis of different CF_3CH_2CHO concentrations in the presence of 1.4×10^{16} cm^{-3} O_2 using constant photolysis energy (49.4 mJ cm^{-2}). The total pressure for all experiments was 40 Torr He. The results of the linear regressions Y = a X are respectively: (▲)– a = 0.50, (Δ)– a = 0.1, (□)– a = 0.61.

A.2.2. Study of the dependence of the O_2 concentration

Two measurements for the influence of O_2 on the kinetic have been performed varying the concentration of O_2 in the range $[O_2] = 0.1 – 1\times10^{17}$ molec cm^{-3}. It is possible to notice the slight increase in the slow HO_2 formation: addition of more O_2 increases the rate of HO_2 formation by reaction VIII-4. It means that the HO_2 radical is produced from the direct reaction of a photofragment with O_2 (Figure VIII-4). In addition, both curves presented in Figure VIII-4 have an apparent rate constant k in agreement with the expected value $k_{(H+O2)} = 2.54\times10^{-14}$ cm^3 molec $^{-1}$ s^{-1} (Table VIII-1) (Fernandes, Luther et al. 2008).

$[O_2]$ / molec cm^{-3}	$k_{expected}$ / s^{-1}	$k_{measured}$ / s^{-1}
1.13×10^{17}	2865	3553
1.31×10^{16}	332	340

Table VIII-1 Values extracted from the fit of the kinetic (Figure VIII-4) and the expected values for both $[O_2]$.

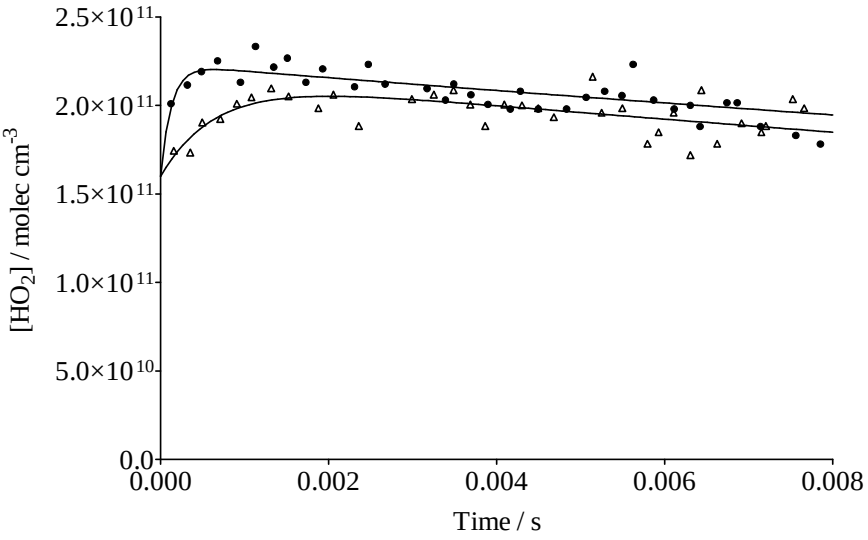

Figure VIII-4 Signal of HO_2 after photolysis at 248 nm of 3,3,3trifluoro propionaldehyde at two different O_2 concentrations $[O_2] = 1.13\times10^{17}$ molec cm^{-3} (•) and $[O_2] = 1.31\times10^{16}$ molec cm^{-3} (Δ).

A.3. HO_2 signals in acrolein photolysis at 248 nm

The second molecule analyzed with the CRDS technique was acrolein. The photodissociation pathways, already presented in chapter VII (page 119), lead to the formation of HCO radicals and H atoms (respectively reactions VIII-7 and VIII-8). From these two photofragments we obtain HO_2 after reaction with O_2 (reactions VIII-1and VIII-4), like in the photolysis of 3,3,3-trifluoropropionaldehyde.

$$CH_2=CHCHO + h\nu \rightarrow CH_2=CH + CHO \qquad \text{VIII-7}$$

$$CH_2=CHCHO + h\nu \rightarrow CH_2=CHCO + H \qquad \text{VIII-8}$$

The time-profiles of HO_2 obtained with different concentrations of acrolein are shown in Figure VIII-5. It is possible to exclude *a priori* the formation of a secondary HO_2 by reaction of H atom with O_2 (VIII-4). This observation led to the conclusion that the only HO_2 detected was likely produced immediately after the excimer pulse by HCO rapidly converted by reaction VIII-1. As a consequence the recorded data have been fitted to equation VIII-6, described by a simple exponential decay :

$$[HO_2] = ([HO_2]_0) \times \left(e^{-kdiff \cdot t}\right) \qquad \text{VIII-6}$$

A.3.1. Study of the dependence of the VOC concentration

As expected, the HO_2 variation with the acrolein concentration is linear. Effectively, analyzing the raw signals of HO_2 in the same conditions (UV excimer laser energy par pulse and oxygen concentration), we distinguish clearly that the signal at highest concentration lays on top, followed by the others two placed in order of decreasing magnitude.

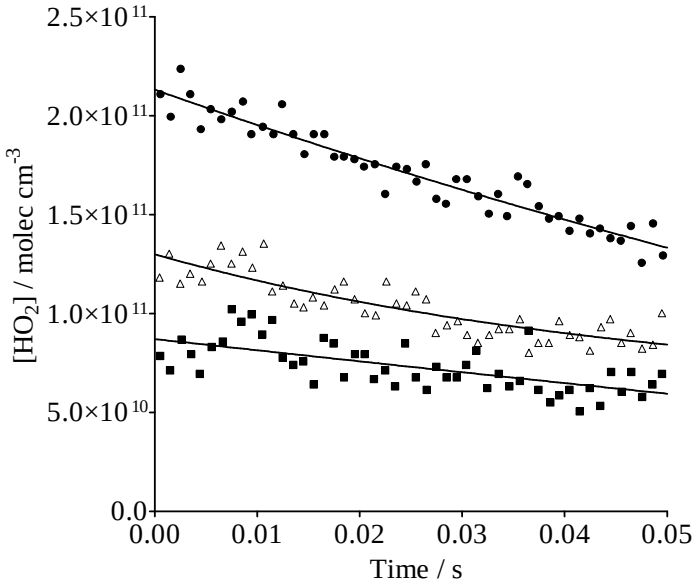

Figure VIII-5 HO_2 signals recorded for the photolysis (56mJ cm-2) of different acrolein concentrations: [CH_2=CHCHO]= 1.1×10^{17} molec cm^{-3} and [O_2]= 5.23×10^{16} molec cm^{-3} (•); .[CH_2=CHCHO]= 7.21×10^{16} molec cm^{-3} and [O_2]= 5.53×10^{16} molec cm^{-3} (Δ) and [CH_2=CHCHO]= 4.64×10^{16} molec cm^{-3} and [O_2]= 5.64×10^{16} molec cm^{-3} (■).

Two series of HO_2 signals have been recorded, using an excimer energy of 56 and 34 mJ per pulse. The concentrations of acrolein presented in Figure VIII-6 are divided by the fluence and the absorption cross section at 248 nm. The linearity represents the probability for an HO_2 to be from the photoproducts originated by photolysis. If we consider that all HCO radicals were totally converted because of the high O_2 concentration, we can assume that $\Phi_{HO2} = \Phi_{HCO} = 0.028 \pm 0.03$

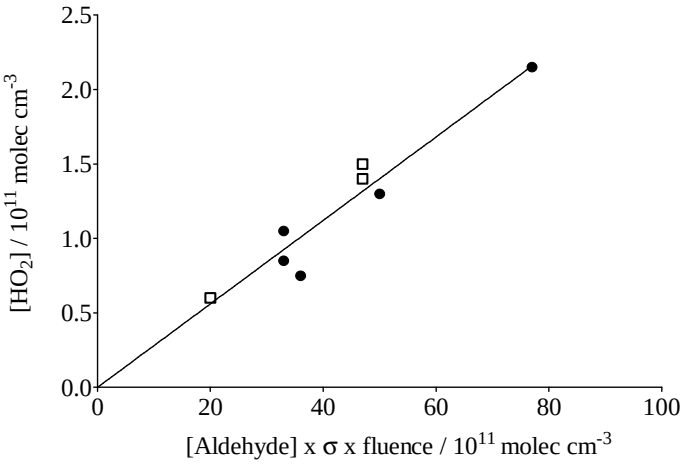

Figure VIII-6 Quantum yield for the acrolein photodissociation at 56mJ cm^{-2} (▲) and 34mJ cm^{-2} (□). Result of the linear regression Y=aX gives: a=0.028

A.4. CRDS conclusions

Acrolein and 3,3,3-trifluoro propionaldehyde have been photolyzed at 248 nm in the presence of O_2 and the formation of HO_2 radicals has been observed by CRDS. This technique has been employed to compare parallel different results: CO, H_2CO signals by TLDAS and HO_2 by CRDS. Even photolysing at different wavelengths (266 for the YAG laser and 248 for the excimer laser), the interpretation of the proposed photo-dissociation mechanisms are in agreement with both measurements. Here are presented briefly the observations obtained by the CRDS experiment.

A.4.1.3,3,3-trifluoro propionaldehyde

This fluorinated aldehyde has been photolyzed with an excimer laser at 248 nm and the HO_2 originated from the reaction of the photofragments with O_2 has been detected. From these experiments, two different ways of HO_2 formation have been observed. The main pathway is the rapid conversion of HCO radical (VIII-2), represented in the signals by the rapid rise at t = 0. A second one, clearly less important, is the reaction of the H atoms coming from the single bond breaking in the α position of the aldehydic group (VIII-3). The HCO way is clearly predominant and characterized by a $\Phi_{HCO} = 0.51\pm0.03$, while the H way has a $\Phi_H = 0.10\pm0.004$. From the combination of those two pathways we obtain the value of $\Phi_{tot} = 0.61\pm0.03$

A.4.2.Acrolein

The formation of HO_2 in the photolysis of acrolein at 248 nm seems to be composed by a single pathway, differently from the 3,3,3-trifluoro propionaldehyde. The HO_2 recorded came from the HCO conversion and the quantum yield associated, recorded for two different energies is $\Phi_{HCO} = 0.028\pm0.001$. No evidence of HO_2 coming from the H atom were detected, probably because of a too large time scale.

B. Annex instrumental

B.1. Calibration of the mass flow controller with the Drycal system

The introduction of the gases inside the cell has been performed with mass flow controllers Tylan. In Table VIII-2 are reported the eight mass flow controllers used in the current work of thesis reporting their field of application and theirs calibration curve parameters. The flow meter of 5000 ml min^{-1} was used coupled with the protection of the windows for experiments performed with low vapor pressure VOCs. For this category of compounds was employed the bubbler system (paragraph II.5.2 page 41) in which the flow of the carrier gas was introduced in the bubbler by the 500 ml min^{-1} flow meter; called "bubbling" in Table VIII-2. For the introduction of high vapor pressure compounds instead (paragraph II.5.1 page 39) were chosen the two flow meter "Low flows of VOC" in order to reduced the consumption of the VOC inside the balloon. In this second set-up all flows were reduced and as a consequence the flow meter "dilution" was substituted by "lower dilution" in order to reach suitable concentration of VOC inside the cell.

Use		Dilution	Bubbling	Windows	Low flows of O_2	High flows of O_2	Low flows of VOC (A)	Low flows of VOC (B)	Lower dilution
Flow max	*ml/min*	5000	500	300	50	300	50	50	1000
Regression	*a*	617.2	127.5	124.09	7.35	60.8	10.9	7.5	287.5
curve	*b*	137.8	4.8	-3	1.68	11.6	1	-3	32.7

Table VIII-2 Maximum flow and calibrations coefficients for the linear regression Y=a X + b.

Calibration with Drycal assures high precision in the flow estimation, but in order to be sure about their operability we have performed a control of the calibration in function of time (Figure VIII-8). This protocol ensures the reliability of the flows calculations at distance of months from the calibration. The calibration of mass flow controller should be repeated at the same conditions after different months. To proof the good operation of our mass flow controllers here are reported some calibration curves and their replicas in the time. It is evident that not important variation occurred in between the measures. Great attention has been focused on the flow-meter called tylanB, used for the sample introduction during the experiments of photolysis. As is proved in Figure VIII-7 no relevant variation on the regression curve has been detected in four different calibrations.

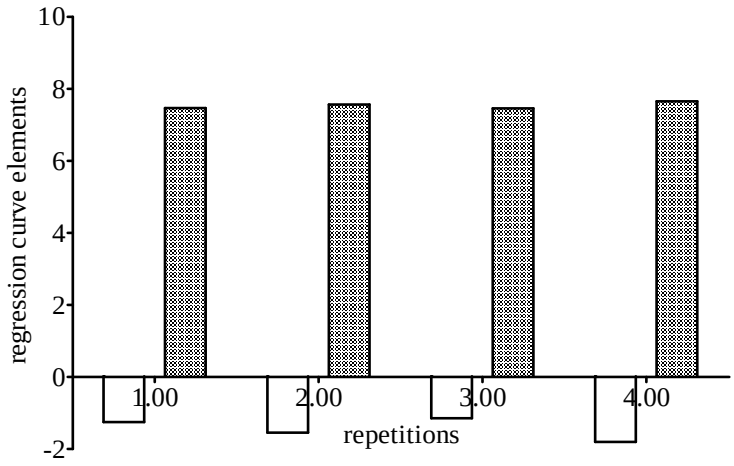

Figure VIII-7 Regression coefficients of the linear regression Y=a X + b for different replicas for the flow meter used for the VOC introduction and called “low flows of VOC (B)” in 0. Gray columns are the parameter a and clear columns are the parameter b.

B.2. Control of the pressure gauges

The pressure inside the cell has been measured for each recorded signal in order to determine the number of molecules that can occupy the volume of the cell at a certain temperature.

The pressure has been measured by two different gauges (Baratron MKS) with capacity 0-100 Torr. In order to check the response to a given pressure we have performed a parallel control on a fixed scale of pressures.

The mixture pressure is varied, controlled and kept constant by a mechanically regulated membrane (Leybold MR16) placed between the exit of the cell and the pumping system. As we can see from Figure VIII-8 the measure are almost identical, knowing that the precision of those gauges is ± 0.1 Torr. The good correspondences between the two measures prove the goodness of the measure and ensure that the gauges remain stables all long the analysis.

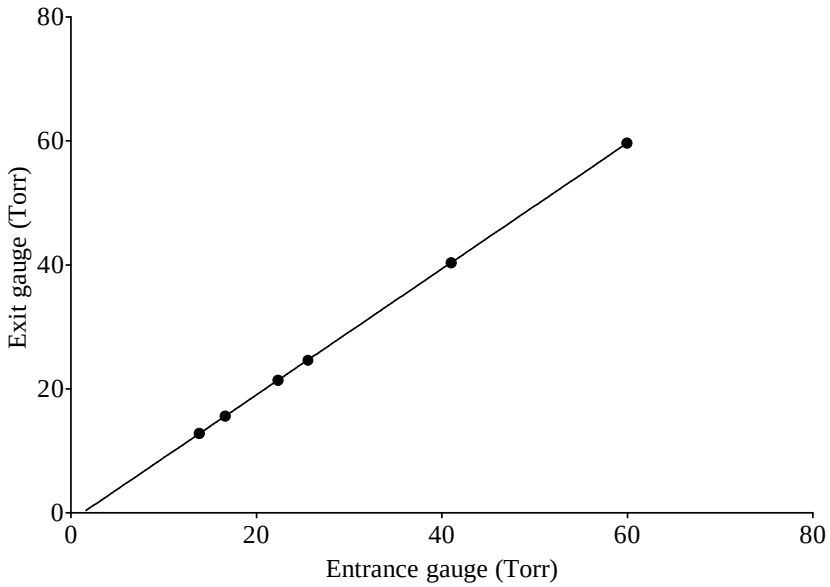

Figure VIII-8 Control of the response of two gauges (Baratron MKS). Gray columns are measurement performed at the exit and clear columns are the entrance of the cell. The result of the fit is Y=1.02 X -1.26

B.3. Working principles of the attenuator

The energy of the UV beam can be changed modifying the laser parameters or introducing a polarizer on the UV line. At 266 nm the energy can be changed regulating the angle and the temperature of the 4th harmonic crystal but these operations are long, delicate and generates disturbs on the laser profile. For this reason we preferred to employ an attenuator, which consists in a wave plate followed by a polarizer posed on a rotating support. The advantage of this mounting is the possibility to reduce the power of the laser beam by selecting a polarization maintaining the same direction of the polar at the exit.

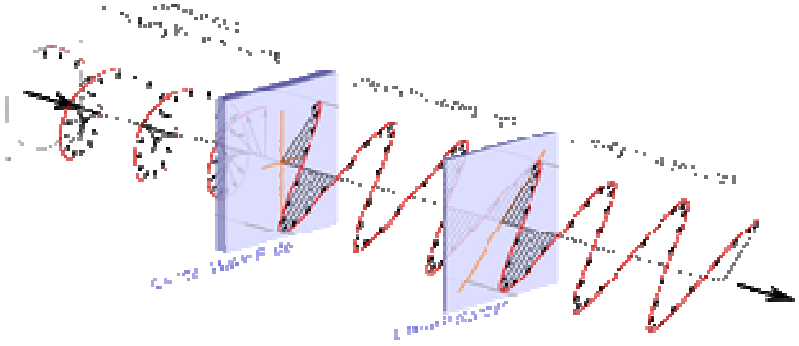

Figure VIII-9 Schematic of the quarter wave plate-polarizer effect on a left handed circularly polarized light

The incident radiation has an optical wavelength amplitude defined as:

$$I = A\sin(\omega t)$$

If we put an half wave plate on the optical way through the cell, we assist to a variation of the intensity due to a delay induced on the X axe (the slow axe of the incident radiation). The wave plate is mounted on a turning support which angle can be adjusted manually. If the plate has an angle θ, the slow axe will be affected by the delay of π on the component (Figure VIII-10). Such delay will modify the components of the A vector:

$$Ax = A\sin(\theta)\sin(\omega t - \pi) = -A\sin(\theta)\sin(\omega t) = -Ax$$

$$Ay = A\cos(\theta)\sin(\omega t)$$

At the exit of the wave plate the polarisation of the vector A will be turned with an angle 2θ (Figure VIII-10) because of the delay introduced on the slow axe.

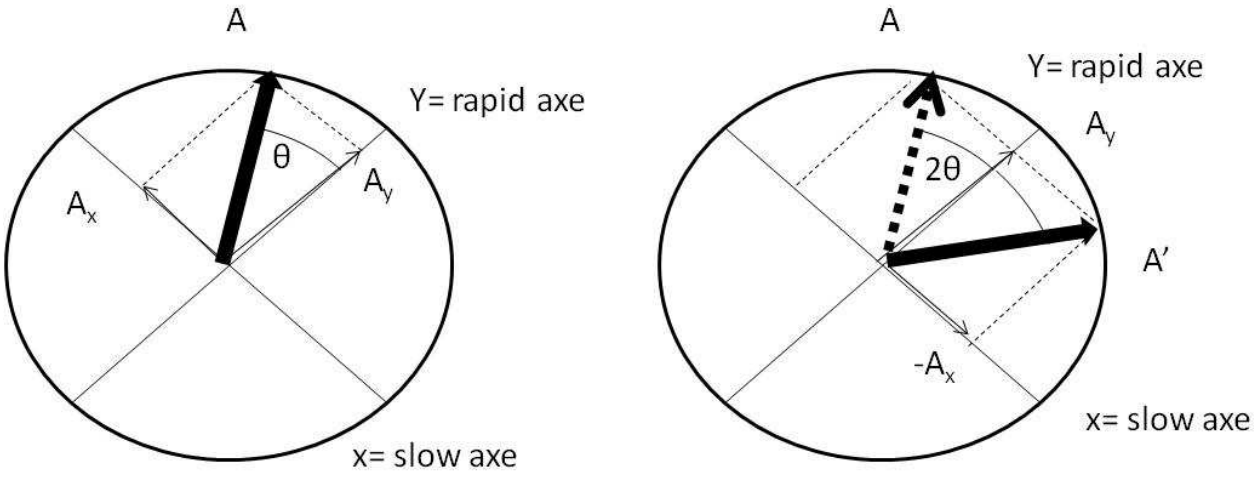

Figure VIII-10 Visual representation of the wavelength polarization before (left) and after (right) the wave plate

The radiation exits the wave plate and encounters the polarizer that will select a particular polarization. Depending on the orientation on the wave plate only a certain amount of radiation will pass through the polarizer. The intensity of the incident radiation will be reduced by the combination of these two elements of a factor depending on the angle of the wave plate (θ).

$$I = A^2 \sin^2(2\theta) = I_o \sin^2(2\theta)$$

In conclusion the wave plate followed by the polariser is a very suitable set-up to modify the laser energy at the entrance of the cell, without changing the polarization of the beam in the cell.

B.4. Calculation of the vapour pressure of hydroxyacetone

Due to lack of data in literature about the hydroxyacetone vapor pressure we have been obliged to determine it experimentally, with the procedure reported. The measurements have been performed with a thermally isolated box. That box was equipped with: an inside thermometer to check the temperature stability during the analysis and a pressure gauge for the Vp measurements. The temperature stability has been checked before each pressure vapor measurement. The temperature at which the HA is warmed are variables from 30 to 60°C: referring to our opertives conditions during the photolysis experieces. In such a range we can achieve the thermal stability of the compound inside the box in almost 15 minutes (Figure VIII-11). The record of the temperature in the first 15 min and the control of the thermal stability has been considered a necessary condition to start the measurement of the vapor pressure.

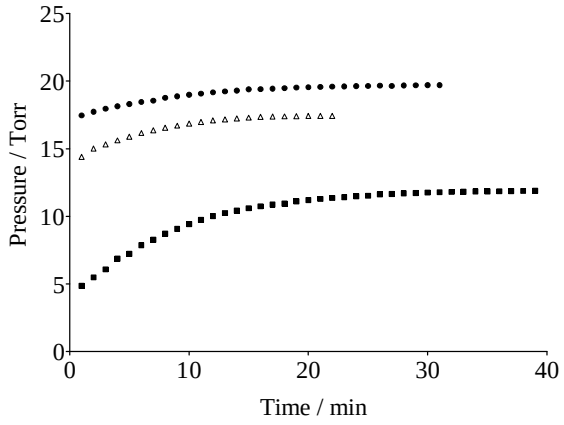

Figure VIII-11 Pressure stability inside the thermo stated box at different temperatures. 50℃ (•), 40℃ (Δ), 38℃ (■).

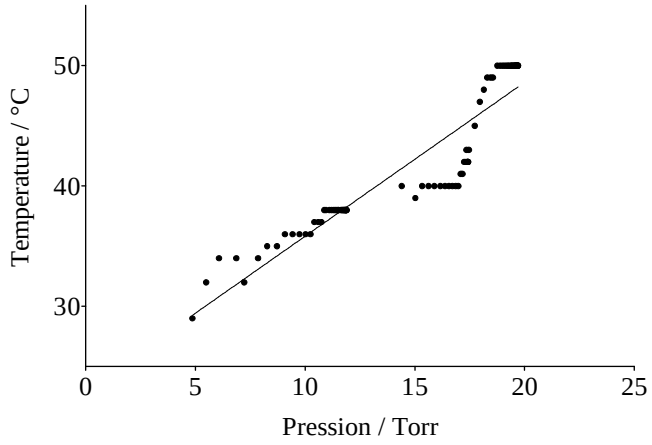

Figure VIII-12 Representation of the analysis made on the pressure variation at different temperatures.

Several replicas have been performed at different values of temperatures and pressure recorded has been plotted in Figure VIII-12. The calculation of the Vp as function of temperature has been possible only assuming the hypothesis:

”The linearity is conceivable only taking a small interval of temperature (30-60 °C), in which the logarithmic effect on the vapor pressure is not yet remarkable”.

By the way, in order to verify the relation between the saturation pressure and the temperature, we determine the latent heat of vaporization which relates the natural logarithm of the pressure with the inverse of the temperature (Figure VIII-13):

$$\ln\frac{p_{sat}}{P_0} = \frac{M \times L_v}{R} \times \left(\frac{1}{T_0} - \frac{1}{T}\right)$$

Where R= perfect gas constant; M= molecular mass; P_{sat}= 1 atm; T= boiling temperature (K). As result from this evaluation the value of Pv at the temperature of 45°C is Pv = 16.6±1.0 Torr.

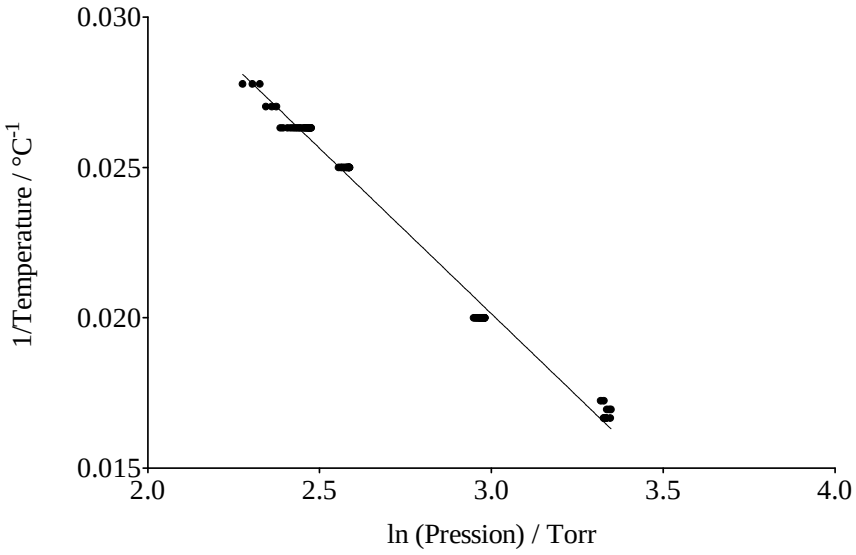

Figure VIII-13 The temperature of the thermostated box versus the natural logarithm of the saturation pressure recorded.

Bibliography

Aghedo, A. M., M. G. Schultz, et al. (2007). "The influence of African air pollution on regional and global tropospheric ozone." Atmos. Chem. Phys. **7**: 1193–1212.

Antiñolo, M., E. Jiménez, et al. (2011). "UV absorption cross sections between 230 and 350 nm and pressure dependence of the photolysis quantum yield at 308 nm of CF_3CH_2CHO." Phys. Chem. Chem. Phys. **13**: 15936–15946.

Antiñolo, M., E. Jiménez, et al. (2009). "Tropospheric photooxidation of CF_3CH_2CHO and $CF_3(CH_2)_2CHO$ initiated by Cl atoms and OH radicals." Atmos. Chem. Phys. Discuss. **9**.

Arnold, S. R. (2004). "Photodissociation of acetone: Atmospheric implications of temperature-dependent quantum yields." Geophysical Research Letters **31**(7).

Atkinson, R. (2000). "Atmospheric chemistry of VOCs and NOx." Atmospheric Environment **34**: 2063-2101.

Atkinson, R. and J. Arey (1998). "Atmospheric Chemistry of Biogenic Organic Compounds." Acc. Chem. Res **32**: 574-583.

Atkinson, R. and J. Arey (2003). "Gas-phase tropospheric chemistry of biogenic volatile organic compounds: a review." Atmospheric Environment **37**(Supplement 2): 197-219.

Atkinson, R. and D. L. Baulch (2004). "Evaluated kinetic and photochemical data for atmospheric chemistry: Volume I - gas phase reactions of Ox, HOx, NOx and SOx species." Atmos. Chem. Phys. **4**: 1461 – 1738.

Atkinson, R., D. L. Baulch, et al. (2001). "Summary of Evaluated Kinetic and Photochemical Data for Atmospheric Chemistry." JPL Publication **December**: 1 - 56.

Atkinson, R., D. L. Baulch, et al. (1997a). "Evaluated kinetic and photochemical data for atmospheric chemistry; supplement VI. IUPAC sub-committee on gas kinetic data evaluation for atmospheric chemistry." Journal of Physical Chemistry Reference Data **26**(6): 1329-1499.

Atkinson, R., D. L. Baulch, et al. (1997b). "Evaluated kinetic and photochemical data for atmospheric chemistry; supplement V-IUPAC sub-committee on gas kinetic data evaluation for atmospheric chemistry. Journal of Physical Chemistry Reference." Journal of Physical Chemistry Reference Data **26**(3): 521-1011.

Baasandorj, M., S. Griffith, et al. (2009). "Experimental and theoretical studies of the kinetics of the OH + hydroxyacetone reaction as a function of temperature." Journal of Physical Chemistry A **113**(39): 10495-10502.

Beyersdorf, A. J., D. R. Blake, et al. (2010). "Abundances and variability of tropospheric volatile organic compounds at the South Pole and other Antarctic locations." Atmospheric Environment **44**(36): 4565-4574.

BIOSINT. "BIOSINT web site." from www.biosint.com.

Blitz, M. A., D. E. Heard, et al. (2006). "Study of Acetone Photodissociation over the Wavelength Range 248-330 nm: Evidence of a Mechanism Involving Both the Singlet and Triplet Excited States." J. Phys. Chem. A **110**: 6742-6756.

Bowen, E. J. and H. G. Watts (1926). "The photolysis of acetaldehyde and of acetone." J. Chem. Soc. Faraday: 1607-1612.

Butokovskaya, N., N. Pouvsesle, et al. (2006). "Mechanism of the OH-Initiated Oxidation of Hydroxyacetone over the Temperature Range 236-298 K." J.Phys. Chem. A **110**: 6833-6843.

Chiappero, M. S., F. E. Malanca, et al. (2006). "Atmospheric Chemistry of Perfluoroaldehydes (C_xF_{2x}+CHO) and Fluorotelomer Aldehydes (C_xF_{2x}+CH_2CHO): Quantification of the Important Role of Photolysis." J. Phys. Chem. A **110**(11944-11953).

Chowdhury, P. K. (2003). "Infrared multiphoton dissociation of propynal: time resolved observation of CO (v ≥ 1) IR emission at 4.7 μm." Journal of Photochemistry and Photobiology A: Chemistry **154**: 259–265.

Chowdhury, P. K., H. P. Upadhyaya, et al. (2002). "ArF laser photodissociation dynamics of hydroxyacetone: LIF observation of OH and its reaction rate with the paren." Chemical Physical Letters **351**: 201-207DEF.

Christensen, L. E., M. Okumura, et al. (2006). "Experimental and ab initio study of the HO_2-CH_3OH complex: thermodynamics and kinetics of formation." J Phys Chem A **110**(21): 6948-6959.

Ciccioli, P., A. Cecinato, et al. (1996). "Occurrence of Oxygenated Volatile Organic Compounds (VOC) in Antarctica." International Journal of Environmental Analytical Chemistry **62**(3): 245 – 253.

Colberg, M. and G. Friedrichs (2006). "Room temperature and shock tube study of the reaction HCO+O_2 using the photolysis of glyoxal as an efficient HCO source." J. Phys. Chem. A **110**: 160 - 170

Crone, H. G. and R. G. W. Norrish (1933). "Predissociation in fluorescence emission spectra: Fluorescence of acetone vapour." Nature **132**(3328): 241.

Dagaut, P., R. Liu, et al. (1989). "Kinetic measurements of the gas-phase reactions of OH radicals with hydroxy ethers, hydroxy ketones, and keto ethers." Journal of Physical Chemistry A **93**(23): 7838-7840.

Delmas R., M. G., Peuch V.H. (2005). Physique et chimie de l'atmosphère.

Dillon, T. J., A. Horowitz, et al. (2006). "Reaction of HO with hydroxyacetone ($HOCH_2C(O)CH_3$): rate coefficients and mechanism." Phys. Chem. Chem. Phys. **8**: 236-246.

DUPONT. "Du Pont engineering internet site web." from http://www2.dupont.com/Heritage/en_US/1990_dupont/1990_replacing_cfcs_indepth.html

Earle, M. E., R. Mills, et al. (2009). "The photolysis of methyl vinyl ketone at 308nm." Journal of Photochemistry and Photobiology A: Chemistry **206**(1): 71-79.

Emrich, M. and P. Warneck (2000). "Photodissociation of Acetone in Air: Dependence on Pressure and Wavelength. Behavior of the Excited Singlet State." J. Phys. Chem. A **104**: 9436-9442.

EPA (2004). Definitions of VOC and ROG.

EPAdefinition. "United States Environmental Protection Agency ", from http://www.epa.gov/ozone/defns.html.

Esig. "European solvent industry group site web." from www.eisg.com.

Fahr, A., W. Braun, et al. (1993). "Photolysis of methyl vinyl ketone at 193.3 nm: quantum yield determinations of methyl and vinyl radicals." The Journal of Physical Chemistry **97**(8): 1502-1506.

Fang, W. H. (1999). "A CASSCF Study on Photodissociation of Acrolein in the Gas Phase." J. Am. Chem. Soc. **121**(36): 8376-8384.

Fernandes, R. X., K. Luther, et al. (2008). "Experimental and modelling study of the recombination reaction H + O_2 (+M) → HO_2 (+M) between 300 and 900 K, 1.5 and 950 bar, and in the bath gases M = He, Ar, and N_2." Physical Chemistry Chemical Physics **10**(29): 4313.

Finlayson-Pitts, B. J. and J. N. Pitts (2000). Chemistry of the Upper and Lower Atmosphere:Theory, Experiments, and Applications. A. Press. New York.

Gandini, A. and P. A. Hackett (1977). "Photochemistry of acetone under tropospheric conditions electronic relaxation processes in acetone and 1,1,1,trifluoroacetone vapour and the Gas Phase Reconbination of the acetyl radical at 22℃." Journal of American chemical Society **99**(19): 229-244.

Gardner, E., R. D. Wijayaratne, et al. (1984). "Primary Quantum Yields of Photodecomposition of Acetone in Air under Tropospheric." J. Phys. Chem. A **88**: 5069-5076.

Gardner, E. P., P. D. Sperry, et al. (1987). "Photodecomposition of acrolein in oxygen-nitrogen mixtures." The Journal of Physical Chemistry **91**(7): 1922-1930.

Gierczak, T., J. B. Burkholder, et al. (1998). "Photochemistry of acetone under tropospheric conditions." Chemical Physics Letters **231**: 229-244.

Gierczak, T., J. B. Burkholder, et al. (1997). "Atmospheric fate of methyl vinyl ketone and methacrolein." J. Photochem. Photobiol. A **110**: 1-10.

Guenther, A., C. Geron, et al. (2000). "Natural emissions of non-methane volatile organic compounds, carbon monoxide, and oxides of nitrogen from North America." Atmospheric Environment **34**: 2205-2230.

Guenther, A., C. N. Hewitt, et al. (1995). "A global model of natural volatile organic compound emissions." J. Geophys. Res. **100**(d5): 8873–8892.

Hanoune, B., S. Dusanter, et al. (2001). "Rate constant determination by laser photolysis/diode laser infrared absorption: examples of HCO + O_2 -> HO_2 + CO and CH_2OH + O_2 -> HCH(O) + HO_2 reactions at 294 K." Chemical physical letters **343**: 527-534.

Hurley, M. D., T. J. Wallington, et al. (2004). "Atmospheric Chemistry of Fluorinated Alcohols: Reaction with Cl Atoms and OH Radicals and Atmospheric Lifetimes." J. Phys. Chem. A **108**: 1973-1979.

Jacquinet-Husson, N., N. A. Scott, et al. (2008). "The GEISA spectroscopic database: Current and future archive for Earth and planetary atmosphere studies " Journal of Quantitative Spectroscopy and Radiative Transfer **109**(6): 1043-1059.

Jen, S. and I. Chen (1999). "Production of HCO from propenal photolyzed near 300 nm: Reaction mechanism and distribution of internal states of fragment HCO." J. Chem. Phys. **111**(18): 8448.

Jenkin, M. E. and K. C. Clemitshaw (2000). "Ozone and other secondary photochemical pollutants: chemical processes governing their formation in the planetary boundary layer." Atmospheric Environment **34**: 2499.2527.

Kelly, T., V. Bossoutrot, et al. (2005). "A Kinetic and Mechanistic Study of the Reactions of OH Radicals and Cl Atoms with 3,3,3-Trifluoropropanol under Atmospheric Conditions." J. Phys. Chem. A **109**: 347-355.

Khamaganov, V., R. Karunanandan, et al. (2009). "Photolysis of $CH_3C(O)CH_3$ at 248 nm and 266 nm: pressure and temperature dependent overall quantum yields." Physical Chemistry Chemical Physics(11): 6173-6181.

Khamaganov, V., R. Karunanandan, et al. (2007). "Photolysis of CH_3COCH_3 (248 nm, 266 nm), $CH_3COC_2H_5$ (248 nm) and CH_3COBr (248 nm): pressure dependent quantum yields of CH_3 formation." Phys. Chem. Chem. Phys. **9**: 4098–4113.

Magneron, I., R. Thévenet, et al. (2002). "A study of the photolysis and OH-initiated oxidation of acrolein and trans-crotonaldehyde." J. Phys. Chem. A **106**: 2526-2537.

Magneron, I., R. Thévenet, et al. (2002). "A study of the photolysis and OH-initiated oxidation of acrolein and trans-crotonaldehyde." J. Phys. Chem. A **106**: 2526-2537.

Maki, A. G. and J. S. Wells (1998). Wavenumber Calibration Tables from Heterodyne Frequency Measurements N. I. o. S. a. Technology. Gaithersburg, MD, [Access at http://physics.nist.gov/wavenum 01July 2011].

Matsunaga, S., A. Guenther, et al. (2007). "Importance of wet precipitation as a removal and transport process for atmospheric water soluble carbonyls." Atmospheric Environment **41**(4): 790-796.

Meyrahn, H., J. Pauly, et al. (1986). "Quantum yields for the photodissociation of acetone in air and an estimate for the lifetime of acetone in the lower troposphere." J. Atmos. Chem. **4**: 277–291.

Molina, M. and J. Rowland (1974). "Stratospheric Sink for Chlorofluoromethanes: Chlorine Atom-Catalysed Destruction of Ozone." Nature **249**: 810-812.

Moortgat, M. (2000). Evaluation of Radical Sources in Atmospheric Chemistry through Chamber and Laboratory Studies: RADICAL. Final report on EU project ENV4-CT97-0419, Max-Planck-Institut fur Chemie, Atmospheric Chemistry Division, Mainz, Germany.

Nesbitt, F. L., J. F. Gleason, et al. (1999). "Temperature dependence of the rate constant for the reaction HCO + O_2 → HO_2 + CO at T = 200-398 K." J. Phys. Chem. A **103**: 3038 - 3043.

Newman and Morris The Stratospheric text book. N. s. G. S. F. C. A. C. a. D. Branch.

Niinemets, Ü., F. Loreto, et al. (2004). "Physiological and physicochemical controls on foliar volatile organic compound emissions." Trends in Plant Science **9**(4): 180-186.

NIST. "NIST Chemical Kinetics database." from kinetics.nist.gov/kinetics/index.jsp.

Norrish, R. G. W. (1934). "Free radicals of short life: Chemical aspects. A. General and inorganic. The primary photochemical production of some free radicals " Transactions of the Faraday Society **30**(Part II.): 103-113.

Norrish, R. G. W., H. G. Crone, et al. (1934). "Primary photochemical reactions. Part V. The spectroscopy and photochemical decomposition of acetone." Journal of the Chemical Society 1456-1464.

North, S., D. A. Blank, et al. (1995). "Evidence for stepwise dissociation dynamics in acetone at 248 and 193 nm." J. Chem. Phys. **102**(11): 4447-4460.

Olivero, J. J. and R. L. Longbothum (1977). "Empirical fits to the Voigt linewidth: A brief review." J. Quant. Spectrosc. Radiat. Transfer **17**: 233-236.

Orlando, J. J., G. S. Tyndall, et al. (1999). "The rate and mechanism of the gas-phase oxidation of hydroxyacetone." Atmosph. Environ. **33**: 1621.

Parker, A., C. Jain, et al. (2009). "Kinetics of the reaction of OH radicals with CH_3OH and CD_3OD studied by laser photolysis coupled to high repetition rate laser induced fluorescence." React.Kinet.Catal.Lett. **96**(2): 291−297.

Parker, A., C. Jain, et al. (2011). "Simultaneous, time-resolved measurements of OH and HO_2 radicals by coupling of high repetition rate LIF and cw-CRDS techniques to a laser photolysis reactor and its application to the photolysis of H_2O_2." Appl Phys B **103**: 725–733.

Paulot, F., J. D. Crounse, et al. (2009). "Isoprene photooxidation: new insights into the production of acids and organic nitrates." Atmos. Chem. Phys. Discuss. **9**: 1479–1501.

Petitjean, M., E. Reyès-Pérez, et al. (2010). "Vapor pressure measurements of hydroxyacetaldehyde and hydroxyacetone in the temperature range (273 to 356) K." Journal of Chemical and Engineering Data **55**(2): 852-855.

Raber, W. H. and G. K. Moortgat (1996). Progress and Problems in Atmospheric Chemistry. Singapore, World Scientific Publ. Co.

Rajakumar, B., T. Gierczak, et al. (2008). "The CH_3CO quantum yield in the 248 nm photolysis of acetone, methyl ethyl ketone, and biacetyl." Journal of Photochemistry and Photobiology A: Chemistry **199**(2-3): 336-344.

Ravishankara, A. R. and G. K. Moortgat (1994). "Atmospheric photochemistry and spectroscopy, Low Temperature Chemistry of the Atmosphere." NATO ASI Series, Springer Verlag **1**(21): 111-145.

Reid, J. P., C. J. S. M. Simpson, et al. (1995). "Vibrational relaxation of CO (v = 1) by inelastic collisions with 3He and 4He." The Journal of Chemical Physics **103**(7): 2528-2537.

Roberts, J. M. and S. B. Bertman (1992). "Thermal decomposition of peroxyacetic nitric anhydride (PAN) and peroxymethacrylic nitric anhydride (MPAN)." International Journal of Chemical Kinetics **24**(3): 297-307.

Romero, M. T., M. A. Blitz, et al. (2005). "Photolysis of methylethyl, diethyl and methylvinyl ketones and their role in the atmospheric HOx budget." Faraday Discussions **110**: 73–88.

Sellevåg, S. R., T. Kelly, et al. (2004). "A study of the IR and UV-Vis absorption cross sections, photolysis and OH-initiated oxidation of CF_3CHO and CF_3CH_2CHO." Physical Chemistry Chemical Physics **6**(6): 1243.

Sellevåg, S. R., Y. Stenstrøm, et al. (2005). "Atmospheric Chemistry of CHF_2CHO: Study of the IR and UV-Vis Absorption Cross Sections, Photolysis, and OH, Cl, and NO_3Initiated Oxidation." J. Phys. Chem. A **109**(16): 3652-3662.

Sinclair, P. M., P. Duggan, et al. (1998). "Line Broadening in the Fundamental Band of CO in CO–He and CO–Ar Mixtures." J.Mol. Spectrosc. **191**(1): 258-264.

Sinclair, P. M., P. Duggan, et al. (1997). "Line Broadening, Shifting, and Mixing in the Fundamental Band of CO Perturbed by N_2 at 301 K." J.Mol. Spectrosc. **181**(1): 41-47.

Singh, H., Y. Chen, et al. (2001). "Evidence from the Pacific troposphere for large global sources of oxygenated organic compounds." Nature **410**: 1078.

Somnitz, H., M. Fida, et al. (2005). "Pressure dependence for the CO quantum yield in the photolysis of acetone at 248 nm: A combined experimental and theoretical study." Physical Chemistry Chemical Physics **7**(18): 3342.

Somnitz, H., T. Ufer, et al. (2009). "Acetone photolysis at 248 nm revisited: pressure dependence of the CO and CO_2 quantum yields." Phys. Chem. Chem. Phys. **11**: 8522–8531.

Stephens, E. R., E. F. Darley, et al. (1961). "Photochemical reaction products in air pollution." International Journal of Air and Water Pollution **4**: 79–100.

Stephenson, J. C. (1973). "Vibrational excitation and relaxation of the CO(v=1) and CO(v=2) states." Appl. Phys. Lett. **22**(11): 576-580.

Swanson, A. L. (2003). "Seasonal variations of C2–C4 nonmethane hydrocarbons and C1–C4 alkyl nitrates at the Summit research station in Greenland." Journal of Geophysical Research **108**(D2).

Szilágyi, I., G. Kovács, et al. (2009). "photochemical and photophysical study on the kinetics of the atmospheric photodissociation of acetone." Reaction Kinetics and Catalysis letters **96**(2): 437-446.

Tadic, J., G. K. Moortgat, et al. (2006). "Photolysis of glyoxal in air." Journal of Photochemistry and Photobiology A: Chemistry(177): 116–124.

Thiebaud, J., S. Crunaire, et al. (2007). "Measurements of line strengths in the 2v1 band of the HO2 radical using laser/Continuous Wave Cavity Ring-Down Spectroscopy (cw-CRDS)." J. Phys. Chem.A **111**: 6959-6966.

Thiebaud, J., A. Parker, et al. (2008). "Detection of HO_2 Radicals in the Photocatalytic Oxidation of Methyl Ethyl Ketone." J. Phys. Chem. C **112**(7): 2239.

Thrush, B. A. and G. S. Tyndall (1982). "The rate of reaction between HO_2 radicals at low pressures." Chem. Phys. Lett. **92**: 232.

Umstead, M. E., R. G. Shortridge, et al. (1978). "Energy Partitioning in the Photodissociation of C_3H_40 Near 200 nm." The Journal of Physical Chemistry **82**(13): 1455-1460.

UNEP. "Montreal protocol from the United Nation Environment Program." from www.unep.org/ozone/pdfs/montreal-protocol2000.pdf http://ozone.unep.org/Publications/MP_Handbook/Section_1.1_The_Montreal_Protocol/Article_2A.shtml.

Wallington, T. J., P. Dagaut, et al. (1987). "Correlation between Gas-Phase and Solution-Phase Reactivities of Hydroxyl Radicals toward Saturated Organic Compounds." J. Phys. Chem. A **92**: 5024–5028.

Warneck, P. (2001). "Photodissociation of acetone in the troposphere: an algorithm for the quantum yield." Atmosp.Environm **35**: 5773-5777.

Watson, J. J., J. A. Probert, et al. (1991). "Global Inventory of Volatile Organic Compound Emissions from Anthropogenic Sources."

Werle, P., R. Mucke, et al. (1995). "Near-infrared trace-gas sensors based on room temperature diode lasers." Appl Phys B **67**: 307–315.

Wollenhaupt, M., S. A. Carl, et al. (2000). "Rate coefficients for reaction of OH with acetone between 202 and 395 K " Journal of Physical Chemistry A **104**(12): 2695 - 2705.

Wu, Xie, et al. (2003). "Ab initio studies for the photodissociation mechanism of hydroxyacetone." Journal of Computational Chemistry **24**(8).

Yao, X., N. T. Lau, et al. (2005). "The use of tunnel concentration profile data to determine the ratio of NO_2/NO_x directly emitted from vehicles." Atmos. Chem. Phys. Discuss. **5**: 12723–12740.

Zhang, D., W. Lei, et al. (2002). "Mechanism of OH formation from ozonolysis of isoprene: kinetics and product yields." Chemical Physics Letters **358**: 171–179.

Zhu, C. and L. Zhu (2010). "Photolysis of Glycolaldehyde in the 280-340 nm Region." J. Phys. Chem. A **114**: 8384–8390.

Résumé :

Les sources d'émission de composés organiques volatils (COV) dans l'atmosphère sont très majoritairement la végétation, suivie par l'activité humaine. Les arbres (forêts d'Amérique du Nord) émettent de grandes quantités d'isoprène, hydrocarbure insaturé qui conduit par oxydation à de nombreux composés carbonylés, dont la méthylvinylcétone (MVK) et l'hydroxyacétone (HAC). Ces COV secondaires sont eux-mêmes oxydés ou photolysés. Des mécanismes élaborés de dégradation de l'isoprène, comprenant plusieurs dizaines de réactions incluant toutes les espèces secondaires (mécanismes des groupes de Mainz (Allemagne) ou de Leeds (Royaune-Uni)), se développent par l'ajout de données expérimentales nouvelles ou plus précises. En particulier, les rendements quantiques de photolyse, définis comme la fraction de photons absorbés donnant lieu à une dégradation des molécules, sont peu connus car difficiles à mesurer ou devant être déduits du rendement de produits secondaires.

Ce travail est une contribution à la détermination des rendements quantiques de photolyse de composés carbonylés. Nous avons utilisé la photolyse laser couplée à la spectroscopie infrarouge de CO ou H_2CO résolue dans le temps. L'acétone, l'HAC ont été photolysées à 266 nm, l'acroléine et la MVK à 355 nm. Des rendements quantiques ont été obtenus mais doivent être pris avec précaution compte-tenu de la possible absorption à plusieurs photons, dont CO observé dans des états vibrationnels excités constitue la preuve.

La photolyse de l'acrolein et du 3,3,3-trifluoropropanal, aldéhyde fluoré provenant de la dégradation des HFC, ont également été étudiées à 248 nm et analysée conjointement par CRDS dans un autre groupe.

Abstract :

Emissions of organic volatile compounds in the atmosphere (COV) are due to human activities, and mainly from vegetation. Isoprene, which is an unsaturated hydrocarbon, is emitted in large quantities by deciduous trees (forests of North America) and leads by oxidation to carbonyl compounds, like methylvinylketone (MVK) or hydroxyacetone (HAC). These compounds are themselves oxidized or photolysed. Mechanisms of isoprene oxidation, comprising tens of reactions including all secondary species, are still under development (Mainz or Leeds mechanisms). They are improved by inclusion of new or more precise experimental data, like quantum yields of photolysis, which are defined as the efficiency of photons in breaking bonds.

We used time-resolved laser infrared spectroscopy coupled to UV laser photolysis (TDLAS) to study the photolysis of acetone and HAC at 266 nm, and of MVK and acrolein at 355 nm. Quantum yields were obtained, but they should be taken with care due to the multi-photons absorption which occurred, demonstrated by the observation of CO in vibrational excited states.

A joint analysis of the photolysis at 248 nm of acrolein and 3,3,3-trifluoropropionaldehyde by CRDS was also studied. The quantum yields of different channels of photolysis were obtained.

Mots-clés :

Photolyse laser - Spectroscopie infrarouge - Rendement quantique – Hydroxyacétone - 3,3,3-trifluoropropanal – Diode laser – Acétone – Méthyle vinyle cétone - Acroléine